QUANTUM EFFICIENCY CHARACTERIZATION
OF
FULLY DEPLETED BACK SIDE ILLUMINATED CCD'S

draft ver 0.4, August 22, 2006

Diplomathesis

by

Maximilian H. Fabricius

Optical Institute

Technische Universität Berlin

prepared at the

Lawrence Berkeley National Laboratory, Berkeley, CA, USA

September 2006

QUANTUM EFFICIENCY CHARACTERIZATION
OF
FULLY DEPLETED BACK SIDE ILLUMINATED CCD'S

draft ver 0.4, August 22, 2006

Diplomarbeit

von

Maximilian H. Fabricius

Optisches Institut

der

Technische Universität Berlin

angefertigt am

Lawrence Berkeley National Laboratory, Berkeley, CA, USA

September 2006

ABSTRACT

The CCD group at the LBNL has developed fully depleted backside illuminated CCDs which are optimized for higher infrared sensitivity. Accurate knowledge of their quantum efficiency (QE) provides important feedback for the design of new CCDs and their antireflective coatings. Decisions of their usability in both ground-based and space-based missions require precise knowledge of the quantum efficiency.

In addition to the already existing test procedures for CCDs at the LBNL a setup to measure the QE has been developed. Its design is similar to already existing setups. The CCD is illuminated by a uniform and monochromatic lightfield. A calibrated photodiode provides the reference for the QE calculation. The QE is measured in the wavelength range from 300 nm to 1100 nm.

Main goal of the work is the characterization of this setup, the exploration of its limitations and systematics and development of auxiliary measurements to verify and improve the QE measurements.

Over a wide wavelength range we would expect 1 - R = QE, where R is the CCD's reflectivity. An unconventional reflectometer has been developed to make this measurement.

In addition to the conventional QE characterization, we measure the QE by comparing the current from a calibrated photodiode with the photo current from the CCD wired up as a photodiode. No system gain calibration is necessary in this mode of measurement. In photodiode mode the QE can be measured at room temperature whereas the operating temperature for the CCDs is -140°C.

The standard method for gain calibration involves a ^{55}Fe x ray source. An attempt was made to improve the existing algorithm for this calibration method. A new method - the fast photon transfer curve - which allows an alternative way for the gain calibration has been successfully tested.

Finally the knowledge of the physical parameters and dimensions of the CCDs allowed to perform calculations to make predictions of the QE and the reflectivity. A deviation of the measured results from the theory allows the search for flaws in the production process and might point to behavior not yet understood.

for Wenjing

ACKNOWLEDGEMENTS

The stay at the Lawrence Berkeley National Laboratory has been a very enjoyable time. I would like to deeply thank everybody who supported me in various ways during my one year stay in California and during the period afterwards during which this work was created.

Armin Karcher - my advisor at the LBNL - has always been a great source guidance, knowledge and support. He provided me with a lot of suggestions and ideas for the debugging of the QE setup and the development of the reflectometer. Not only Armin was the ideal advisor also he and his family supported me personally and have great responsibility for my very enjoyable time in Berkeley.

Bill Kolbe was always willing to explain underlying physical backgrounds and facts in - sometimes long - discussions. He also provided me with many hints and ideas. More than a formadable coworker Bill Kolbe has been a great friend.

I am grateful for Susanna Orlic's decision to support my thesis. Without her I would not have been able to go to Berkeley. Thank you for all the support and the many appointments during deadline times.

Don Groom supported me with a lot of information in the form of *private lectures* which I enjoyed a lot. As the careful reader will find, many parts of this thesis are based on his earlier work. Thank you Don also for letting me steal so many figures! Finally it was Don who promoted me to give the talk in San Jose which was a great experience.

Chris Bebek made it all possible. He always had an open ear for technical problems and came up with may excellent suggestions.

I thank all my office mates and friends who made the stay at the LBNL such an enjoyable and memorable time. Especially I want to mention Jessamyn Fairfield, Sherri Cheeseboro, Gersende Prior, Joao Pequenao and the whole BFC.

John Emes helped me with many technical questions and has been of great patience in fixing broken wirebonds.

Richard Kyper introduced me to the machine shop and spend many hours showing me the correct and save usage of machines and tools. Without his help I would not have been able to build the reflectometer.

I would like thank the Lawrence Berkeley Laboratory and the SNAP group for inviting me twice - once for my internship in 2004 on once for this work - to the US and allowing me to write my thesis about their CCDs.

Wolfgang Lorenzon and Michael Schubnell of the University of Michigan allowed me to integrate their large 100 mm field shutter into out QE setup. This detail turned out to be of great importance to the accuracy of our measurement.

Finally, I would like to express my gratefulness to all the support by my family during the whole time, especially my wife Wenjing Zhang.

.

CONTENTS

LIST OF TABLES

LIST OF FIGURES

CHAPTER 1

INTRODUCTION

Charge-Coupled Devices or CCDs became an extremely important technology as well in the consumer market - a majority of nowadays digital cameras employ CCDs as detectors - as in science. CCDs are silicon based optical detectors which allow to take two dimensional resolved image of an incident light field. Their sensitivity reaches from soft x rays into the near infrared (~ 1000 nm). Their extremely high light sensitivity in the visible and IR (100 times higher than film), their excellent linearity and their ability to handle exposure times of several hours quickly made CCDs become very important for astronomical applications. Nowadays typical astronomical CCDs have quatum efficiencies as high as 98% at a wavelength of 600 nm - i.e. 98 out of 100 incident photons generate an detectable electron hole pair.

The LBNL developed techniques to extend the sensitivity of CCDs further into the infrared by increasing their thickness. The development is part of the proposal process for the Super Nova Cosmology Probe (SNAP). Besides 36 infrared detectors 36 LBNL CCDs will be installed in its focal plane.

To measure the quantum efficiency one typically employes a monochromatic light source with selectable wavelength and a previously calibrated detector such as photodiode. Based on a somewhat canonical design, a setup was developed as part of an earlier thesis and a first prototypical QE curves were measured for two devices.

Here we carfully search for systematics and test modifications to further decrease systematic effects. In addition to the quatum efficiency measurement itself we develop techniques to verify our data. Since over a broad wavelength range the CCD's ability to detect photons is limited mostly by its reflectivity, a known reflectivity is an important verification for a QE measurement. We therefore developed a system to measure the reflectivity. As the gain calibration introduces one of the most significant systematics, further improvements to existing gain calibration algorithms as well as a new method for the gain calibration the Fast Photon Transfer Curve are tested.

1.1 CCDs

A glimpse at the history [1]

Invented in 1969 by Willard S. Boyle and George E. Smith at the Bell Telephone Laboratories Charge-Coupled Devices quickly revolutionized digital film and photography. In 1974 the first commercially available CCD was sold by Fairchild

---

[1] What follows is a brief summary of chapter one in [25].

Semiconductors. Mounted by J. R. Jenasick on his 8 inch amateur telescope it produced the first astronomical image in the same year [25].
In 1976 the JPL Traveling CCD Camera System was on Mount Lemmon's 154-cm telescope produced the first professional grade astronomical images.

Devices on board of the Galileo mission to Jupiter launched in 1989, the Hubble Space Telescope launched in 1990, the Yohkoh Soft X-ray Telescope launched in 1991, and the Space Shuttle Electronic Still Camera were the first CCDs in space [26]. Nowadays CCDs are used in a large number of space probes and telescopes.

One of the largest CCD cameras OmegaCam, a 16.000 x 16.000 pixel CCD Camera for the VLT Survey Telescope, is expected to become operational at Paranal in 2007.

What are CCDs

A CCD is a photon detector. Photons above a certain threshhold energy create electron hole pairs when the interact with silicon. An array of potential wells in the CCD allow to capture either the electrons or the corresponding holes which result from that electron hole pair creation. The potentials in the wells are variable. By changing them one can *clock* the charge out of the CCD.

Before describing in more detail how the potential wells are created the clocking mechanism will be clarified first. (One might want to consult [25] for the famous picture of the "bucket brigade" from Jerome Kristian and Morley Blouke).

The potential wells are organized in a two dimensional array within the rectangular shaped photoactive area of silicon, the bulk material of the CCD. These wells form the pixel of the CCD.
A special row with the same number of potential wells as the CCD has columns is located at one edge of the CCD. This row is called the serial register.
To *read* the CCD out, first all the wells or pixels are moved in a parallel manner by one row towards the serial register at the edge. The charge which was formerly located in the row of wells closest to the serial register is now stored in the serial register (see Fig. 1.3) . Now, the wells in the serial register are moved towards one corner of the CCD where the serial register ends (see Fig. 1.4).
A readout amplifier at this corner allows to measure the amount of charge in each of the potential wells.

After all the wells on the serial register got moved to and measured by the readout amplifierer, again all the wells in the active region get moved parallel towards the serial register. This procedure is repeated until the whole charge in the CCD is read out.

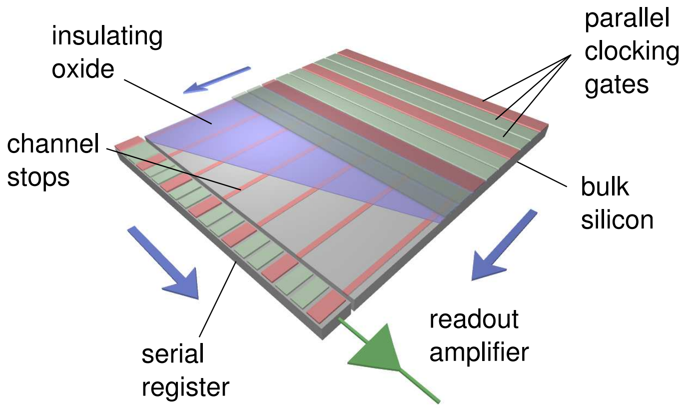

Figure 1.1: Schematic picture of a three phase readout CCD. Arrows indicate later clocking direction. Red electrodes symbolize high potential and green the low potentials. A pixel is the region between two channel stops and two parallel strip electrodes at high potential. During the exposure the gates are held at the indicated fixed potentials preventing the charge carriers - once created through the absorption of a photon - from leaving the pixel.

Since the columns of wells in the active region is always moved in parallel, they are referred to as the parallel registers. The serial register at the edge is called that way because the charge is moved in a serial manner pixel by pixel towards the readout amplifier.

Not all CCDs are restriced to this mode of operation. Orthogonal Transfer CCDs allow arbitrary movement of the pixels in the active region [48].

This work will treat three phase readout CCDs to which the above mentioned principles apply. The columns in the CCDs are separated by so called channel stops. If electons are used as signal carriers, n-doped channel stops form the potential barriers in one dimension. In the case of electron-holes the channel stops are p-doped.

Perpendicular to the channel stops and separated by a silicon oxide layer from the silicon, strip electrodes - the clocking gates - on the surface of the CCD allow to raise and lower potential barriers (see Fig. 1.1). In a three-phase readout device these electrodes are arranged in groups of three electrodes for the three phases ϕ_1, ϕ_2 and ϕ_3.

The serial register at the edge of the CCD is of similar design as the columns. It consists of one channel covered by electrodes which provide the variable potentials.

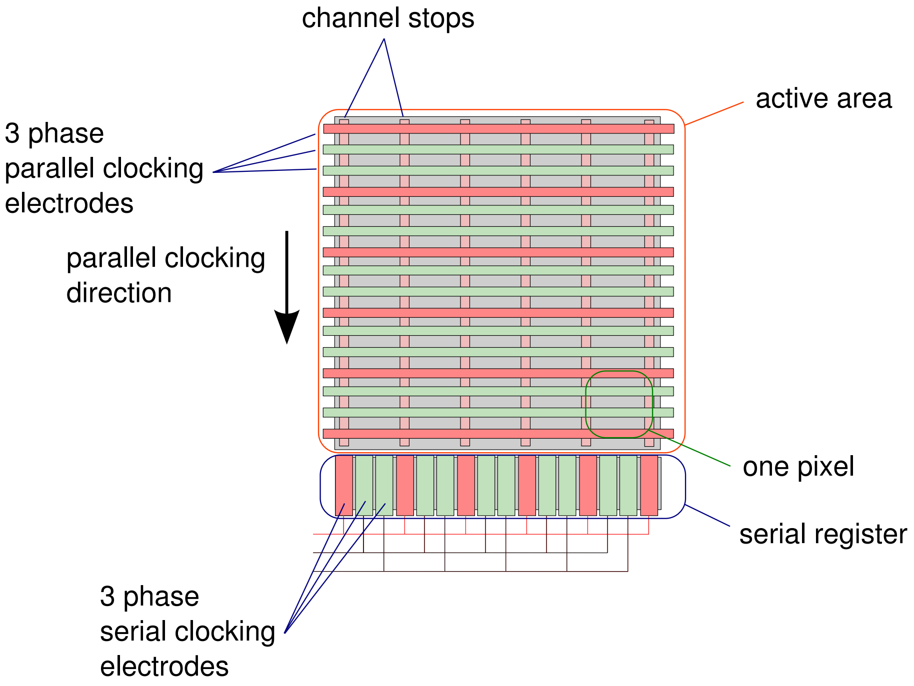

Figure 1.2: Another view of the concept of a three phase readout CCD. Channel stop implants prevent charge from moving in horizontal direction within the active area. Vertical clocking lines are held at fixed potentials during the exposure: Every third parallel clocking line is held in barrier phase (high potential) and prevents charge from moving vertically during the exposure. The area between two channel stops and two barrier phase electrodes forms one pixel.

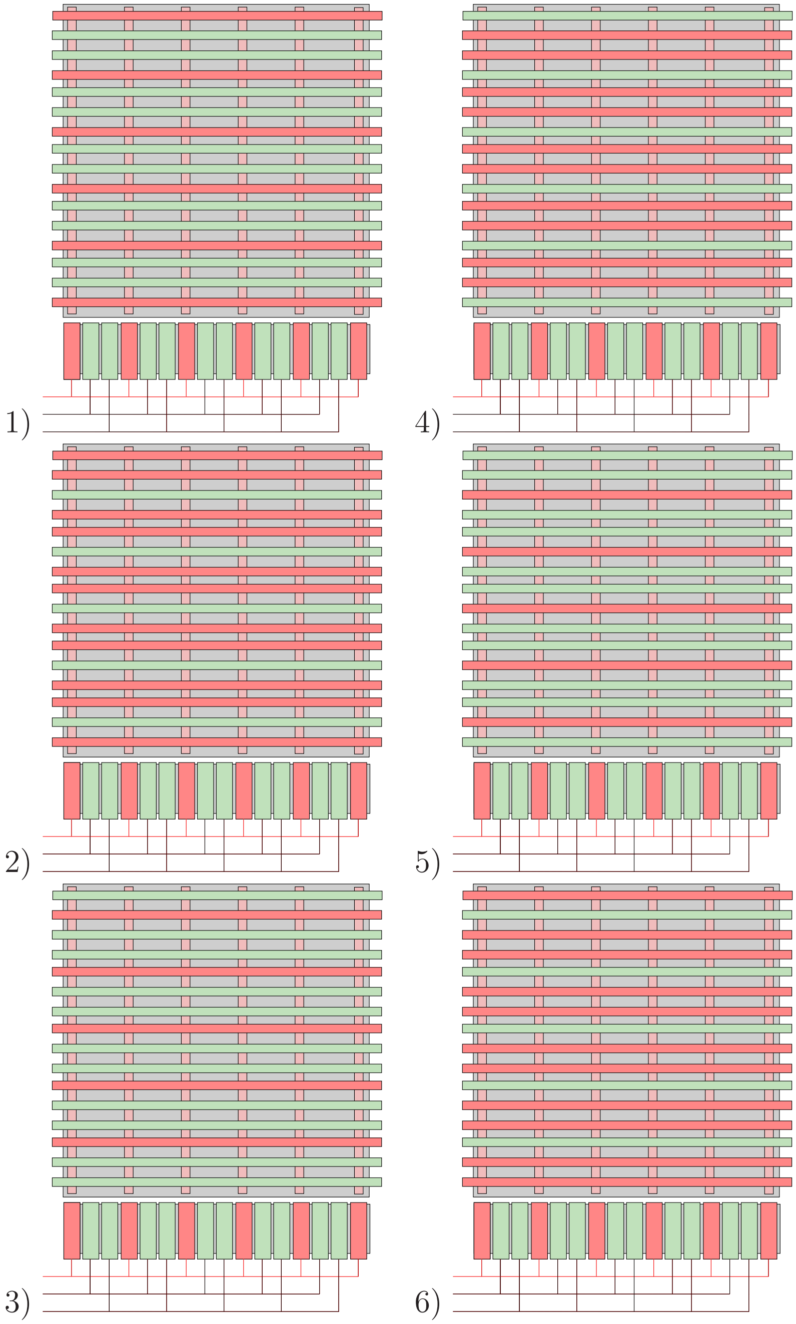

Figure 1.3: Illustrates the parallel readout clocking mechanism of a three-phase CCD. The potentials of of clocking lines are varied such that one row of pixels is moved towards the serial register at the bottom. Red symbolizes high potential. After state 6 the CCD goes back the state 1. During the exposure the CCD is in phase 1.

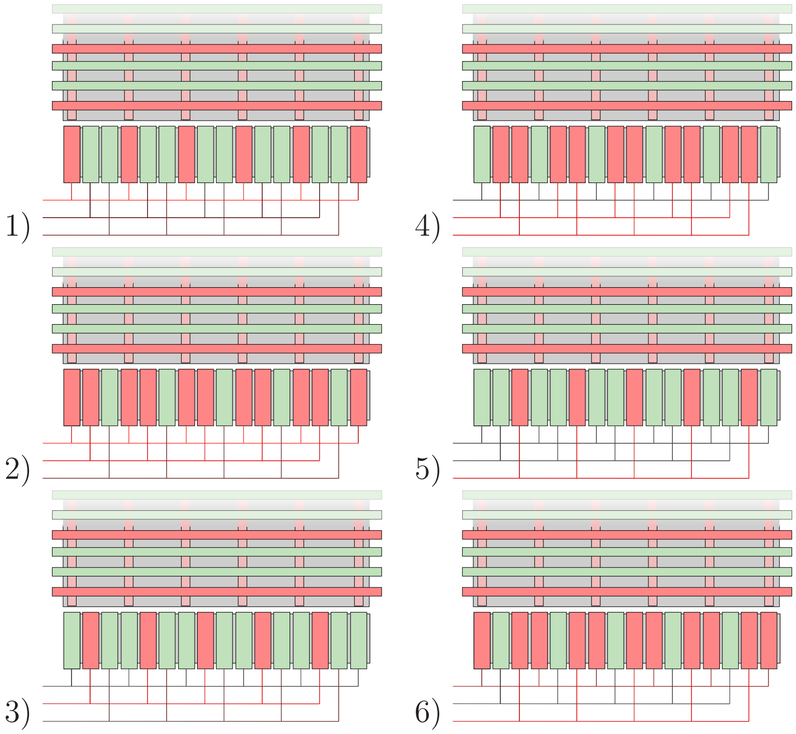

Figure 1.4: Illustrates the serial readout clocking mechanism of a three-phase CCD. Displayed is a closeup on the serial register.
The potentials of the serial register clocking electrodes are varied to move the row of pixels towards the sense node located at the lower right corner. The sequence from picture 1 to 6 shows moves the charge in the serial register by one pixel towards the sense node (to the right in this schematic). The sequence is repeated as many times as there are columns.
After all the charge is clocked out of the serial register it is set to phase 1 again and the next row is clocked into the serial register.

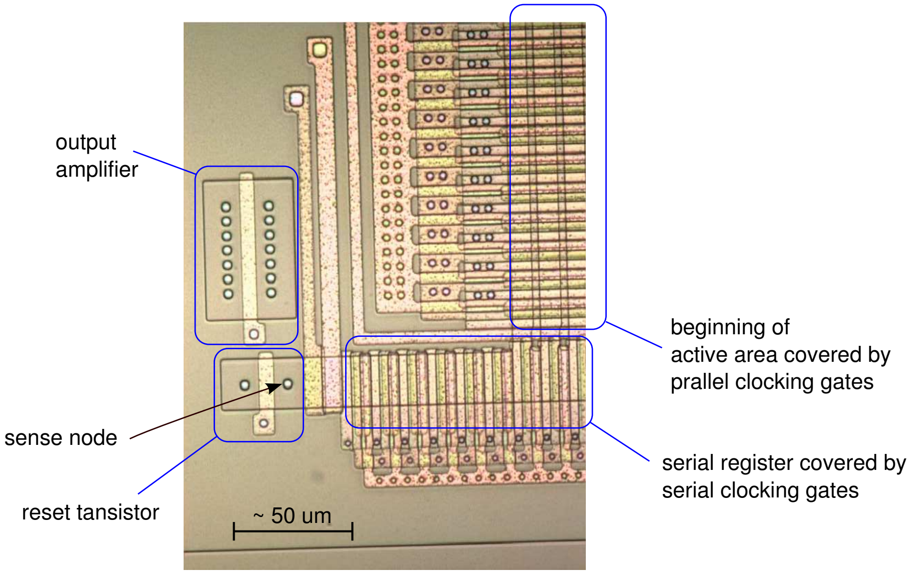

Figure 1.5: Shows a micrograph of the corner region of the LBNL CCD. The upper right region shows part of the optically active area of the CCD where the three phase strip electrodes cover the channels. Below this region one can see the serial register which ends at the reset amplifier further left. The gate of the output amplifier is connected to the sense node during a later processing step.

Reproduced from [23] with the kind permission of Stephen E. Holland

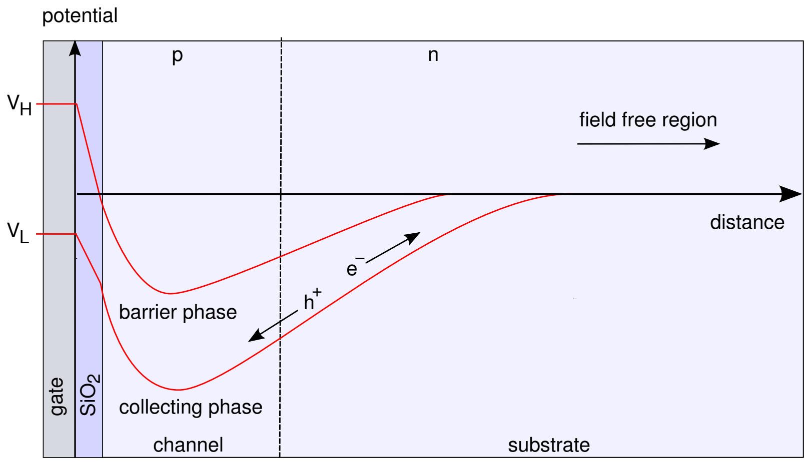

Figure 1.6: Shows the potential well which is formed by the channel implant during collection phase and during barrier phase, here for a p-channel device. Since the potential minimum is located deeper than the Si-SiO_2 interface, the electron holes do not come into contact with surface defects. This results in a improved charge transfer efficiency.

The serial register is typically wider than a column of the CCD and can therefore hold more charge. This becomes important when several pixels are binned. The electrodes of the CCD are usually called gates.

In literature the serial register is referred to as horizontal register, the parallel registers are referred to as the vertical registers for historical reasons.

In nowadays devices the channels are also doped. If electrons are used as signal carriers they are n-doped otherwise they are p-doped. This doping results in a buried channel. The charge carriers do not move along the silicon-silicon-oxide interface but in a channel underneath the surface. Since this avoids the contact of the signal carriers with surface defects, this technique improved the charge transfer efficiency dramatically (see 2.2).

This leads to the differentiation of n-channel CCDs and p-channel CCDs. n-channel CCDs use electrons as signal carriers. p-channel CCDs use electron holes.

Figure 1.6 shows the buried potential of a p-channel CCD.The image presents a cut through the CCD in the plane of a channel. Photons enter the silicon from the left. If their energy is sufficiently high they create an electron-hole pair within a few a microns. The resulting electron-hole is captured in the buried channel whereas the hole immediately moves away from the channel. The electodes which are set to high potential form a barrier and prevent the charge from moving freely through the channel. One or two electrodes between two barrier phase electrodes are set two low potential and collect the generated charge.

Astronomical devices

In a so called front illuminated device the light enters the CCD through the gate structure which would be from the left in figure 1.6. Although the gates are very thin this results in a great loss of detectable photons. The shorter the wavelength of the photon, the higher the probability that a photon gets reflected or absorbed by the gates.

Astronomical CCDs are therefore backside illuminated. The photons would enter from the right side in figure 1.6. If the CCD was as thick as a typical wafer ($\sim 600\ \mu m$), large parts of the substrate would be field free and most of the photons would be absorbed in a field free region. Without a field, generated charge-carriers diffuse also laterally from the point of their creation. The resulting image would be blurred - or as an astronomer would say, the point spread function would be very large - rendering such devices unusable.

Therefore backside illuminated devices have to be thinned. A typical astronomical CCD has a thickness of about 20 microns. They are thinned so that electrons which are created at the surface immediately experience a potential pulling them into the channels. Such thin devices are obviously very difficult to manufacture and to handle, resulting in a high price.

Below a photon energy of 2.5 eV - the direct bandgap energy of silicon - phonons are required for electron-hole pair generation in the silicon. This results in an increase of the absorption length and therefore a decrease of quantum efficieny above 500 nm (see Fig. 1.7). When the photon energies become compareable to the indirect bandgap energy of 1.12 eV, the absorption length can be more than 100 μm. So that thinning results in a low quantum efficiency in the NIR.

At long wavelengths light penetrates the silicon deeply enough to be reflected internally from the front side. The reflected light interferes with incident light in the silicon. The resulting fringing is a inherent problem of thinned devices.

1.2 CCD development at the LBNL

Super Nova Cosmology Project

Using type Ia supernovae as standard candles, in 1998 two groups ([40] and [38]) found evidence for the accelerated expansion of the universe.

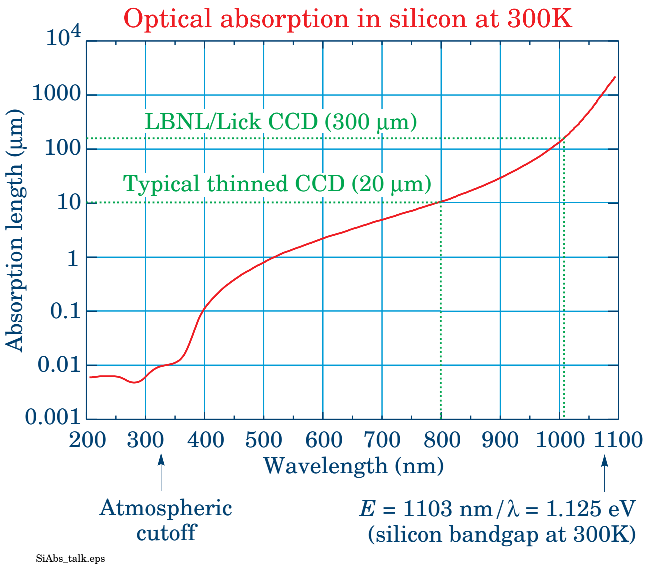

Figure 1.7: Absorption length in silicon, calculated using the parameterization of [41]. Reproduced from [17] with the kind permission of Donald E. Groom

A standard candle is an astronomical object of known luminosity. By comparing its luminosity to its observed brightness one can calculate the distance. Standard candles may be objects like Cepheid variables - stars with a periodic change in their luminosity which show a tight correlation between their period of variability and absolute brightness. Cepheid variables allowed Edwin Hubble 1923-1924 to show for the first time that Andromeda was not part of our Milky Way galaxy, but an entirely separate galaxy.

Although Cepheid variables may be used to measure the distances of the galaxys in our local group they are barely bright enough to allow to measure Hubble's constant [15] and can not be used for cosmology.

The most commonly accepted theory of type Ia supernovae is that they are the result of a carbon-oxygen white dwarf accreting matter from a nearby companion star, typically a red giant, until it reaches the Chandrasekhar limit. Once the white dwarf reached the Chandrasekhar limit it forms a super novae, a extremely violent event which reaches a typical absolute magnitude of -19.5. Since triggered by the Chandrasekhar limit, each type Ia supernovae has nearly the same light curve, i.e. brightness over time.

Having such a bright standard candle one can now compare their brightness and their redshift and try to extract cosmological parameters from this relationship.

From the cosmological principle (homogeneity and isotropy on large scales, modelling the matter as ideal fluid) Friedmann derived his famous equations

$$H^2 = \left(\frac{\dot{a}}{a}\right)^2 = \frac{8\pi G}{3}\rho + \frac{\Lambda}{3} - \frac{k}{a^2} \tag{1.1}$$

$$\frac{\ddot{a}}{a} = -\frac{4\pi G}{3}(\rho + 3p) + \frac{\Lambda}{3} \tag{1.2}$$

where ρ and p are the density and pressure of the ideal fluid, Λ is the cosmological constant, G is the gravitational constant, k gives the shape of the universe, and a is the scale factor. In these equations, c - the speed of light - is set to one, and would appear in the last term otherwise. The Hubble parameter H is the rate of expansion of the universe, a value that can change over time if other parts of the equation are time dependent - in particular the energy density, vacuum energy, and curvature (see [34] or [14]).

The first equation might be rewritten into the form

$$\frac{H^2}{{H_0}^2} = \Omega_R a^{-4} + \Omega_M a^{-3} + \Omega_\lambda - \frac{k}{a^2} \tag{1.3}$$

where Ω_R is the radiation density parameter, Ω_M is the matter (dark plus baryonic) density parameter, and Ω_λ is the cosmological constant or vacuum density parameter.

The cosmological constant was first introduced by Albert Einstein to force the equations to yield a static universe. He later revised his decision as the "greatest blunder of his life" when Edwin Hubble discovered the expansion of the universe by making use of the already mentioned Cepheid variables [24].

Now, the 1998 results [38] (see Fig. 1.9) which compare the standardized brightnesses of 42 high-redshift Type Ia supernovae (SNe Ia) ($0.18 < z < 0.83$) with 18 low-redshift SNe Ia found that for a flat universe $\Omega_\lambda = 0.72 \pm 0.08$ ($\Omega_M = 1 - \Omega_\lambda$) (i.e. a cosmological constant different from zero) and constrain the combination $0.8 \cdot \Omega_M - 0.6 \cdot \Omega_\lambda$ to -0.2 ± 0.1. These results are in good agreement with more recent data from combined cluster measurements and CMB results (see [36]).

. . . Such an acceleration requires an unknown component to contribute the majority of the energy density of the universe twice as much as the matter density. Researchers are intently designing theories to explain these observations as well as experiments to test the theories and probe the nature of this "dark energy". Type Ia supernovae observations have a clear, simple connection to the expansion of the universe that makes them excellent at probing the dynamics out to redshifts $z \approx 2$. *The apparent magnitude, or intensity, of the supernova is a measure of the distance and its redshift directly translates into the expansion factor, mapping out the recent expansion history of the universe. . . .* [33]

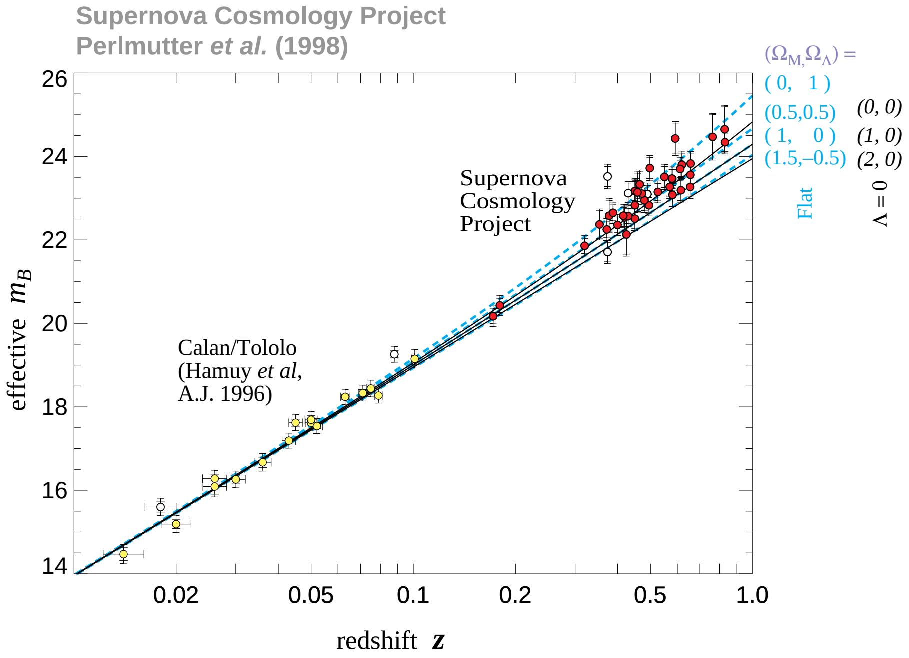

Figure 1.8: Hubble diagram published by the Supernova Cosmology Project.
Reproduced from [38] with the kind permission of Saul Perlmutter

The Super Nova Cosmology Probe

[33] continues:
. . . But we know almost nothing of the nature of the dark energy – its equation of state, ratio of pressure to density, $w = p/\rho$*, or whether this evolves, e.g.* w' *. These two quantities hold crucial clues to the underlying fundamental physics. . . . A next generation experiment needs to be carefully designed to probe the dark energy. But systematic uncertainties rather than merely paucity or imprecision of observations will be the key obstacle. The CMB is insensitive to time variation and can only provide a rough estimate of an averaged value of* w*, except for a small impact on the late time Sachs-Wolfe effect buried in cosmic variance. Gravitational lensing and the growth rate of large scale structure is promising, but needs to be separated from complicated nonlinear astrophysics. Supernovae studies directly measure the expansion dynamics and have a longer history than the various structure related methods. From this history a comprehensive list of possible systematics, and methods for accounting for them, have been developed and a new experiment is under design dedicated to exploring dark energy: the Supernova/Acceleration Probe (SNAP) satellite [36]. To investigate the dark energy and distinguish between classes of physics models we need to probe the expansion back into the matter dominated deceleration epoch, indeed over a redshift baseline reaching* $z > 1.5$ *. . .*

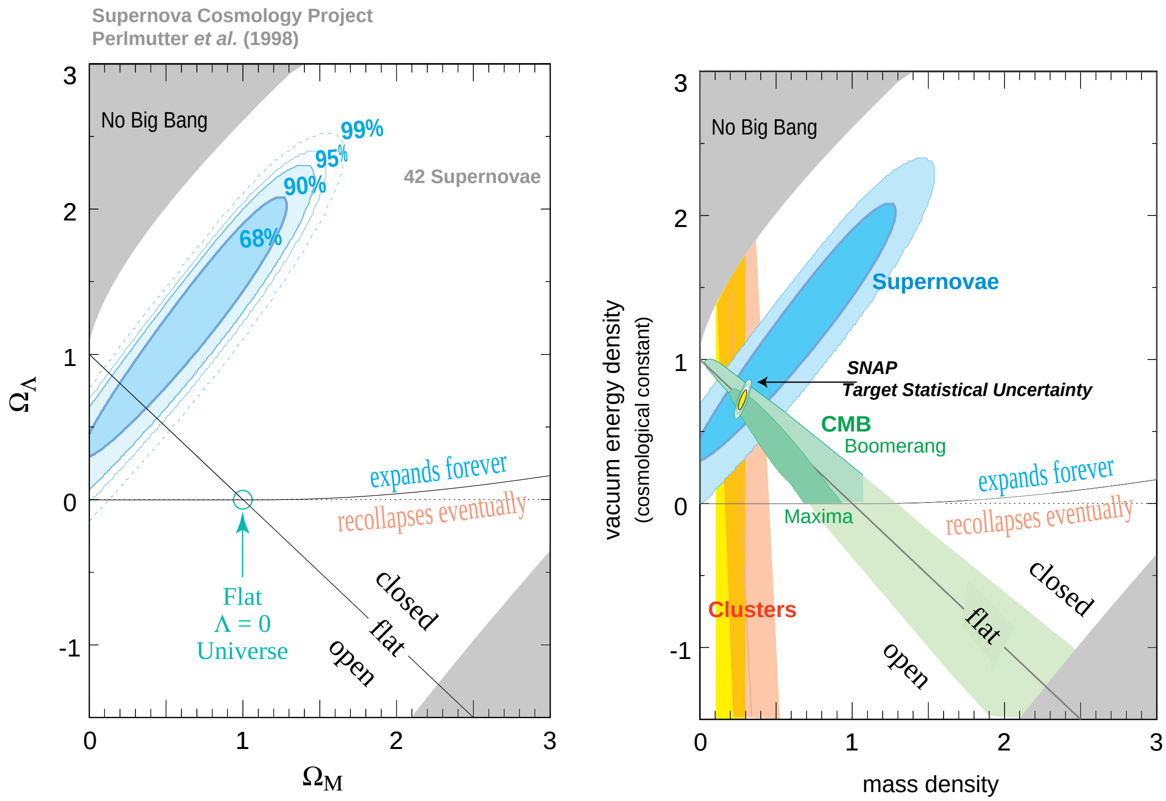

Figure 1.9: Results suggest the the expansion of the universe is accelerated. **left)** Constraints in the (Ω_m,Ω_Λ) plane, published by the Super Nova Cosmology project.

Reproduced from [38] with the kind permission of Saul Perlmutter

right) Compares SCP results with the 1998 published Bahcall et al. results on cluster studies [6] and the in 2003 published Spergel et al. CMB results [45]

Reproduced from [36] with the kind permission of Gregory Aldering

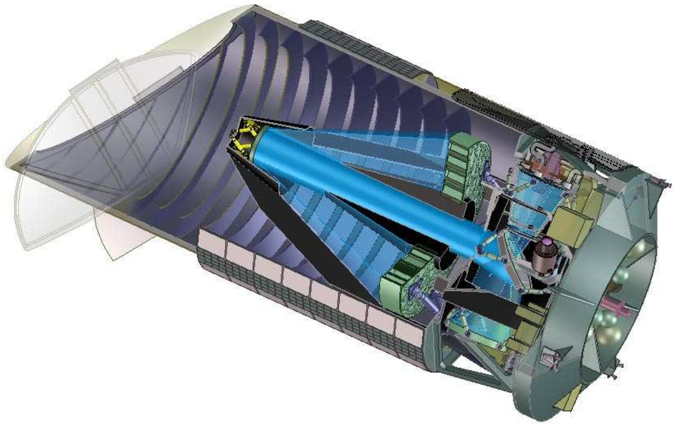

Figure 1.10: A cross-sectional view of the SNAP satellite. The principal assembly components are the telescope, optical bench, instruments, propulsion deck, bus, stray light baffles, thermal shielding and entrance door.

From the scientific requirements a space craft was designed, dedicated to the exploration of dark energy. The baseline concept of the Super Nova Cosmology Probe (SNAP) is a 2 meter space telescope with a large 0.7 square degree field of view. A 3-mirror anastigmatic assembly (see Fig. 1.10 and 1.11) will provide a flat focal plane. The focal plane (see Fig. 1.12) will be equipped with an optical NIR imager and a low resolution $R \sim 100$ spectrograph (see [30]). Both the imager and the spectrograph will cover a wavelength range of 350 nm - 1700 nm, allowing detailed characterization of Type Ia supernovae out to $z = 1.7$. The wide field imager consists of mosaic of 36 LBNL n-type high resistivity 3.5k × 3.5k CCDs (see 1.2) covering 0.34 square degrees and 36 2k x2k HgCdTe infrared detectors also covering 0.34 square degrees. Fixed filters will be placed in front of the detectors so that each piece of sky can be observed through each filter in a shift and stare mode of operation.

The SNAP experiment will be able to study supernovae over a redshift range of $0.1 \leq z \leq 1.7$ a much larger range than has been possible with the current ground-based measurements – over a wide wavelength range unhindered by the Earth's atmosphere and with much higher precision and accuracy.

LBNL CCDs

As part of the general detector research program the LBNL started developing CCDs in 1996 . The LBNL CCD was originally a spin-off of the high-energy detector development at the LBNL. On July 30 1996 200 × 200 pixel prototype produced the first astronomical image (see [20]).

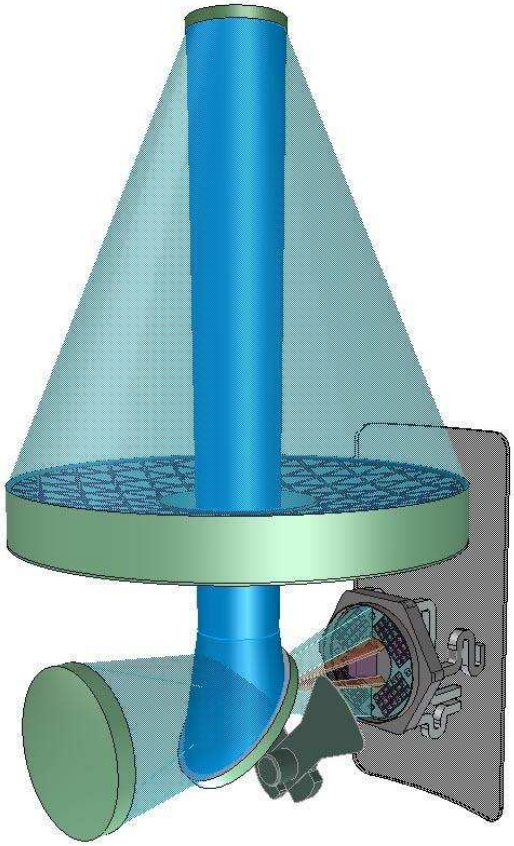

Figure 1.11: Shows the 3-mirror anastigmatic design for SNAP

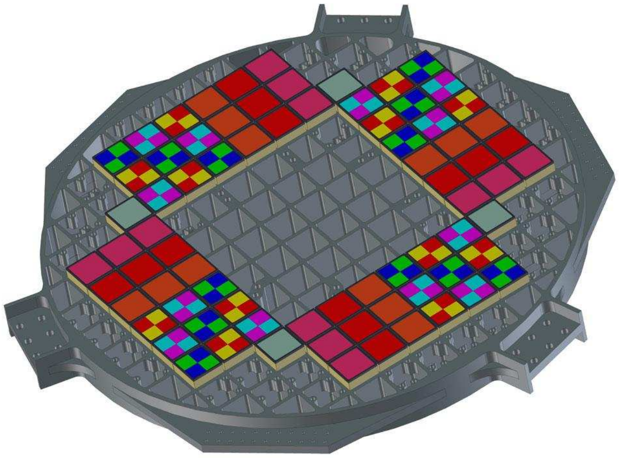

Figure 1.12: The SNAP mosaic camera is tiled with 36 3.5k × 3.5k high-resistivity thick backside illuminated CCDs and 36 HgCdTe detectors, covering a 0.7 square degree field of view. The detectors are arrayed to allow step and stare sky coverage in orthogonal directions while coping with the central obscuration that is necessary in a simple three-mirror anastigmat telescope design. Each CCD is covered with four fixed filters, while each HgCdTe has one fixed filter.

In contrast to many other devices in the market The LBNL CCD is a thick, backside illuminated, p-channel device. A p-doped channel is implanted in weakly doped high resistivity (10.000-12.000 kΩ) n-type silicon. *... The production of low dark current devices through backside gettering techniques in n-type silicon seemed to be more straight forward. ...* [22] Utilizing electron-holes as signal carriers showed to improve the radiation hardness [7] of these devices due to the lack of phosphorus-vacancy formation in the channels. Lower hole mobility is not and issue for the slow readout rates in astronomical devices.

The usage of high resistivity silicon and biasing through an backside ohmic contact allow for full depletion of up to 650 μm thick devices [29]. The large photosensitive volume greatly improves the quantum efficiency in the NIR (up to 90% at 900 nm).

The backside ohmic contact is formed by low-pressure, chemical-vapor deposition of in-situ doped polycrystalline silicon (ISDP). This layer can be made thin for good blue response, typically 10-20 nm, and is robust to over-depleted operation that is necessary both to guarantee full depletion across the entire CCD, and to improve spacial resolution [22]. Finally a SiO_2 layer acts as additional anti-reflective coating [22]. Currently another approach for backside contacting where the contact is formed through molecular beam epitaxy is tested to improve UV sensitivity (see Sec. 8.5.7).

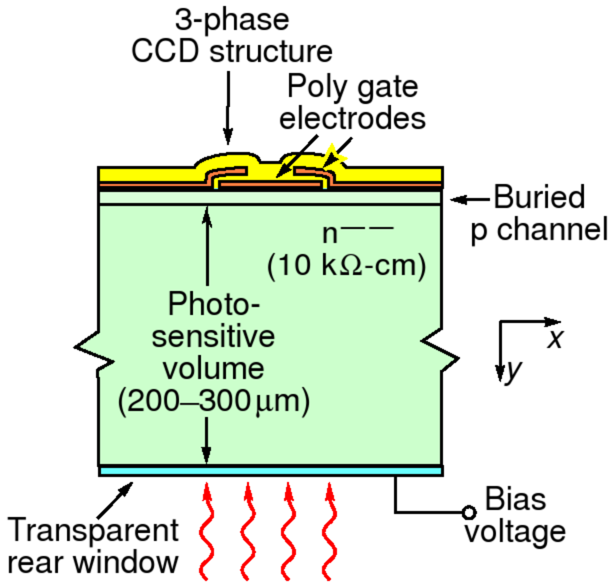

Figure 1.13: Crossectional diagram for the thick backside illuminated LBNL SNAP CCD.

The SNAP proposal would lead to a high number of devices which need to be fabricated. The fabrication has therefore been outsourced to DALSA, only the backside finishing is done at the Micro Systems Laboratory at the LBNL.

The SNAP V2 CCD

In 2005 the version 2 design was submitted to DALSA. It includes modifications to meet the more recent SNAP mission requirements. The SNAP V2 devices are 3512 × 3508 pixel large, four corner readout devices. The pixel size is 10.5 μm .

The design employes protective measures which allow to apply substrate voltages up to 206 V (see [29]). A point spread function of 4 μm was shown for a thinned 200 μm thick device at a substrate voltage of 80 V (see [13]).

A dark current as low as 0.62 $e^{-}/\text{pixel}/h$ at -140° C, a read noise as low as 3.6 e^{-} RMS and a serial CTE of 0.99999975 ± 1.4^{-7} and a parallel CTE of 0.99999988 ± 1.2^{-7} were measured for this device (see [29]) [2].

---

[2] An explanation of these terms is given in the next chapter.

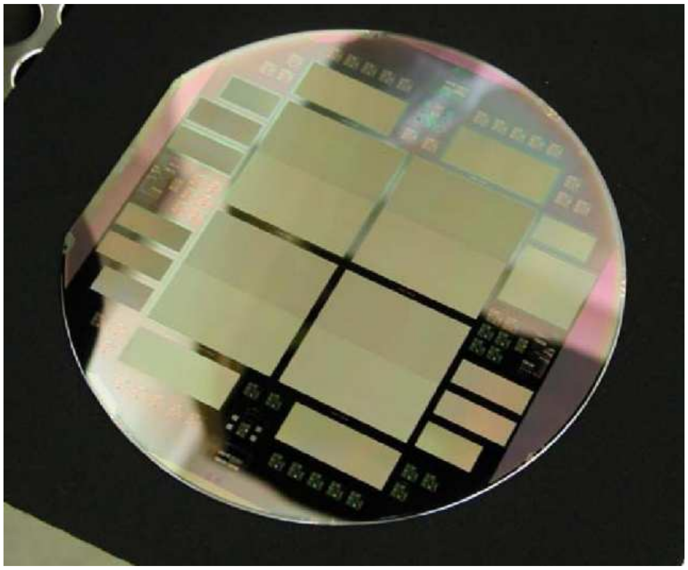

Figure 1.14: A 150 mm wafer with four 3.5k × 3.5k SNAP V2 type CCDs and various smaller CCDs and test structures.

CHAPTER 2

DEVICE CHARACTERISTICS

2.1 System gain

Since the analog digital conversion of the readout controller provides us only with some digital number for the pixel signal (ADU as in Analog Digital Unit), at some point one has to calibrate how many ADUs are measured per electron. The result of this calibration is the system gain [1]. A common way to measure the system gain is to expose the CCD to x rays which result from a radioactive decay. The energy spectrum of such x ray photons has typically very sharp lines. If an x ray photon of well known energy interacts with the silicon of the CCD it produces a certain number of electrons. If this number is known one basically has to identify the x ray events in the CCD image and to divide the signal in the event pixel by this number to obtain the system gain.

We use a ^{55}Fe x ray source. ^{55}Fe decays into ^{55}Mn which in turn emits x rays after the decay. When the ^{55}Fe nucleus absorbs a K-shell electron a x ray photon is generated when either an L- or an M-shell electron fills the resulting vacancy in the K-shell. In the L-shell case a 5.90 keV x ray photon is generated, in the M-shell case a 6.5 keV photon is generated where the production ratio of both is approximately seven to one (see chapter 2.3.2 in [25])..

Now this method proved to be very straight forward and useful for the very day gain calibration. Several problems occur when one tries to be accurate within one percent though.

First of all the number of electron hole pairs produced in silicon is relatively well known for room temperature. One often finds a different number which is the number of electron-hole pairs per eV of x ray energy ω.
It is

$$\omega(300K) = 3.66 \pm (0.02 \text{ to } 0.03)\frac{eV}{\text{e-h}} \tag{2.1}$$

(see [17]) which results in 1612 ± 13 electron hole pairs per K_α x ray. Traditionally the number of 1620 electron hole pairs per K_α x ray is used (see chapter 2.3.2 in [25]). Now as quoted in [17] this number is more likely to be

$$1570 \pm 13\frac{\text{e-h}}{K_\alpha} \tag{2.2}$$

---

[1] To avoid any confusion: One has to differentiate between the CCD's amplifier gain and the system gain. The system gain is the ratio of measured ADUs per electron. It is a function of the gains of all amplifiers between the CCD's sense node and the analog to digital converter as of the AD-converter itself.

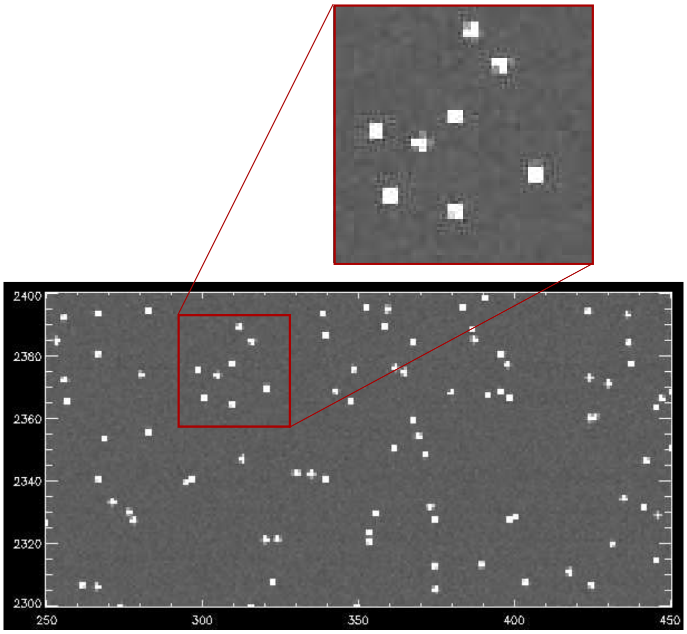

Figure 2.1: Shows a 100 × 200 pixel region of the thick backside illuminated device 105868-14-6 after ^{55}Fe x ray exposure. If the number of electrons which are generated during the absorption of the photon is known, one can calculate the system gain from such an image. The 36 × 36 pixel closeup shows the events are actually spread over several pixel.

at -140 C which is the operating temperature of the SNAP CCDs. Still this new number has about a one percent uncertainty.

Second, the identification of x ray event pixel in the CCD image is not trivial. The x rays penetration depth in silicon is only about 30 μm . Therefore in front side illuminated devices the x rays generate electron hole pairs close to the gate structure. Only if an x ray hits the edge or the corner of one pixel, the resulting charge might be spread over several pixel. The charge will usually be contained in one and in not more than four pixel. Now, SNAP CCDs are backside illuminated. The electron holes will travel several hundred microns through silicon before they get collected in the gate structure (see [16] and [13]). Depending on the strength of the depletion field and the device thickness the charge packet can spread out and end up in more than four pixel (see closeup 2.1).

Finally when integrating over a number of pixel to obtain the x ray signal, one has to substract the background signal. Each CCD is read out with a small voltage offset so that there is always a baseline of a couple of hundred to a couple of thousand ADUs. Ideally this basline is flat over the whole CCD. In the experiment though, shifts of the baseline were observed and have to be corrected for.

Chapter 6.1 will explain advanced algorithms we developed to be able to calibrate the gain more accurately.

Any one percent error directly results in a one percent error in the QE estimate. Since our self set error margins are small we looked into an alternative method for calibration the gain.

2.2 Charge Transfer Efficiency (CTE)

The charge transfer efficiency CTE denotes how much of the charge in one pixel actually gets transfered into the next pixel in a three phase clocking cycle. The importance if this parameter is easily understood if one imagines a CTE only as good as 99%. In a 100 × 100 pixel large CCD - a small device for nowadays standards - the charge of one pixel might get shifted as often as 100 times in the parallel direction before it reaches the serial register. Now, if during each clocking cycle only one percent of the charge is lost, only $0.99^{100} = 0.37 = 37\%$ of the original charge reaches the serial register.

The SNAP V2 devices are about 3600 × 3600 pixel large. In four corner readout mode the worst case pixel has to be shifted 3600 times. Obviously such a device would be unusable with a 99% CTE. Burried channel CCDs typically have a CTE of 0.99999% or higher.

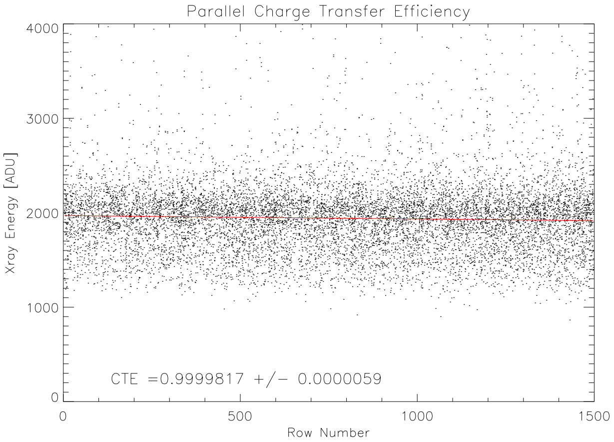

Figure 2.2: Shows the result of a typical CTE measurement for the frontside illuminated device 105868-15-10. The signal per pixel (in electrons) is plotted over the number of transfers. A line fit revealed a CTE of 0.99998167. This is actually a low CTE for this type of device. In this case the CTE is degraded because the device was exposed to 13 MeV protons.

Several methods exist to measure the CTE. We use ^{55}Fe - the same radiation as used in the gain calibration - for the CTE measurement. If the amount of electrons which result from a x ray photon absorption is known, one can estimate the CTE by simply comparing this number with the number of measured electrons at the readout amplifier. One actually does not even have to now this number since only the ratio is used in the calculation. Typically the signal per pixel is plotted vs. the number of times a pixel has to be transfered for one pixel to the other before being read out at the sense node. A line fit the gives the CTE. The actual algorithm goes through several iterations to separate the CTE in the parallel and in the serial direction.

Even though the CTE does not directly affect the QE measuremens, it might be an important obstacle to our gain calibration techniques (see Sec. 6.2 and 6.1).

2.3 Read noise

The CCD read noise denotes the noise caused by the CCD readout amplifier during read out. The two dominant noise source are the the thermal or white noise caused by the output amplifier impedance and the $1/f$ of flicker noise cause by surface interface states (see chapter 6.3 in [25]).

The read noise is usually measured by taking a dark image and calculating the pixel to pixel RMS variance in the resulting image. If one wants to measure the amplifier noise one has to substract the noise generated by the readout system. Here we will generally deal with the overall read noise which is the sum of both, the CCD amplifier noise and the readout system noise. Usually read noise is given in electrons RMS. From the image one first calculates the RMS of the pixel to pixel variance in ADU and then divides by the system gain. For good devices - and, as a matter of fact, on good days - we achieve a read which is a small as four electrons RMS. For our highly experimental setups a read noise of 20 electrons is not unusual though.

2.4 Dark current

Dark current in CCDs refers to the signal generation in the pixel without exposing the device to light. The CCD is based on the p-n junction. As other p-n devices too, a CCD pixel is subject to reverse leakage current. This leakage current is caused by intermediate-level centers or traps (see chapter 7.1.1 in [25]) associated with impurities or imperfections within the semiconductor or at the Si-SiO$_2$ interface. Usually the spontaneous generation of an electron-hole pair is highly improbable. A trap with an energy level in the center of the forbidden bandgap assists the generation of through a stepping process. The probability of the excitation of an valence electron to the trap level is much higher than its excitation to the conduction band energy and vice versa for electron holes. If these two processes occur simultaneously a electron-hole pair is generated. Depending on the type of CCD then either the electron or the hole can be captured in the potential well of a pixel. The dark current is a strong function of the temperature, [25] derives

$$D_R(e^-) \sim T^{1.5} e^{-E_g/(2kT)} \tag{2.3}$$

where D_R is the is the average dark current generated (e^-/sec/pixel), T is the temperature, E_g is the bandgap energy (also a function of temperature) and k is Bolzmanns' constant.

Therefore scientific CCD have to be operated cold, otherwise the dark current at room temperature would immediately flood the CCD. The operating temperature for SNAP CCDs is -140 C. Typical values for the dark current of SNAP devices are in the order of a few electrons per pixel per hour. The so called Multipinned Phase (MPP) device (see chapter 4.2.12 [25]) was developed to suppress surface dark current which allows this CCD to be operated at room temperature. This technique is not employed in SNAP CCDs.

2.5 Quantum efficiency

The quantum efficiency (QE) of a CCD denotes its efficiency in detecting photons. QE is the ratio of incident photons to generated electron-hole pairs.
Of course photons of sufficient energy might actually generate more than one electron

but this does not happen for photons of energies below 3.1 eV or 400 nm (see p.26 [25]). The gain calibration and the CTE measurement using ^{55}Fe method was already mentioned, here one x ray photon actually generates in the order of one and a half thousand electrons. [25] differentiates between interacting QE_I and QE. He defines

$$QE = \eta_i \mathrm{QE}_I$$

where η_i is the quatum yield, the number of signal electrons per interacting photons. QE_I specifies the ratio of interacting photons to total incoming photons. Where QE_I is the actually interesting number – since it tells how many of the incident photons we are able to detect – it is the QE we actually measure. For wavelengths above 400 nm $\eta_i = 1$ and $QE = \mathrm{QE}_I$.

As explained in section 1.1 the gate structure limits the QE of frontside illuminated devices. In section 8.5.5 the QE of such a front side illuminated device is shown. For backside illuminated devices the QE in the blue is limited due to absorption in backside layers like ohmic contacts. In the red the QE is limited by the bandgap energy of silicon (see Sec. 1.1) where the silicon becomes transparent. Within this range reflection off the backside is the main limiting factor, almost each photon penetrating the CCD's surface is detected. Depending on the AR coating a QE from 90% up to almost 100% is typical.

Fig. 2.3 shows the QE of a LBNL CCD. At about 900 nm the CCD starts to become transparent. In the blue, absorption in the backside polysilicon layer of the CCD becomes dominant. This effect reduces the QE for wavelengths below 500 nm. Between 500 nm and 900 nm we see an internal quantum efficiency of close to 100%.

2.5.1 QE measurement

Typically the quantum efficiency of a CCD is measured by exposing the device to flat fields i.e. very uniform light fields at a number of different wavelengths and comparing the resulting CCD signal to the previously or simultaneously measured light intensity. In most setups the light intensity is measured using a calibrated photodiode. This means the quantum efficiency of the photodiode has to be known. The calibration is typically provided by the manufacturer of the photodiode. Uncertainties in this calibration are obviously very problematic for the accuracy of the QE measurement.
The QE is then measured as

$$\mathrm{QE}_{\mathrm{CCD}} = \frac{e \cdot S_{\mathrm{CCD}}}{G \cdot T \cdot I_{\mathrm{PD}}} \cdot \mathrm{QE}_{\mathrm{PD}} \cdot A_r \tag{2.4}$$

where S is the mean CCD signal in analog digital units ADU, G is the system gain here defined in ADU/e^-, T is the exposure time, I_{PD} the photocurrent of the

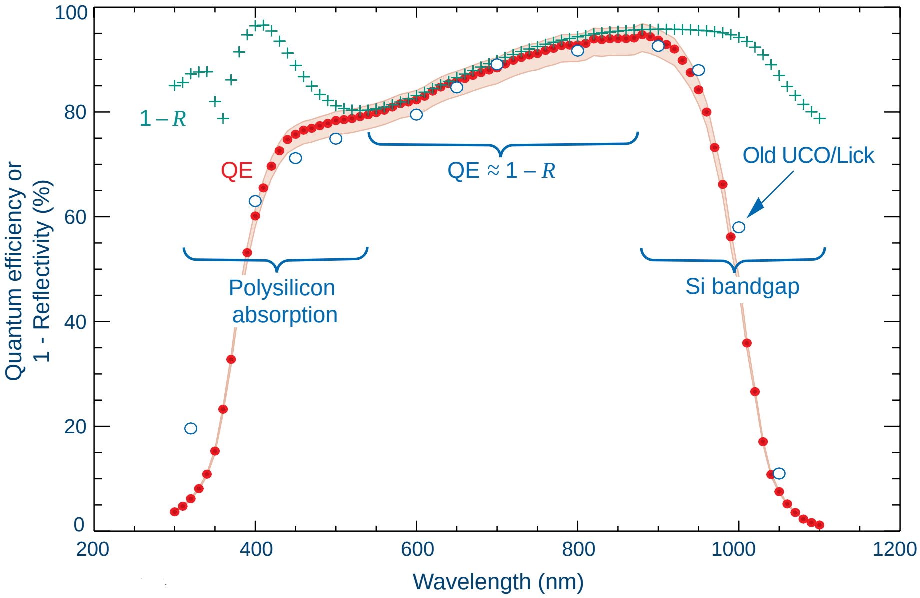

Figure 2.3: The expected quantum efficiency and one minus the reflectivity of a CCD. For $\lambda > 900$ nm silicon becomes transparent (bandgap). For $\lambda > 600$ nm absorption in the polysilicon layer of the CCD becomes dominant. For 600 nm $< \lambda <$ 900 nm the QE is close to $1 - R$.

Reproduced from [17] with the kind permission of Donald E. Groom calibrated photodiode, $\mathrm{QE}_{\mathrm{PD}}$ the quantum efficiency of the photodiode, λ is the wavelength and $A_r = A_{\mathrm{pd}}/A_{\mathrm{pixel}}$ is the area ratio between the photoactive area of the calibrated photodiode and one CCD pixel.

2.5.2 QE Verification

Reason for verification [2]

Our QE measurement is based on a calibrated photodiode. The CCD is illuminated with a monochromatic uniform light field. The QE is is calculated from equation 7.5. Uncertainties in the exposure time and the area ratios are controllable. Due to the large number of pixels the mean signal also has a small uncertainty.

The QE of the calibrated photodiode is a rather problematic factor. We have to rely on the calibration of the manufacturer. The calibrated photodiode was purchased from Hamamatsu. Hamamatsu does provide a “final inspection sheet” (see Fig. 4.24) showing a plot of photosensitivity vs. wavelength and a table listing the photosensitivity in mA/W and QE in percent. Hamamatsu does not provide an estimate of the uncertainty of their calibration. Obviously this makes error estimates difficult.

We regularly open the dewar to exchange the device to test. Each opening of the dewar brings possibly contaminations into the system and onto the photodiode. We observed contamination of our dewar system, the photodiode and the CCD itself. Actual measurements of the QE showed variations of up to 7% within three different days. Other groups observed aging effects of their photodiodes. Surface contamination of the photodiode may invalidate calibration of the photodiode. In similar setups, aging of calibrated photodiodes has caused inaccurate QE estimations.

Just as important is an exact knowledge of the system gain. Uncertainties of either the gain or the calibration are the most significant sources of systematic errors. The gain calibration using ^{55}Mn K_α x rays from ^{55}Fe decay [25] became standard in the SNAP CCD group at the LBNL. Historically a conversion factor of 1620 e^-/γ is used. This number is based on the bandgap energy of 3.64 eV of silicon at room temperature. The number of measurements of the larger bandgap energy at -140°C which is the operating temperature of our CCDs are smaller in number. After a review of the existing literature [17] we moved towards using 1580 e^-/γ. Other gain measurements using a modified photon transfer [8] curve show good agreement with this number and an uncertainty of about 0.2%.

The search for systematics and ways to verify the QE measurements has been the major part of this work. Contaminations proved to be so difficult to eliminate

---

[2] Summary of [12].

that we implemented the measurement in the photodiode mode which allows to measure the QE at room temperature. This was inspired by the Round Robin measurement which also compared result from our QE setup to the results of eight other groups. In this work a reflectometer was implemented to measure the specular surface reflectivity of our CCDs. It was specifically designed to be able to cope with the low reflectivity resulting from the AR coatings.

Reflectivity

As explained in 2.5 reflection is the limiting factor for the QE in the wavelength range from 500 nm to 900 nm. Here we expect

$$\mathrm{QE} = 1 - R - T \tag{2.5}$$

where R refers to the reflectivity and T to the transmission. If the backside is coated, absorption in the coatings might decrease the quantum efficiency. In the case of LBNL CCDs we found a significant absorption in the backside ohmic contact ITO layer and possibly in the poly silicon layer which allows the biasing of these devices. More generally

$$\mathrm{QE} \leq 1 - R \tag{2.6}$$

must always be true. We have implemented a setup to measure R directly. Reflectivity is measured in two steps, first measuring the intensity of a probe beam directly and then measuring the intensity of the reflected beam.

PD mode

The complication of having to calibrate the gain can be avoided by measuring the quantum efficiency in the photodiode mode. All clocking lines of the CCD are left floating or are grounded. The connection is made to the drain of the reset MOSFET which is connected to the signal channel.

In normal thinned CCDs the substrate is grounded. The photocurrent which is generated in the signal channel is than measured between the reset drain and the substrate. The quantum efficiency is then

$$\mathrm{QE} = \frac{\mathrm{QE}_{\mathrm{PD}} \cdot I_{\mathrm{CCD}} \cdot A_{\mathrm{PD}}}{I_{\mathrm{PD}} \cdot A_{\mathrm{CCD}}} \tag{2.7}$$

where QE_{PD} is the quantum efficiency of the calibrated photo diode, I_{CCD} is the photocurrent measured at the reset drain [3], I_{PD} is the photocurrent measured from the photodiode, A_{CCD} and A_{PD} are the active areas of the CCD and the photodiode.

---

[3] Since we bias our CCDs we actually measure a combination of dark current and photocurrent. We therefore need to measure the dark current separately and substract it. Section 7.2 will discuss this issue in greater detail.

This method allows to measure the QE at room temperature. In CCD mode the dark current would saturate the pixels even during the readout time. In PD mode the photocurrent is drained at all times and measured with a current meter. To operating temperature of LBNL CCDs is -140°C. A measurement at room temperature avoids contamination. One can actually measure without a dewar which also eliminates the dewar window.

Since we are dealing with LBNL CCD the substrate has to be biased above the depletion voltage. This biasing results in a large dark current. For a reasonable light intensity we actually found the dark current to be twice as large as the photo current. The dark current is extremely temperature sensitive (see Sec. 2.4). It was questioned whether one could measure the QE of LBNL CCDs in PD mode at room temperature despite the large dark current.

Round Robin

The Round Robin measurement directly compares the results of our QE setup to other groups results. Eight different groups, including the CCD group at the LBNL measured the quantum efficiency of the same device. The thin, backside illuminated CCD was measured at room temperature in the photodiode mode. The photodiode mode measurement simplified the mounting (since no dewar is needed) and the wiring (only two connections to the CCD are made).

CHAPTER 3
ANTIREFLECTIVE COATINGS AND QE PREDICTION

3.1 Coatings

The reflectivity of silicon would not allow to achieve a quantum efficieny in the order of 90% (see Fig. 3.1) without antireflective coatings.

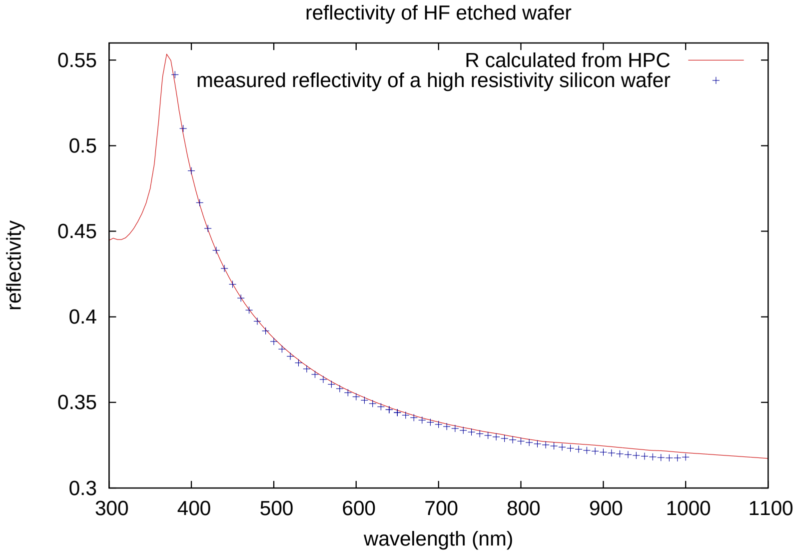

Figure 3.1: Shows the reflectivity of silicon as calculated using the constants given in the [10] from $R = \frac{(n-1)^2+k^2}{(n+1)^2+k^2}$ and the measured reflectivity of a high resistivity wafer of the type which is used for the LBNL CCD production.

In the case of LBNL CCDs the thickness of the indium tin oxide (ITO) backside ohmic contact layer is chosen so that it forms one of the antireflective (AR) coatings. A silicon dioxide layer on top of these acts as additional AR coating.

In [18] a code based on the transfer matrix approach was developed to calculate the reflectivity of a CCD with anitreflective coatings of given thickness. This code allows to design coatings for either flat response - close to constant QE over a broad wavelength range - or high infrared sensitivity. It calculates the reflection and transmission coefficients for the stack of coatings and the silicon substrate. The quantum efficiency is assumed to be the result of

$$QE = 1 - R - T - a_{\text{poly}}$$

where R and T are the reflection and the transmission coefficients of the CCD, and a_{poly} is the absorption in the poly silicon layer on the backside. Absorption in the ITO contact layer is neglected. The frontside of the CCD is simulated as silicon-air interface, the gate structure on the frontside is neglected.

Despite of these simplifications the calculated quantum efficiencies gave a good estimate of what the QE of the actual CCD would look like. It allowed the design of the anitreflective coating of the LBNL CCDs.

Measurements in this work show a discrepancy between the actual data and the reflectivity (see 8.5.4). The QE is lower than expected. In the range from 500 nm to 900 nm the QE proved to be lower than eq. 3.1 suggested.

To see whether the loss could be due to absorption in the ITO coating the existing code was extended to include absorption in the backside coatings. The code was first reimplemented in JAVA, before access to the old code was granted. After it was proven to produce the same results, the JAVA version was than extended to include absorption.

3.2 QE prediction

3.2.1 Transfer matrix approach

Our QE calculation uses the transfer matrix approach. One solves the boundary value problem for the electric field for one film of given thickness.

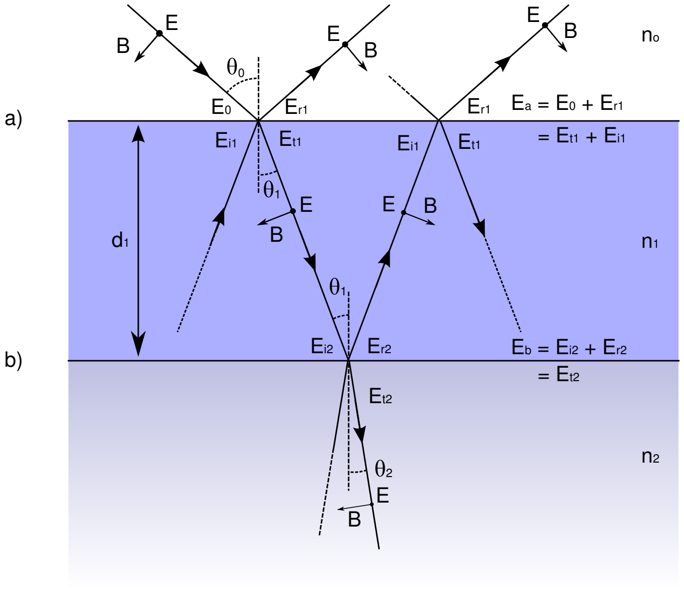

Figure 3.2: Reflection of a beam from a single film. The incident electric field magnitude is E_0, the net reflected magnitude from surface a is E_{r1}, and the transmitted magnitude is E_{t2}. The fields (E_a,B_a) and (E_b,B_b) are related via the transfer matrix.

The fields in figure 3.2 at the front surface a) of the layer and the backside surface

b) are related over the equation (see [37] and [18]):

$$\begin{pmatrix} E_a \\ B_a \end{pmatrix} = \begin{pmatrix} \cos\delta & \frac{i\sin\delta}{g_1} \\ ig_1\sin\delta & \cos\delta \end{pmatrix} \begin{pmatrix} E_b \\ B_b \end{pmatrix} \equiv M \begin{pmatrix} E_b \\ B_b \end{pmatrix} \tag{3.1}$$

Where $g_1 = n_1 \cos\theta_{t1}$ and $\sqrt{\epsilon_0\mu_0}$ was set to 1 since it will cancel out in the calculation anyways.
The phase shift was given by [37] as

$$\delta = \frac{2\pi d n_1}{\lambda}\cos\theta_{t1} \tag{3.2}$$

. Now, [18] included the absorption by introducing the absorption length l

$$\delta = \frac{2\pi d n_1}{\lambda}\cos\theta_{t1} - \frac{id}{2l}\cos\theta_{t1} \tag{3.3}$$

or the complex index k

$$\delta = \frac{2\pi d}{\lambda}(n_1\cos\theta_{t1} + \frac{ik}{\cos\theta_{t1}}) \tag{3.4}$$

. The transfer matrix can be calculated separately for each layer in the CCD. The fields at surface a) and surface N) are then related via the equation.

$$\begin{pmatrix} E_a \\ B_a \end{pmatrix} = M_1 M_2 M_3 ... M_N \begin{pmatrix} E_N \\ B_N \end{pmatrix} \tag{3.5}$$

The complex reflection coefficient is defined as the ratio of the incident and the reflected field strength, the complex transmission coefficient is defined as the ratio of the incident and the transmitted field strength (see [37]).

$$r \equiv \frac{E_{r1}}{E_0} = \frac{g_0 m_{11} + g_0 g_s m_{12} - m_{21} - g_s m_{22}}{g_0 m_{11} + g_0 g_s m_{12} + m_{21} + g_s m_{22}} \tag{3.6}$$

$$t \equiv \frac{E_{tN}}{E_0} = \frac{2g_0}{g_0 m_{11} + g_0 g_s m_{12} + m_{21} + g_s m_{22}} \tag{3.7}$$

with

$$\begin{pmatrix} m_{11} & m_{12} \\ m_{21} & m_{22} \end{pmatrix} = M = M_1 M_2 M_3 ... M_N \tag{3.8}$$

then

$$R = \|r\|^2 \tag{3.9}$$

$$T = \|t\|^2 \tag{3.10}$$

$$\tag{3.11}$$

Now, [18] assumed

$$QE = 1 - R - T \tag{3.12}$$

and for the LBNL CCD used

$$M = M_{\mathrm{SiO_2}}\ M_{\mathrm{ITO}}\ M_{\mathrm{poly}}\ M_{\mathrm{Si}} \tag{3.13}$$

for wavelengths $\lambda \geq 400$ nm.

Below 400 nm absorption in the polylayer is modelled on top of that. The most conservative approach is to assume that all the charge generated in the poly layer is lost through recombination or other processes. The transfer matrices for the quartz layer, the ITO layer and a polysilicon layer are calculated and multiplied

$$M_{\mathrm{AR}} = M_{\mathrm{SiO_2}}\ M_{\mathrm{ITO}}\ M_{\mathrm{poly}} \tag{3.14}$$

from this – using equation 3.6 – the reflection and transmission coefficients $R_{\mathrm{AR}} = \|r_{\mathrm{AR}}\|^2$ and $T_{\mathrm{AR}} = \|t_{\mathrm{AR}}\|^2$ for the backside coating stack are calculated. The absorption in the backside coatings is then

$$a_{\mathrm{AR}} = 1 - R_{\mathrm{AR}} - T_{\mathrm{AR}} \tag{3.15}$$

and the quantum efficiency is

$$QE = 1 - R - T - a_{\mathrm{AR}} \tag{3.16}$$

Between 400 nm and 600 nm some deviation between theory and measurements was observed. The measured QE was lower than the predicted QE (see Sec. 8.2). Below 400 nm the measured QE was higher than the estimate possibly to the too conservative assumption that all charge generated in the poly silicon layer is lost through recombination.

Measurements of the reflectivity and the QE showed similar differences. For wavelengths below 500 nm there is no transmission of light through the silicon and it should be:

$$QE = 1 - R_{\mathrm{meas}} - a_{\mathrm{AR}} \tag{3.17}$$

In an attempt to find an explanation for the discrepancy, the absorption in the ITO layer which was neglected in [18] is now included in the model. Although this decreases the difference between measurement and the model it does not fully explain the experimental result (see Sec. 8.2).

It was suggested the the optical properties of our ITO recipe are significantly different for those we use for the calculation. Follow up measurements of the reflectivity and the transmittance of an ITO layer and an combined ITO and SiO_2 layer deposited on the piece of quartz did not explain the differences so far.

A nonlinear fit, using the thicknesses of the coatings as parameters, suggests that actually the polysilicon layer might be thicker than expected. An increase of the layer's thickness produces a curve which is in relative good agreement with the measurement.

This might point to a problem in the processing of the waver, resulting in a too thick polysilicon layer. Diffusion of dopants into the silicon substrate might also create a field free region at the surface preventing charge from getting transferred into channels. This question remained unanswered up to the submission of this work.

CHAPTER 4

QE SETUP

4.1 CCD mode

4.1.1 Experimental apparatus

Overview

The setup follows the canonical scheme as described in [27], [32], [5], [19], [35]. A xenon arc lamp serves as light source. Xenon was chosen for higher light intensity in the UV compared to the infrared output.

A monochromator allows to select the wavelength of interest. The monochromator is equipped with filterwheels to limit stray light and to suppress higher order refractions. A 20 inch integrating sphere attached to the output port of the monochromator provides uniform illumination of the CCD.

Due to its operating temperature of -140 °C the CCD is placed inside a dewar. The dewar window faces the output port of the integrating sphere. A 80 cm long dark box which is placed between the sphere and the dewar provides an almost normal angle of incidence a the CCD's surface. Not-canonical is the placing of the calibrated photodiode inside the dewar right next to the CCD. We actually placed two calibrated photodiodes next to the CCD to monitor for possible contaminations (see Sec. 4.3.2). The CCD and each photodiode are separately temperature controlled.

Placing the photodiodes inside the vacuum makes prior calibrations of the dewar window unnecessary. It also simplifies the coplanar alignment of the photodiodes and the CCD . A large shutter is attached to the output port of the sphere to control the exposure. A ARC GenII controller CCD readout controller with modifications for the SNAP high voltage design is used to read the CCDs out. Finally the whole setup is automated using a off the shelf Linux PC.

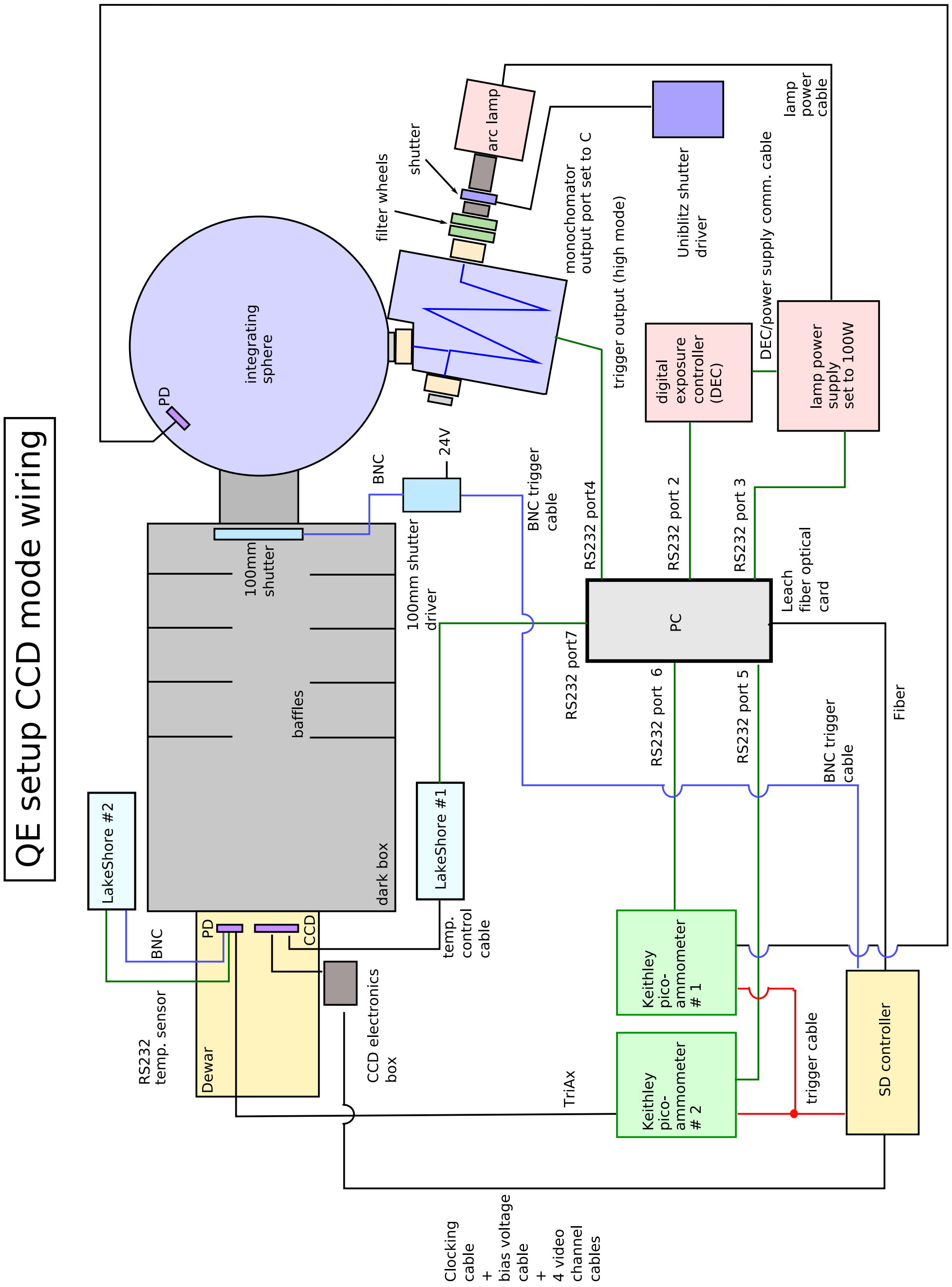

Figure 4.1: Overview of the quantum efficiency setup.

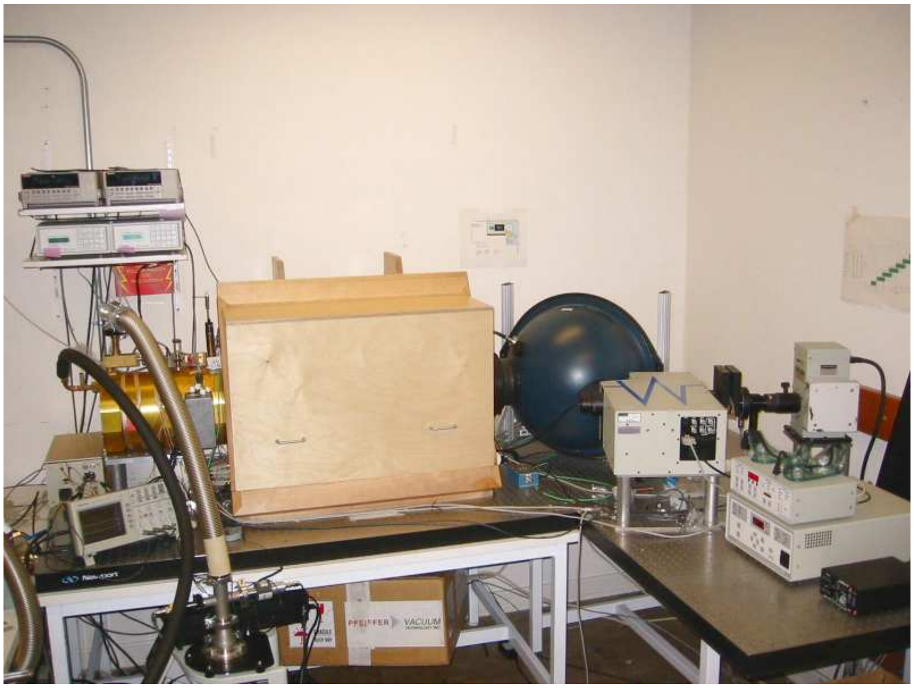

Figure 4.2: Overview of the QE setup. On the right one can see the light source and the monochromator. The monochromator feeds into the blue 20 inch integrating sphere. The sphere is attached to a 80 cm long dark box. The golder dewar on the left holds the CCD and two temperature controlled photodiodes.

It follows a detailed description of the QE setup. I will follow the beam path while describing the components. A more detailed description may be found in [17]. The setup underwent some smaller modification since its publication.

Light source

A 100 W Xenon arc lamp was chosen as light source. It provides a high blue and UV output and relatively low IR output compared to other quartz or halogen lamps (see Fig. 4.3).

Xenon has strong emission lines in the infrared (especially 823 nm and 835 nm [1]) which have to be dealt with. When the QE scan procedure reaches these wavelengths the CCD is easily saturated by the high light intensity. Instead of shortening the exposure time we decided to control the light intensity using the motorized slits (see 4.1.1) of the monochromator sacrificing a constant bandwidth.

Light source stabilization

Spectra Physics also sells a so called digital exposure (DEC) controller which allows to predefine exposure times or doses and may be used as shutter trigger.

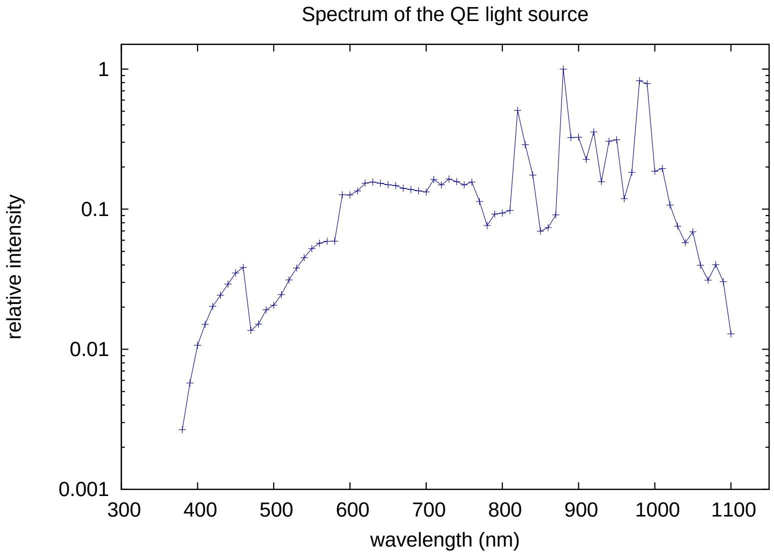

Figure 4.3: Shows the spectrum of the QE setup lightsource. The spectrum was measured with a photodiode through the optical fiber which is attached to the lateral output port of the monochromator. The UV light intensity is - due to absorption in the fiber - actually higher for the axial port than measured here. This spectrum is a product of the Xe spectrum and the transmission of the optical filters at the entrance port of the monochromator. The strong emission lines of Xe at 823 nm and above can easily be seen.

Its maybe most important feature is a feedback light stabilization. A temperature controlled photodiode - which is part of the DEC - provides the feedback signal. A beamsplitter was placed between the lightsource and the monochromator. The idea was to use the white light for feedback stabilization. If possible one would not have to worry about resetting the feedback loop when changing the wavelength.

After extensive measurements of the resulting light stability we decided that a beamsplitter at this point is not useable as source for the feedback signal. We observed drifts in the light intensity, possibly due to the strong heating of the beamsplitter by the arc lamp and resulting deformations.

Rather successful was the attempt to stabilize when the feedback photodiode was attached to one of the smaller output ports of the integrating sphere. We achieved light stability as good as 0.1% (standard deviation).

Finally we decided that the error introduced by changes in the light stability without feedback are small enough to be ignored. Still the feedback stabilization is a crucial part of our reflectivity measurement (see chapter 5).

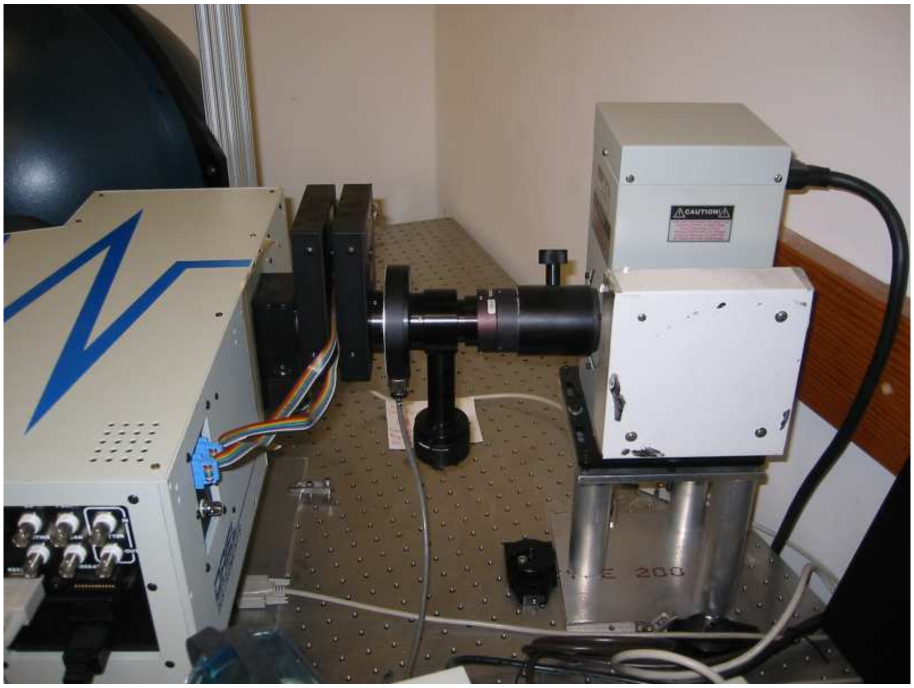

Figure 4.4: The light source of the QE setup. On the right one can see the housing of the Xe arc lamp. The arm pointing downwards is part of the beam splitter which we tried to use as source for a feedback signal for light stabilization. The shutter #1 is located right behind the beam splitter. The two black boxes on the left are the filter wheels at the entrance port of the monochromator.

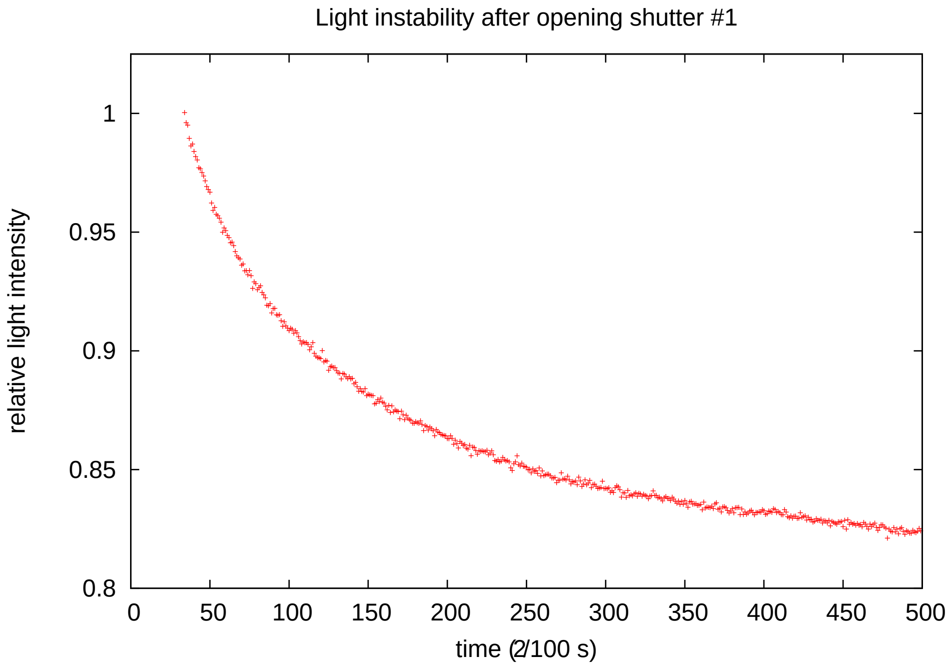

Figure 4.5: Shows the light stability after opening shutter number one. Even though stabilized, the light intensity drops by about 20% over a time of about 10 s.

Shutter No. 1

A first shutter is placed between the light source and the monochromator. Using a shutter with blank blades assures the the blades are not damaged by the high light intensity. We observed the light intensity to be unstable at the five percent level after opening this shutter due to the light which was suddenly not reflected back into the lamp any more. We were therefore unable to use this shutter for the QE measurements. It proved to be useful for later gain calibrations experiments though (see 6.2).

Monochromator

On the basis of other groups work the Oriel M-257 Monochromator was chosen. The monochromator has three ports. A automated mirror allows to toggle between two of the ports. We use the fixed port A as input port and the two other ports B and C as output ports. Port B feeds into the integrating sphere. An optical fiber attached to port C delivers the light for the reflectometer.

Filter wheels The monochromator is equipped with two filter wheels at the entrance port to suppress higher order refractions and to limit stray light. The filter wheels have five openings each. One opening on each wheel is left open resulting total of eight filters. A combination of colored glass and short and long pass filters

Stack	**Part #**	**Type**
Colored glass filters		
1	Hoya U340	280 nm-370 nm
2	Schott BG 28	380 nm-500 nm
Dielectric filters		
3	LL-450-F	Long pass 450 nm
3	LS-600-F	Short pass 600 nm
4	LL-550-F	Long pass 550 nm
4	LS-700-F	Short pass 700 nm
5	LL-650-F	Long pass 650 nm
5	LS-800-F	Short pass 800 nm
6	LL-750-F	Long pass 750 nm
6	LS-900-F	Short pass 900 nm
7	LL-850-F	Long pass 850 nm
7	LS-1000-F	Short pass 1000 nm
8	LL-950-F	Long pass 950 nm

Table 4.1: Filter wheels

Filters or pairs of filters used to make the bandpasses shown in Fig. 4.6. The stack number refers to the bandpasses indicated in the figure.

Reproduced from [17] with the kind permission of Donald E. Groom

was used. The short- and the longpass filters were combined to provide bandpasses (see table 4.1 and Fig. 4.6).

Gratings The turret of the monochromator can be equipped with up to four gratings. Two 1200 lines/mm gratings were installed - one with a 350 mm blaze and one with a 750 mm blaze - the desired wavelength range from 350 nm to 1100 nm can be covered with never less than 50% efficiency.

Slits Two motorized slits one at the entrance port and one at to output port of the monochromator allow to adjust bandwidth and light intensity. The maximum slitwidth for both slits is 2 mm giving bandwith of not more than 6.4 nm. A fixed 3.2 mm slit and an optical fiber are mounted on the lateral output port of the monochromator.

Integrating sphere

The light exiting the monochromator is not uniform. An empty sphere coated with a barium sulfate coating on the inside with reflectance of >99% over the wavelength

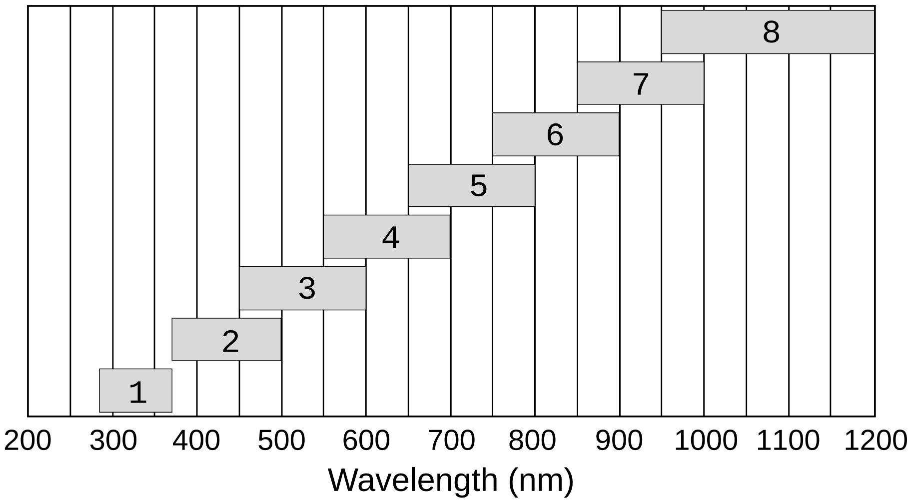

Figure 4.6: Approximate bandpasses of the filter stacks.
Reproduced from [17] with the kind permission of Donald E. Groom .

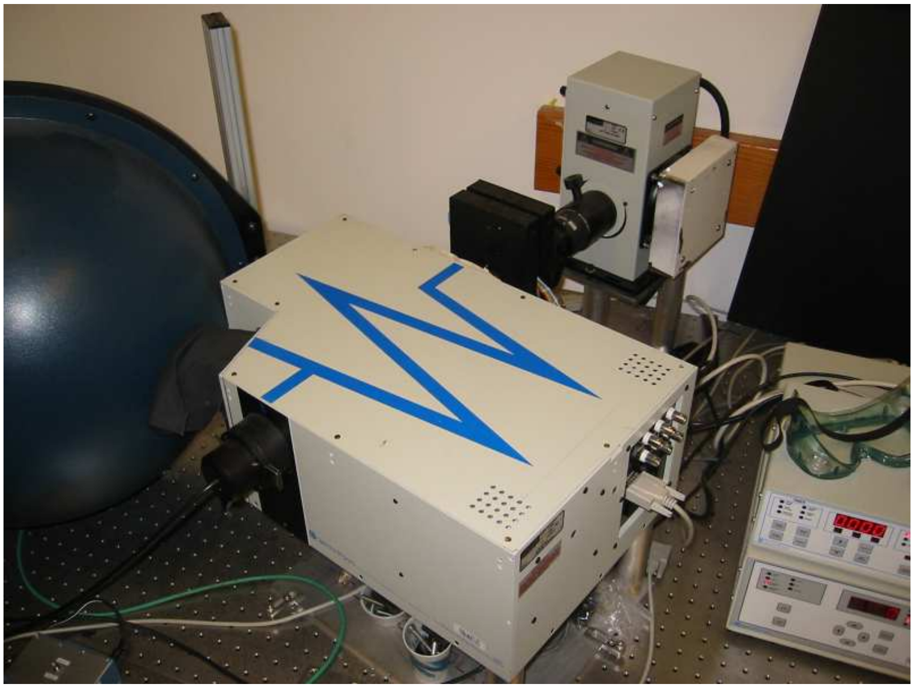

Figure 4.7: The M-257 monochromator. On the left the MC feeds into the integrating sphere. One can see the optical fiber mounted to the other output port.

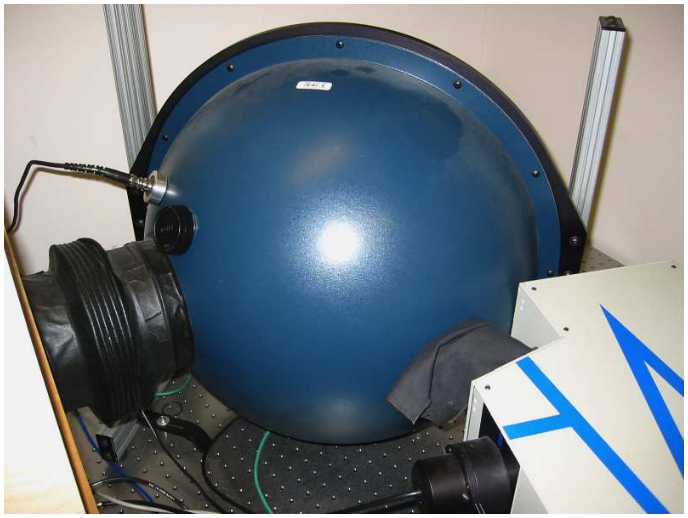

Figure 4.8: Shows the 20 inch integrating sphere. The 90°angle in the setup was employed for reasons of limited lab space.

range from 400 nm to 1100 nm is used to obtain a uniform light field.

The quality of the uniformity is dependant in the ratio of the surface of the sphere and the size of the holes. A very conservative 1% coverage was chosen resulting in a large 20 inch sphere. The overall distance between the 4 inch exit port of the sphere and the dewar window is 100 cm. The non-uniformity of the light field was shown to be smaller than 1% over the surface of the 100 mm diameter dewar window (see Sec. 4.3.9).

Dark box

The darkbox is a 80 cm long and 61 cm wide and 61 cm high wooden box painted black from the inside. It ensures a light tight space between integrating sphere and dewar window. The uniform light field is lambertian at the exit port of the sphere. Light of normal incident angle is desired for the CCD. The 100 cm spacing between the sphere and the dewar guarantees an angle of incidence of not more than 5.8°. Baffles in the dark box suppress stray light (see Fig. 4.9).

Further the dark box provides space for other experiments like the reflectometer setup which will be introduced in chapter 5 or point spread function measurements described in [13].

Shutter No. 2

For the actual exposure control a large 100 mm iris shutter is used. Light intensity instability which is caused by backreflection from the shutter blades made shutter #1

Figure 4.9: The inside of the 80 cm dark box.

unusable for exposure control. By mounting the shutter so far down the optical path one avoids that opening and closing the shutter affects the light source. It has the disadvantage of making a large shutter size necessary. We did not use a photometric shutter. Prior calibration of the shutter delay is therefore necessary (see 4.3.8).

Dewar system

The CCD is mounted inside a liquid-nitrogen cooled Infrared Labs ND-8 dewar. The operating temperature of the LBNL CCDs is -140 °C resulting from the SNAP requirements. Unique about this QE setup are two calibrated photodiodes which are mounted next to the CCD inside the vacuum.

The CCD and the photodiodes are separately temperature controlled. Usually the temperature control for one of the diodes is inactive. We are using two Lakeshore autotuning temperature controllers. The calibration temperature of the photodiodes is +25°C. The wish for the second diode arose from problems of contaminations in the dewar. The second diode is kept cold and its photocurrent may be compared to the other diode.

Masks were designed to limit stray light. A machine-shop-made rough mask covers most of the region inside the dewar. Holes are made so that just the active areas of the detectors are fully illuminated. Smaller wire-EDM high precision masks with 9 mm × 9 mm holes cover the edges of the 10 mm × 10 mm photodiode to eliminate edge effects (see 4.3.3).

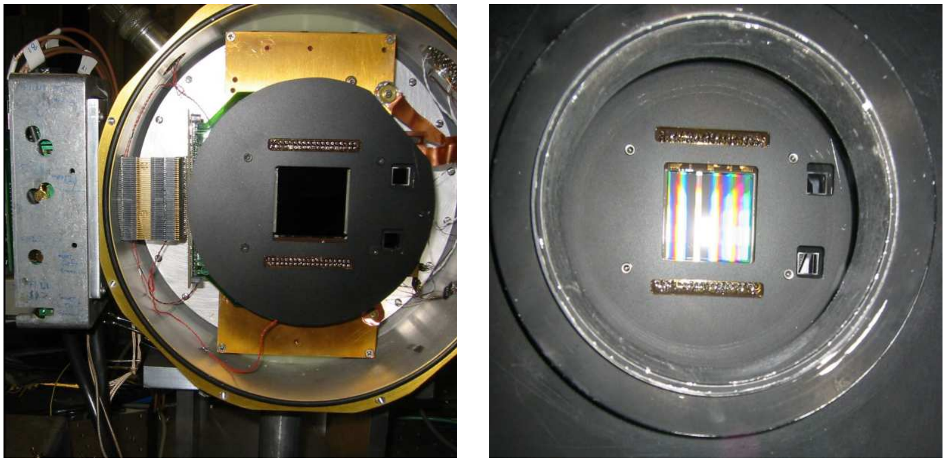

Figure 4.10: Shows the CCD and the calibrated photodiodes mounted behind baffles in the dewar. The left picture shows the open dewar. The right picture shows the view from inside the dark box facing the dewar. In this case a SNAP format but front side illuminated device was mounted. The gate structure causes the refractions seen on the CCD.

Readout electronics

CCD The CCD is read out using a Astronomical Research Cameras Gen II controller (see [31]) also known as *San Diego Controller* within the community (see [11]). Several modifications of the controller hardware allow to read out p-channel devices, applying high substrate voltages and ramping the substrate voltage up and down with predefined ramp rates.

Most CCDs tested in this work were SNAP V2 CCDs or CCDs of similar design. These CCDs have four readout amplifiers - one in each corner of the device - which are read out simultaneously.

The CCD signal goes through a stage of preamplification and inversion (we are dealing with p-channel devices, the controller was build for n-channel devices) on the outside of the dewar. After additional amplification the signal is sampled in double correlation mode (see [25]) and converted into a 16-bit data stream.

Photodiodes Two Keithley picoammeters measure the photocurrent. The photocurrent of the calibrated photodiode is read through a low noise triax cable. The second picoammeter is used to either crosscheck the photocurrent with the second calibrated diode or the light intensity in the sphere using and additional diode attached to the sphere. Monitoring the sphere current has the advantage of being able to adjust the light intensity without exposing the CCD to light. This method avoids saturation of the CCD.

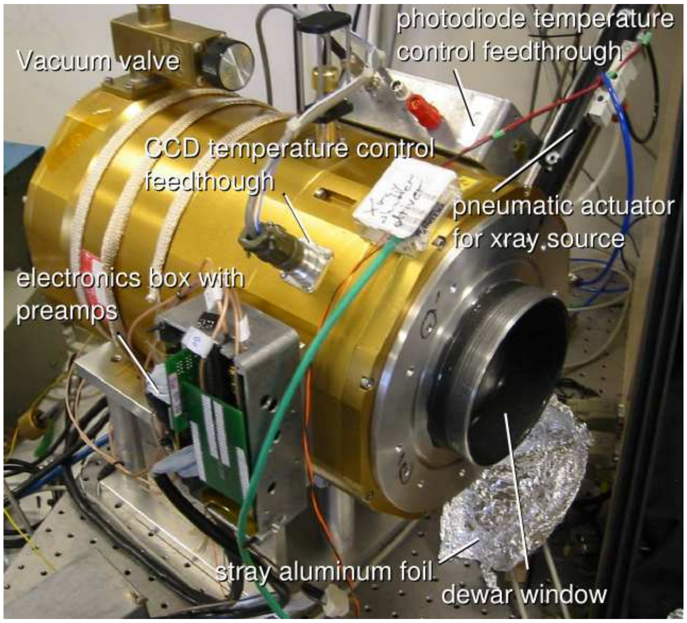

Figure 4.11: Infrared Labs ND-8 dewar. The dewar entrance port can be seen on the right. The feedthrough for the CCD signals is hidden behind the electronics box. A pneumatic actuator with mechanical feedthrough allows to move a x ray ^{55}Fe source in front of the CCD.

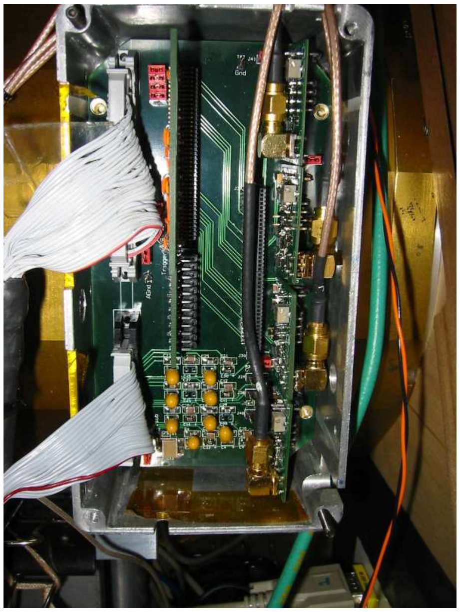

Figure 4.12: A closeup view of the electronics box which is attached to the dewar. The feedthrough for the CCD signals (the clocking signals, the bias voltages and the video signal) is hidden behind the printed circuit board. Four preamplifier daughter boards are located on the right.

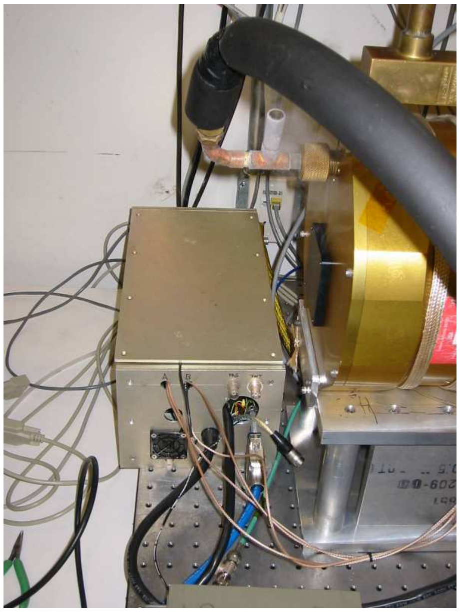

Figure 4.13: ARC GenII controller (San Diego) readout controller.

Figure 4.14: Two Keithley 6485 picoammeters measure the photocurrent of of either the two calibrated photodiodes or of one calibrated photodiode and the sphere diode. The later setup allows light level adjustment without exposing the CCD to light and therefore without saturating the CCD.

Software

The software for the San Diego Controller includes a JAVA interface called Voodoo. It allows full exposure control as well as modification of the controller and CCD parameters such as clocking voltages, substrate voltage, gain, video offsets etc.

We modified Voodoo in its version 1.7 extensively to include all the additional features we need for everyday CCD testing. We implemented a scripting capability based on the JAVA syntax. Interfaces for all devices in the QE setup such as the DEC, the monochromator, the picoammeters and the Lakeshore temperature controllers were implemented. The actual measurement is then controlled over a Voodoo script (see A).

4.1.2 Part list

Table 4.2: Parts list

Item	Part number	Description
Xenon Light Source		
Lamp	Oriel 6257	100W Xenon Lamp
Socket adapter	Oriel 66150	Lamp Socket adapter
Lamp housing	Oriel 68907	50-500-W arc housing w. f/1 condenser
Power supply	Oriel 68907	Power supply for arc lamps
Lens holder	Oriel 6195	Lens holder for 1.5 lenses
f/4.6 focusing lens	Oriel 41575	152 mm UVFS lens
Stabilization	Oriel 68950	Light intensity controller system
Shutter	Uniblitz VS25S2ZM0R1	25 mm aperture shutter
Monochromator and filter wheel		
Monochromator	Oriel 77700	MS257 monochromator
Multiple grating Turret	Oriel 77708	
Grating #1	Oriel 77742	1200/mm 350nm blaze
Grating #2	Oriel 77752	1200/mm 750nm blaze
Mirror	SP45700-1738	Mirror 50x50x6 mm coated one side
Slit controller board (2 ea)	Oriel 77712	Motorized single slit control
Output Mirror	Oriel 77737	
Motorized Filter Wheel (2 ea)	Oriel 77212	
Fixed slit	Oriel 77212	3.16 mm fixed slit
20 inch Integrating sphere	LabSphere CSTM US2000	coated with LabSphere Spectraflect
Light Measurement		
Photodiode	Hamamatsu S1337-1010BQ	Calibrated photodiode
Photodiode	Hamamatsu S2281	Sphere diode
Picoammeter (2 ea)	Keithley 6485	Picoammeters for PD readout
Optical Table	Newport IG-35-2	90x150 cm breadboard
	Newport IG-36-2	90x180 cm breadboard

Continued on Next Page. . .

Item	Part number	Description
Field shutter	Prontor (today Zeiss) 100 mm	Shutter at dark box entrance port. The shutter is not produced anymore. We had to implement a driver circuit.
Dewar	Infrared Labs ND-8 dewar	8” liquid nitrogen cooled dewar
CCD readout	ARC GenII controller	equipped with two ARC41 Video processor boards and LBNL inverse and high voltage modifications

Part list for the LBNL QE setup. The Linux PC, the masks and the dark box are excluded. The filters are listed in Table 4.1.

Reproduced from [17] with the kind permission of Donald E. Groom .

4.1.3 Measurement procedure

4.1.4 Overview

The QE measurement takes flat field images, i.e. images of the uniform lightfield, for each desired wavelength. Dark images of the same exposure time are acquired before each flat field image. The latter can be subtracted from the flat fields to zero out the baseline. The photocurrent of the calibrated photodiode is recorded during the flat field and the dark exposure. Later the CCD signal for each flat field is compared to the photocurrent.

4.1.5 Calibration

Monochromator

The monochromator was calibrated using 10 nm bandpass filters and the calibrated photodiode. The bandpassfilter was carefully placed in front of the photodiode and the monochromator was stepped through the wavelength region around the bandpass. The Xe emission lines can be used for calibration of the red part, the first strong line is located at 823 nm.

Shutter

We are not using a photometric shutter but an iris-type shutter. The time it needs to fully open after the shutter trigger was activated and the time it needs to fully close present errors to the exposure time. By taking a series of multiple exposures we are able to measure this error. The procedure is described in section 4.3.8.

4.1.6 Preparation

Setup

The CCD is mounted in the dewar. The dewar is evacuated and cooled. The CCD is kept at room temperature for as long as possible to allow as much water as possible to freeze out at the charcoal getter and the walls of the liquid nitrogen vessel.

It turned out that we actually get best results if we *thermocycle* the CCD once before starting the measurement (see 4.3.2). The CCD is allowed to cool down. It then is warmed up to room temperature and cooled down again before starting the measurement.

While the CCD is cooling first readout tests are executed. Often minor flaws have to be eliminated. Due to the buildup of contaminations it is important to start the measurement as quickly as possible once the CCD is cold.

Gain calibration

Before the actual measurement the gain has to be calibrated. We observed the gain to be different every time we cool a device down. Changes of the gain were observed to exceed 5%. Therefore the CCD is exposed to x-rays resulting from the ^{55}Fe decay. The resulting image is used to calibrate the system gain (see Sec. 2.1).

4.1.7 The QE scan

Wavelength selection The operator chooses a wavelength rage and a stepwidth he wants to measure the QE for. Now for all selected wavelengths the monochromator is first set to the specific wavelength. Using predefined changeover tables the monochromator automatically chooses the right filter and the right grating for each wavelength. We monitor the automatic filter changes of the monochromator. After such a filter change we wait for two minutes to allow the light intensity to stabilize. As explained above, the reflectivity of the different filter varies. After a filter change variations in the light intensity - possibly due to changes in the lamp temperature - were observed.

Light level adjustment The calibrated photodiode inside the dewar was used to crosscalibrated the photodiode in the integrating sphere during earlier measurements. So the sphere diode can then be used in the next step to set the light level.

A light level of 2000 e^-/pixel/s (see 4.3.1) is usually employed. The lightlevel is adjusted by changing both slits of the monochromator. An automatic procedure first sets the slits to their minimum and maximum widths to see whether the desired lightlevel is achievable and then adjust the slits until the the lightlevel is reached. The shutter at the exit port of the sphere is left closed throughout this procedure. The CCD is therefore not saturated. Once a CCD is saturated it has to go through a series of procedures such as the erase, the epurge and the clear procedure (see appendix D) which restore its working condition. It is therefore favorable avoid saturation. An alternative scheme takes the slitwidths which were determined during earlier measurement and sets them directly. This decreases the time for a QE scan significantly.

Flat fields The CCD is cleared (see appendix D) then a darkimage is taken. The CCD is exposed to darkness using the same exposure time as will be used later for the actual flat field. As a compromise between high light intensity and resulting high signal to noise ratios but short exposure times and larger errors in the exposure time on the one hand or long exposure times and low light intensities on the other (see 4.3.1) we chose an exposure time of 20 s.
During the dark and the flatfield exposure the photocurrents of the calibrated diode and the sphere diode are recorded. The current is sampled with a half second integration time. The Keithleys show the best noise performance for a one second integration time. But there is a delay between the samples which is in the order of the integration time cause by the Keithleys picoammeter. To loose less time at the beginning and the end of the exposure we integrate for half a second. Due to the mentioned delay we get eight current samples for each exposure.

Double sweep interlaced scan Setting the wavelength, adjusting the light level and taking dark images and flat fields is repeated for each wavelength. The scan is performed in a *double sweep interlaced* manner. Lets say the operator chooses to scan from 300 nm – 1100 nm in 10 nm steps. The measurement script then automatically scans first 300 nm, 320 nm, 340 nm and so on up to 1100 nm, then it scans 310 nm, 330 nm, 350 nm and so on up to 1090 nm. This double sweep first showed us drifts in the measurement which were caused by the buildup of contaminations. It turned out to be a very useful tool to monitor for contaminations.

The actual script for the measurement is described in appendix A.

4.2 Photodiode mode

4.2.1 Setup

CCD as photodiode On the CCD the reset MOSFET is connected to the serial register (see Fig. 4.15), the photocurrent is measured between reset drain and

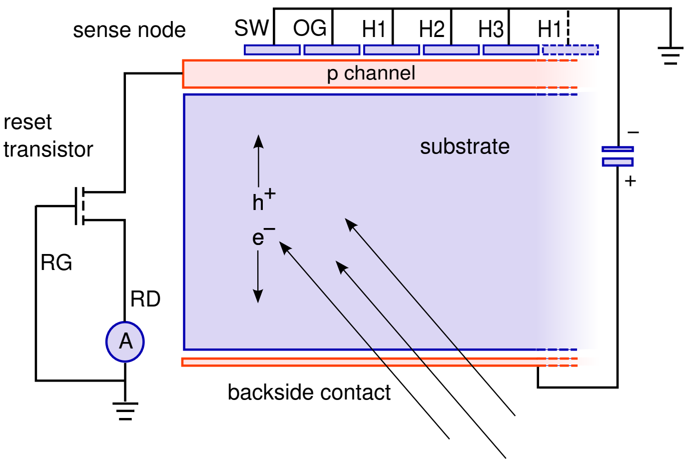

Figure 4.15: Shows a simplified image of the CCD wired for a photodiode mode measurement.
The on chip reset transistor drain allows to measure the current flow out of the signal channels. Here only the end of the serial register channel at the sense node is shown. But the serial register is connected to all signal channels in the photoactive area of the CCD. For thick SNAP type CCD a substrate voltage is applied to fully deplete the substrate.

ground. The reset gate is connected to the reset drain to avoid gate charging of the transistor and a resulting loss in conductivity.

We decided to ground all the clocking lines. We also grounded the guard rings around the active area to eliminate edge effects. To fully deplete the thick CCD a substrate voltage has to be applied vs. ground. The electronics box at the side of the dewar was removed and replaced by a connector which allowed to connect a power supply for the substrate voltage and a current meter.

Substrate voltage [13] showed that we can expect full depletion of a 200 μm around 20V. We typically applied a substrate voltage of 30 V. Measurements at a number of different substrate voltages above 20 V did not show any dependence of the QE of the applied voltage.

Photocurrent The Keithley picoammeter which was used to monitor the sphere diode in the CCD mode measurement is now used to measure the CCD photocurrent.

Temperature The CCD may or may not be cooled during the photodiode mode measurement. During a warm measurement it proved to be important to stabilize the temperature of the CCD very carefully due to the strong dependence of the dark current on the temperature. Drifts in the temperature would result in drifts in the dark current which would make a clean substraction of the dark current impossible.

Figure 4.16: Adapter to operate the CCD in the photodiode mode.

Masks We already equipped the originally 10 mm × 10 mm sized calibrated photodiode with a mask to avoid edge effects of the photodiode. We manufactured a second mask - with 31.98 mm × 31.98 mm slightly smaller than the active area of the CCD - and placed it in front of the CCD for the same reason.

4.2.2 Measurement procedure

Wavelength selection The operator chooses the wavelength range and the stepwidth and the script scans through all selected wavelengths in the double sweep interlaced manner explained in section 4.1.7. A two minute delay after filter changes allows the light stability to recover.

Light intensity Since now we use the second Keithley to measure the photocurrent of the CCD, we can not use the sphere diode for light adjustment any more without purchasing more picoammeters. In the photodiode mode saturation of the CCD is no issue though since the CCD is constantly drained. After opening the large shutter we can therefore use the calibrated photodiode for the light level adjustment. The light level is adjusted in the manner as in the CCD mode measurement. Again we typically chose a light level of 2000 photons/pixel/second

Photocurrent Before the actual photocurrent is measured, the shutter is closed and the dark current of both, the CCD and the photodiode, is recorded. We introduced very conservative 30 s delay into our measurement to allow the current to

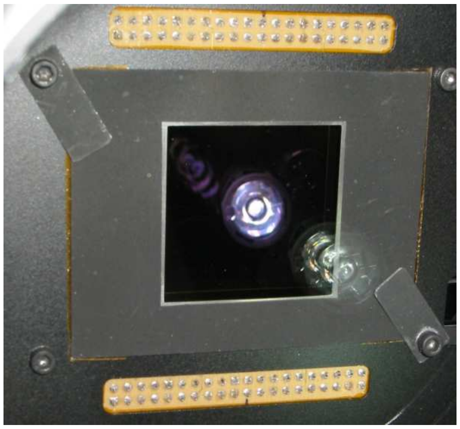

Figure 4.17: Shows the mask we place in front of the CCD for photodiode mode measurements to avoid edge effects (compare to Fig. 4.10).

stabilize before triggering the currentmeters. We take 20 samples with a half second integration time for the current measurement.

Next, the large shutter is opened and after another delay of 30 s the actual photocurrent is measured.

Finally the dark current is measured for a second time. Later the average of the dark current before and after th measurement is calculated. This allows to compensated for - at least - linear drifts in the temperature over the time of the measurement.

4.3 Error sources

4.3.1 The right light level

The higher the light level, the better the signal to noise ratio of the photocurrent. On the other hand a higher light level also results in shorter exposure times. Since we do not use a photometric shutter, we prefer long exposure times to minimize errors in the exposure time caused by the opening and the closure of the shutter.

The maximum signal the 16-bit analog to digital converter of the readout electronics can measure is $2^{16} = 65536$ ADU. A system gain of 1-1.5 ADU/e^- per electron is typical. We expose the CCD to light for 20 seconds. We chose 2000 photons/pixel/second as reasonable light level. For a gain of 1.5 ADU/e^- this would result in 60.000 ADU per pixel if the CCD had a 100% QE. With exception of a wavelength of 300 nm this light level proved to be achievable over the whole wavelength range for a SNAP device with 10.5 μm pixel.

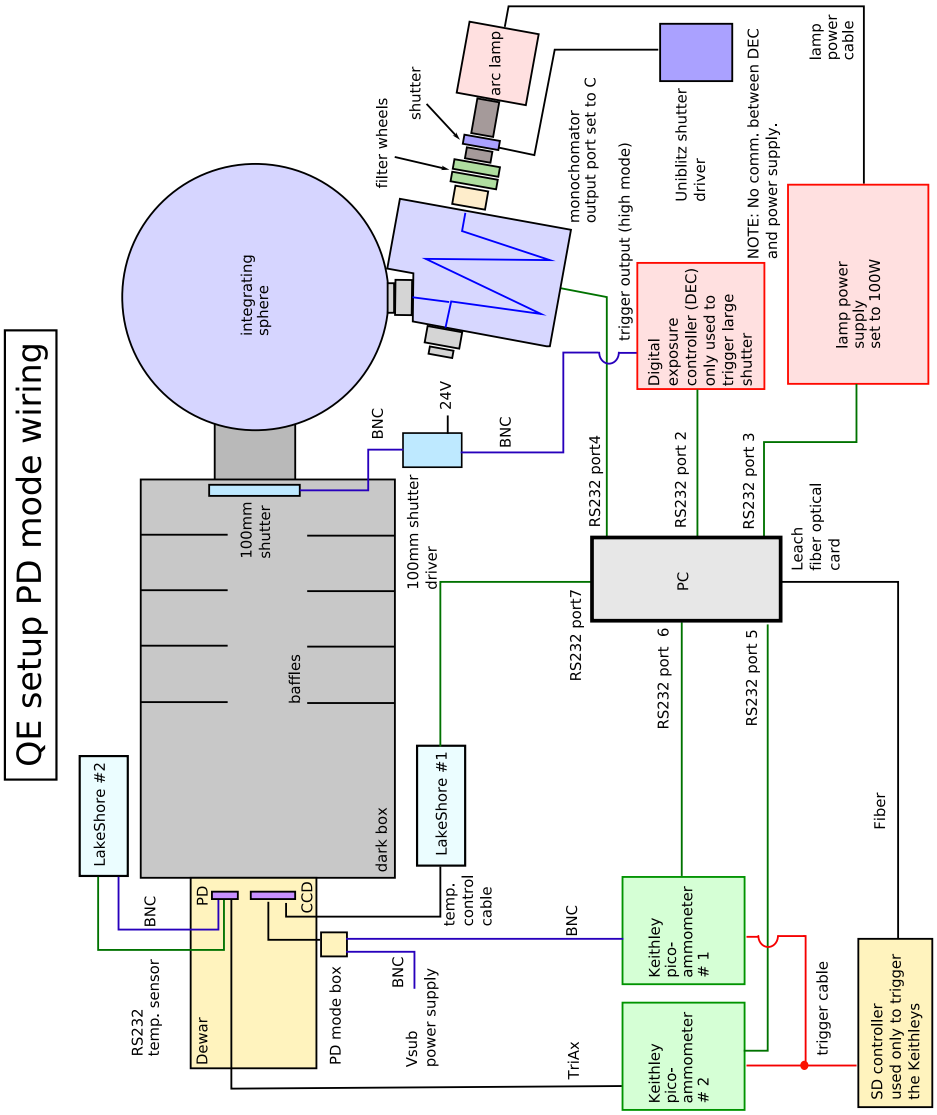

Figure 4.18: Overview of the quantum efficiency setup for the photodiode mode measurement.

We take 20 current samples for each exposure. Usually the first one or two samples and the last ten samples - due to the mentioned delay the lie outside of the exposure time interval - have to be dropped.

4.3.2 Contamination of the Dewar

Contaminations of CCDs in the dewar turned out to be the most serious obstacle to QE measurements. First measurements of the quatum efficiency showed drifts. Each measurement gave a significantly different curve (see Fig. 8.16). We were able to track the problem down to films growing on the surface of the CCDs. Differend kinds of films of unknown composition were observed. Some of them evaporated at room temperature, others were permanent and had to be washed off.

The first encounter of a film on the CCD was rather surprising. After an extended search for the reason for the varying QE results we used the flashlight to examine the CCD itself. We found a diffuse reflection of the light off the surface of the CCD (see 4.19). We warmed the CCD up to room temperature. Since the layer stayed on the CCD we took it to the clean room and washed it with soap and water.

Now, that we examined the CCD with a flashlight on a regular basis we found two different kinds of contaminations. One appears relatively suddenly, does not disappear at room temperature and has to be washed off.. The other one starts to appear slowly when the CCD is cold. First visible signs a changes in the color of the reflection of the flashlight off the CCD's surface (see 4.19). When the CCD is warmed up, the film starts to become even more pronounced and the reflection becomes more and more diffuse until the temperature reaches about +10°C where the film evaporates completely.

As long as the CCD stayed warm (i.e. room temperature) it never showed any contamination. As soon as it is cooled down it becomes a very effective getter. The dewar is equipped with a charcoal getter which is held at the temperature of the liquid nitrogen and is intended to collect all residuals - especially water - in the vacuum on its large surface. Still at -140°C the CCD collects substances out of the non-perfect vacuum.

One source of contamination seemed to be one of the heaters of the calibrated photodiodes. The heater of diode #1 was observed to unsolder itself from its wires. Measurements of its temperature in ambient air showed that the pins actually became as hot as 160°C. In vacuum the situation might actually be worse due to the lack of the cooling by air convection. We believe that the evaporation of solder flux caused one type of contamination. After replacing the heater this contamination did not appear again.

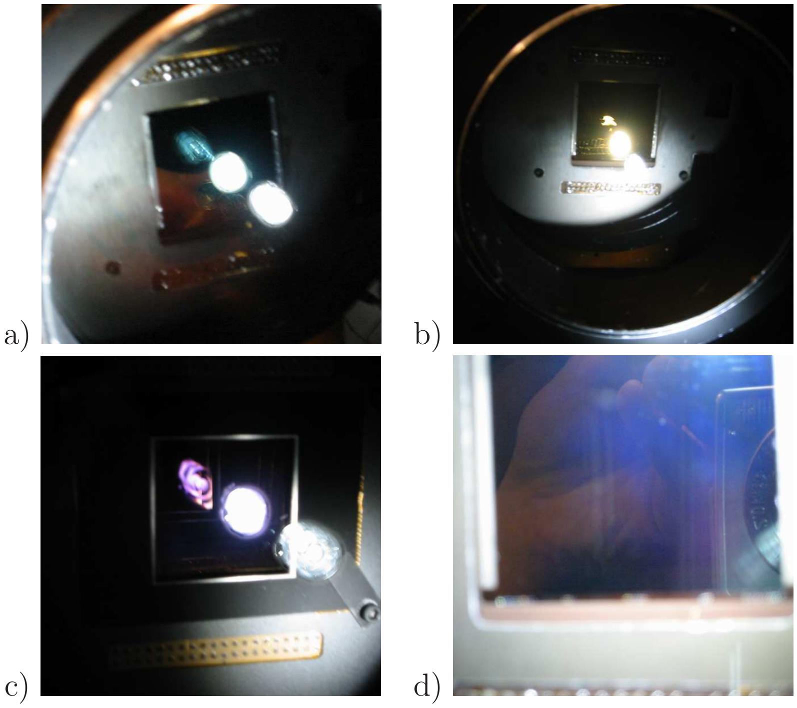

Figure 4.19: Shows the change in the color of the reflection of a CCD due to contamination.

a) The normal blue color of the reflection after the CCD was warmed up to +30° C.

b) The CCD was held cold in the vacuum for one night. The left picture shows the yellowish reflection of the flashlight of the surface of the CCD.

c) Several hours later the the reflection had turned into a purple color.

d) The worst case is usually seen when we warm the CCD up. The reflection now turned into a diffuse type.

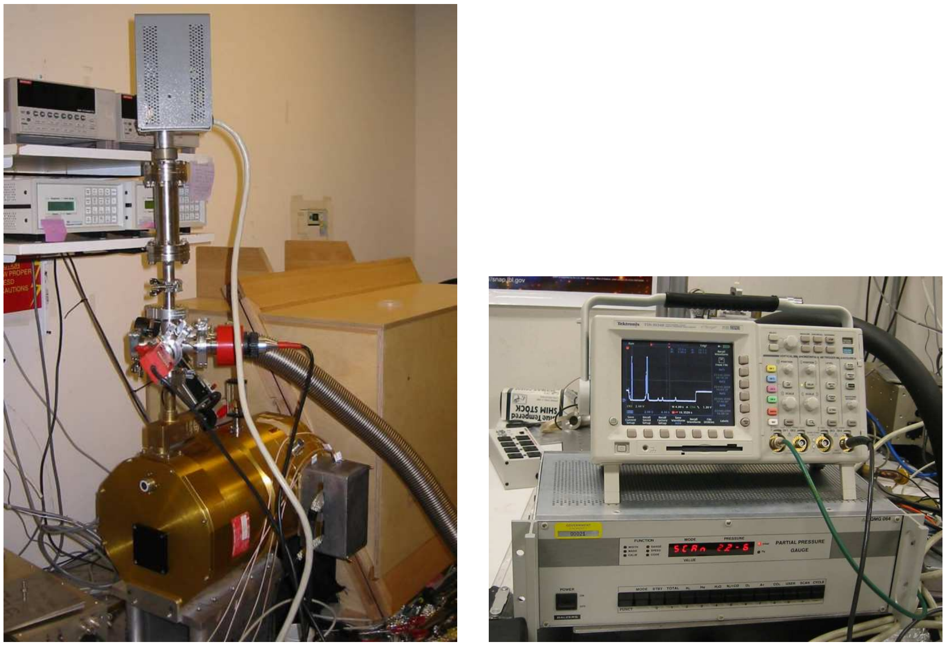

Figure 4.20: A RGA attached to the dewar allowed to analyze residual gases. After the analysis we believe that water is the most likely culprit for the remaining contaminations.

The second kind of contamination (starts appearing slowly, evaporates at room temperature) turned out to be the most difficult to deal with.

We tried cleaning the dewar extensively by partly cleaning parts in a ultrasonic bath and wiping them with alcohol, partly by just wiping them with alcohol. Other groups reported contaminations caused by the getter. Test runs with a freshly baked and without getter with did not succeed.

We attached a residual gas analyzer (RGA) to the dewar. The only obviously problematic peak in the mass spectrum was water. Due to the electronics inside the dewar a baking of the dewar is difficult. Heating of the dewar for several hours up to 60°C did decrease the water peak but did not make it disappear. We cooled the dewar and still found a buildup of a contamination on the CCDs.

Finally we tried to freeze the water out. We kept the dewar cold for about three days while keeping the CCD warm. Still the CCD developed a contamination during the QE scan (see Fig. 4.21).

None of these measures produced stable QE results. We concluded that the attempt to perform the perfect QE measurement which avoids any kind of contamination is probably not practical since possibly each week a different CCD will be

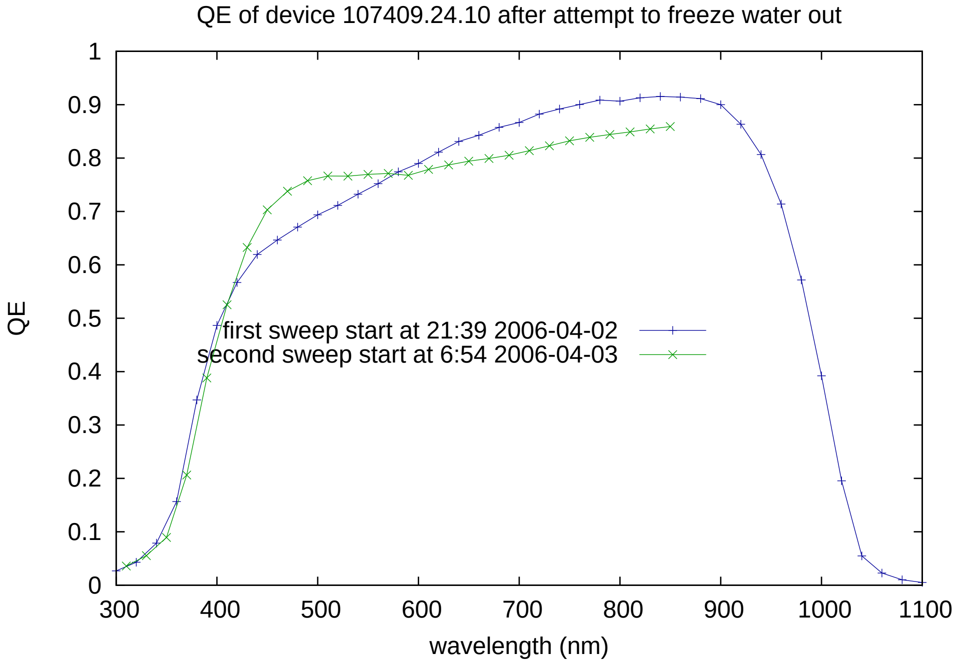

Figure 4.21: Shows the two sweeps of the QE of device 107409-24-10 scan after out attempt to freeze the residual water in the dewar out. The idea was to give the charcoal getter time to collect the remaining water molecules out of the vacuum before cooling the CCD. We kept the dewar cold (filled with liquid nitrogen) for two and a half days while the CCD was kept at room temperature. Still the scan shows the characteristic drift of a contamination. The second sweep shows an increased QE in the blue and a decreased QE in the red. We interrupted the second sweep since the contamination was obvious at that point.

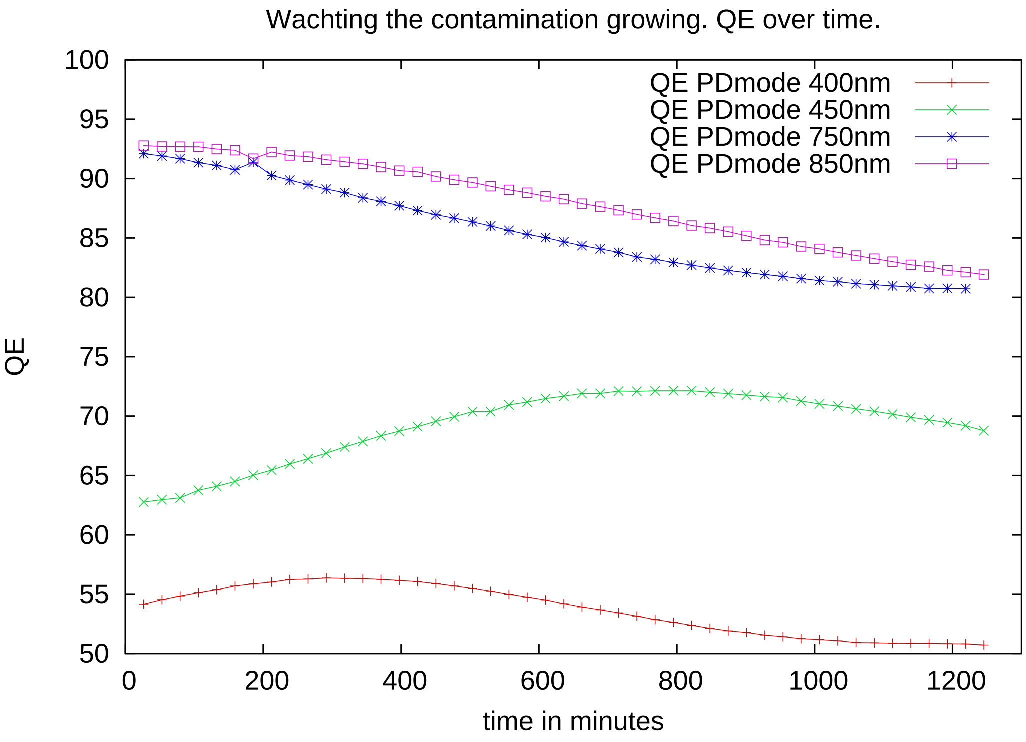

Figure 4.22: The quantum efficiency measured 47 times at four different wavelengths over a time period of 20 hours and 46 minutes. One can see the change over time due to the build up of a contamination layer on the CCD.

installed and tested in the QE setup. Each time the dewar is opened at least water is brought into the system.

We tried to observe the time constant for the buildup of films. We cooled the CCD down and measured the QE repeatedly for four wavelengths at which the variations showed the most significant change during earlier measurements (compare with figure 4.21). We kept repeating this measurement for about 21 hours. The result is shown in figure 4.22. First of all one can see the change in quantum efficiency over time. As observed with a flashlight already, the change is different for different wavelengths. On can also see that for shorter wavelengths earlier and for longer wavelength later a turnover point is reached. The change in the QE is not – or not only – caused by absorption in the contamination. Rather it acts as additional antireflective layer. The reflectivity is lowest when the layer's thickness reached

$$d = c \cdot \frac{\lambda}{n \cdot 4} \tag{4.1}$$

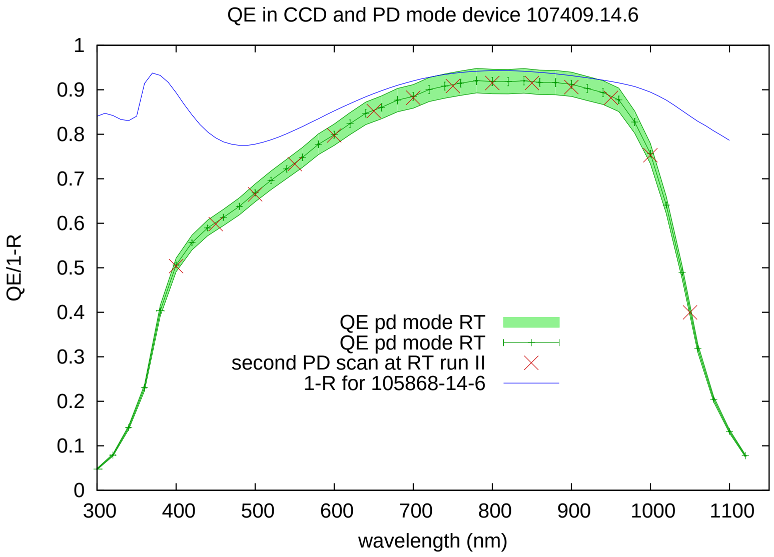

Figure 4.23: A repeated photodiode mode room temperature QE measurement once before and once after the CCD was cooled down allowes to prove the the contaminations which grow on the cold device disappear completely when it is warmed.

where n is the refactive index of the contamination, λ is the vacuum wavelength of light and c equals one or two depending on whether n is larger or smaller than the refractive index of SiO_2.

From this result we learned that a possible workaround might be to measure the quantum efficiency quickly enough, i.e. before the contamination had time to build up. We increased the stepwidth for the QE scan, minimized delays such as light stabilization delays after filter changes (see 4.1.7) and use predetermined values for the slitwidths for each wavelength (see 4.1.7). For a stepwidth of 25 nm we can now measure the QE from 300 nm to 1100 nm in 222 minutes and the first sweep is completed in 109 minutes. From 4.22 we see a 3.5% worst case effect for a 222 minute scan for the first sweep the error due to contamination should be less than 1.5% .

Of course we do not know that the time constant for the buildup of the contamination is the same for each measurement. But by performing the QE scan in the double sweep interlaces manner (see 4.1.7) we can monitor the drift of the QE by comparing neighboring points.

Finally the photodiode mode scan at room temperature allowed us to show that the contamination really disappears completely when warming the CCD up by comparing results before and after the cooling (see Fig. 4.23).

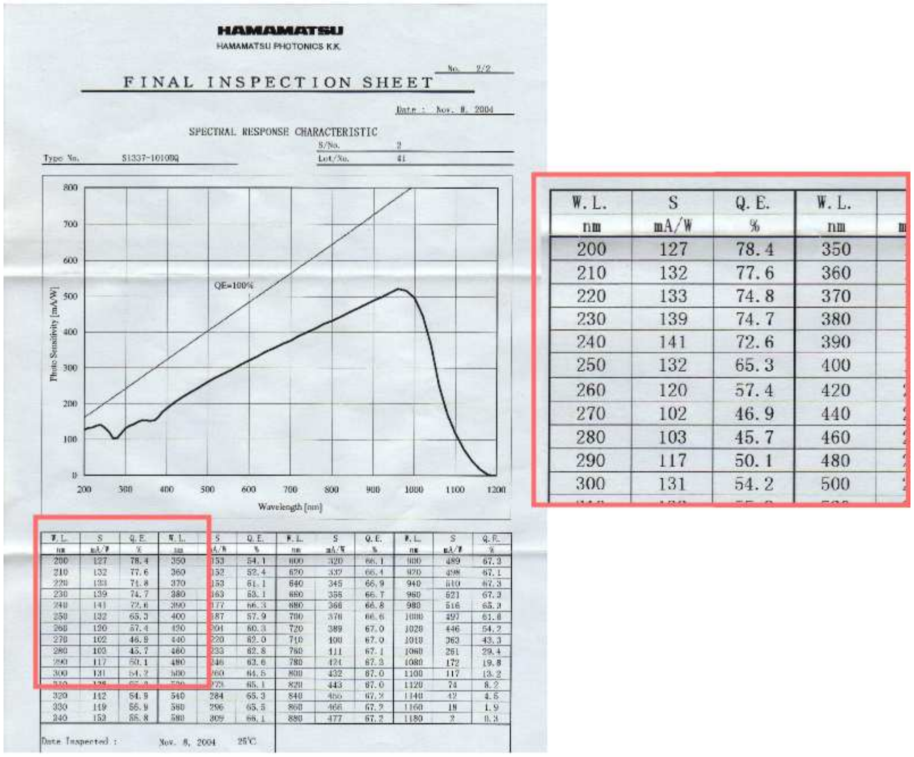

HAMAMATSU
HAMAMATSU PHOTONICS K.K.

No. 2/2

FINAL INSPECTION SHEET

Date : Nov. 8, 2004

SPECTRAL RESPONSE CHARACTERISTIC

Type No. S1337-1010BQ
S/No. 2
Lot/No. 41

W.L. nm	S mA/W	Q.E. %	W.L. nm	S mA/W	Q.E. %	W.L. nm	S mA/W	Q.E. %	W.L. nm	S mA/W	Q.E. %
200	127	78.4	350	153	54.1	600	320	66.1	900	489	67.3
210	132	77.6	360	152	52.4	620	332	66.4	920	498	67.1
220	133	74.8	370	153	51.1	640	345	66.9	940	510	67.3
230	139	74.7	380	163	53.1	660	355	66.7	960	521	67.3
240	141	72.6	390	177	56.3	680	366	66.8	980	516	65.3
250	132	65.3	400	187	57.9	700	376	66.6	1000	497	61.6
260	120	57.4	420	204	60.3	720	389	67.0	1020	446	54.2
270	102	46.9	440	220	62.0	740	400	67.0	1040	363	43.3
280	103	45.7	460	233	62.8	760	411	67.1	1060	251	29.4
290	117	50.1	480	246	63.6	780	424	67.3	1080	172	19.8
300	131	54.2	500	260	64.5	800	432	67.0	1100	117	13.2
310	[illegible]	[illegible]	520	273	65.1	820	443	67.0	1120	74	8.2
320	142	54.9	540	284	65.3	840	455	67.2	1140	42	4.5
330	149	55.9	560	296	65.5	860	466	67.2	1160	18	1.9
340	153	55.8	580	309	66.1	880	477	67.2	1180	2	0.2

Date Inspected : Nov. 8, 2004 25°C

Figure 4.24: The calibrated photodiode is delivered with this *Final Inspection Sheet*. The document shows a curve for the quantum efficiency of the photodiode. It also provides a table with actual figures. The manufacturer does not give any error estimates on the calibration.

4.3.3 Calibrated Photodiode

We use the calibrated photodiode S1337-1010BQ from Hamamtsu. The manufacturer delivers the photodiode with a so called *Final Inspection Sheet* (see Fig. 4.24). As already explained in 2.5.2 the calibration of the the reference photodiode is crucial to the measurement.

Calibration The first concern is the original calibration itself. The *Final Inspection Sheet* provides the calibration in form a a curve and a table of numbers. It does not give any error estimates on the calibration though. Our best guess is that the calibration is correct within the last digit given on the sheet. We assume a one percent error on the given numbers.

Contamination The calibration is obviously very sensitive to any kind of contamination of the surface of the photodiode. Contaminations might be caused by

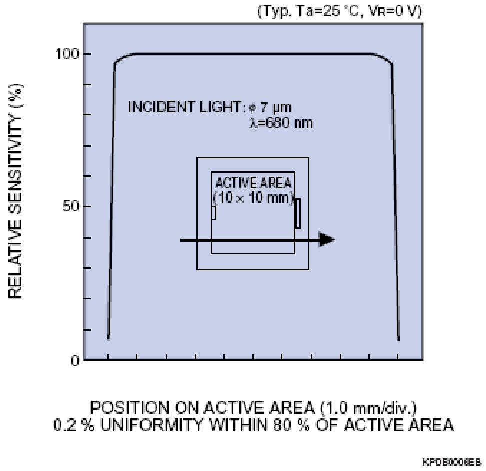

Figure 4.25: Shows the spatial variation of the sensitivity of the similar Hamamatsu S1227-1010BQ photodiode. Masks which cover the edges of the photoactive area eliminate edge effects. (from the Hamamatsu website)

the handling of the device or by gettering in a non-perfect vacuum. We try keeping the photodiode at room temperature and to clean it on a regular basis. In addition to QE loss due to contaminations, other groups reported aging effects of their detectors. Now, a loss in the QE of the photodiode would result in a too high QE estimate for the CCD (see 2.5.2). By measuring the reflectivity for each CCD we set an upper limit the the CCD's QE which would point to a change of the QE of the photodiode if exceeded.

Active Area The photodiode is calibrated using a pointlike light source whereas we illuminate the device with a uniform lightfield. Manufacturer provided plots of the uniformity of similar device's response show variations at the edges (see Fig. 4.25). We placed a 9 × 9 mm mask in front of the 10 × 10 mm diode to eliminate these effects (see Sec. 4.1.1). Still the error in the size of the mask presents an error to the active area of the detector in the QE calculation. After consultation of the machine shop we estimate an error of a half thousands of an inch or 12.7 μm accuracy for the edge of the mask. Further we estimate an $(2 \times 10^{-3}\ \text{inch})^2 = (50.8\mu\text{m})^2$ error for the corners of the mask. This results in a 0.3% error for the active area of the photodiode.

Alignment The photodiode has to be aligned coplanar to the CCD. The active area and the mask must be perpendicular the the optical path. We checked the alignment with a laser pointer. The reflected point was off by less than 5 cm from the beam path at a distance of 80 cm. A tilt of this magnitude would result in a 0.2% error of the active area of the photodiode.

4.3.4 Signal integration

The signal of one CCD pixel is subject to several sources of noise and variations.

Fixed pattern noise First of all the quantum efficiency is not identical for all pixel of the CCD. Contaminations obviously affect their ability to detect photons but also their size is not necessarily equal. Imperfections in the mask alignment during the production of the detector cause variations to the actual size of a pixel. The thickness of the antireflective coatings may also vary and lattice defects can trap generated electron holes. These variations of the QE from pixel to pixel are of systematic nature and are often referred to as fixed pattern noise. Pattern noise is proportional to the average pixel signal.

Shot noise Depending on the average signal the shot noise (see also Sec. 6.2) might actually hide the fixed pattern noise. The standard deviation of the number of photons falling into the area one pixel is proportional to the square root average number of photons per pixel. As long as the light intensity is small the shot noise therefore dominates.

Read noise The statistical read noise was discussed in section 2.3. It affects the pixel signal and can be measured separately. Read noise can be as small as four electrons RMS. Up 20 electrons read noise were measured for some CCDs. The read noise presents a constant noise floor for the pixel signal.

To calculate the average pixel signal the operator chooses a region in the flat field images. Since we want to measure the average quantum efficiency we assign an error of $\frac{\sigma_S}{\sqrt{N}}$ to the average signal where σ_S is the standard deviation and N is the number of pixels in the chosen region of interest. We typically measure standard deviations in the order of a few percent. The regions of interest we chose usually integrate over 500^2 or more pixel. The error to the average signal is therefore in the order of a hundredth of a percent and negligible.

4.3.5 Monochromator

Bandwidth During the scan over the different wavelengths we try to keep the lightlevel constant (see 4.3.1) by varying the widths of the monochromator input and output slits. For the chosen gratings the bandwidth is given by

$$\Delta\lambda = 3.2\frac{\text{nm}}{\text{mm}} \cdot w$$

Where w is the slitwidth given in mm. Since the maximum slitwidth is 2000 μm , the bandwidth might be as large as 6.4 nm. Now, the actual quantum efficiency is a convolution of the actual quantum efficiency with the monochromator bandwith. In the case of strong variations as at the cutoffs this will lead to errors. We will

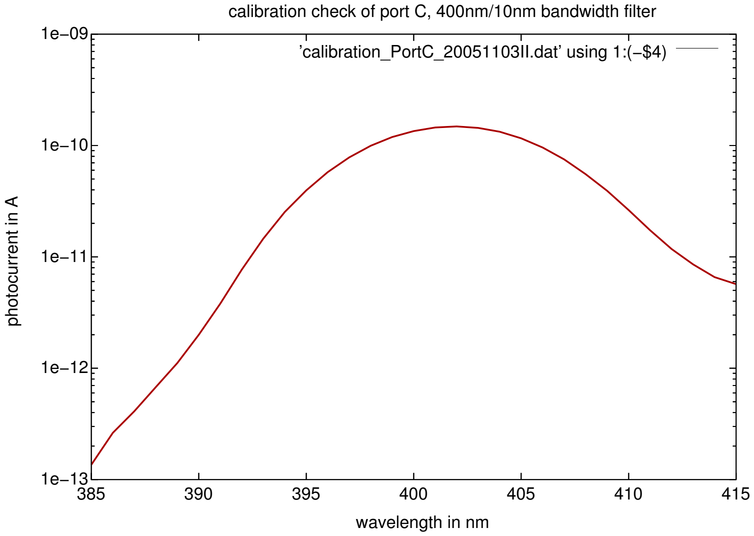

Figure 4.26: Shows a scan from 385 nm to 415 nm for a 10 nm wide 400 nm bandpassfilter. After this measurements the monochromator was recalibrated.

not try to correct for the bandwidth but rather give the bandwidth as error in the wavelength.

Calibration As explained in 4.1.5 the monochromator was calibrated using 10 nm bandpass filters and a photodiode. Figure 4.26 shows a typical wavelength calibration. The peak maximum is located between 400 nm and 405 nm. We claim a ±2.5 nm calibration error.

4.3.6 Backreflection

In this setup the dewar window is supposed to be coplanar to the CCD's and the photodiode's surfaces. Incident light can reflect off the detectors surfaces, an be reflected back off the window onto the detectors (see Fig. 4.27).

If one assumes a 60% reflectivity of the photodiodes and a 3.5% reflectivity both surfaces of the window, this leads to about one percent more light on the photodiodes than anticipated. The antireflective coating of the CCD will cause less light to be reflected resulting in a difference of the lightlevels at the photodiodes and the CCD. Now, actually the surface of the photodidodes is not perfectly flat, and its alignment to the dewar window is not actually coplanar either. Thus the error is difficult to estimate but probably smaller than one percent.

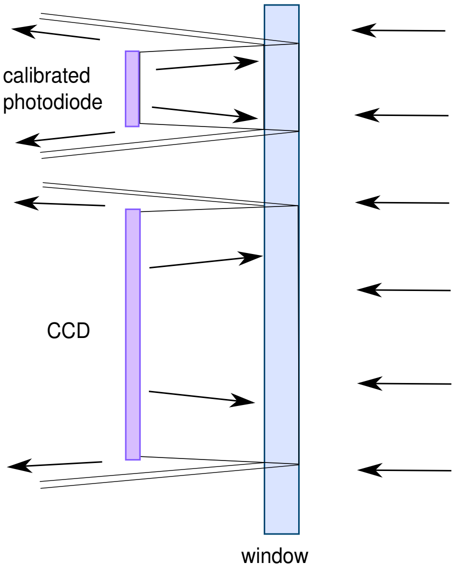

Figure 4.27: Incident light is reflected off the photodetectors on the dewar window and reflected back onto the detectors.

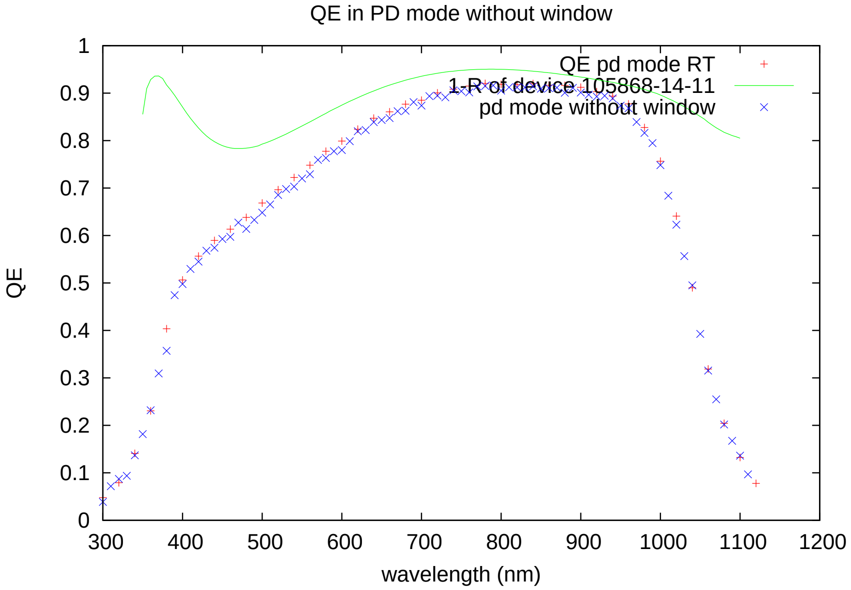

Figure 4.28: Compares the QE in PD mode at room temperature with and without dewar window. One minus reflectivity is plotted as reference.

The photodiode mode allows to measure the quantum efficiency at room temperature. Thus we were able to take a QE scan without the dewar window (see 4.28). The temperature stabilization in air is more difficult than in vacuum. Due to the strong temperature dependence of the dark current the windows-less measurement shows more noise than the measurement with window and vacuum. Still both curves show a relative good agreement. The QE without the windows seems to be slightly smaller, indicating that actually more light is backreflected onto the CCD than onto the photodiodes. From this result we estimate a probably conservative one percent error caused by backreflection. Such an effect might be decreased by using a window with anitreflective coatings. Since we found that a regular cleaning of the window is necessary we believe that this would be not a practical solution. Tilting the dewar window would eliminate backreflection and might be the right approach.

4.3.7 Straylight

The filters at the entrance port of the monochromator suppress second order refractions by a factor of 10^{-3}. The monochromator stray light rejection lies in the order of 10^{-4} . How much stray light affects the error in the quantum efficiency depends on the QE for the light within the bandwidth and the QE for light outside of the bandwith. [46] quotes a worst case error of about 0.8% for 500 nm and 1000 nm.

4.3.8 Shutter delay

As explained in 4.1.1 we decided against using the small shutter between the lightsource and the monochromator for exposure control. Its reflectivity caused light instability when the shutter was opened. We attached a large shutter to the exit port of the integrating sphere. This 100 mm shutter is also of the iris type and therefore necessarily not a photometric shutter. The time it needs to open and close present systematic errors to the exposure time. Due the size of the shutter the open- and closure times lie in the oder of a tenth of a second.

The error Δ_T to the exposure time T is measured by multiple exposures. For exposure times which are significantly longer than Δ_T, we can safely assume that Δ_T is not a function of T. By exposing a CCD one time to T_N and n times to T_N/n - where T_N is the nominal exposure time - one can calculate Δ_T from the resulting CCD signal.

Since our trigger mechanism could not handle non-integer exposure times, we exposed a CCD to nominal 1 × 16 s, 2 × 8 s, 4 × 4 s, 8 × 2 s and 16 × 1 s. The each exposure we took a dark image with the same exposure time by closing shutter #1. The test was conducted with the SNAP V2 backside illuminated device 107409.24.10. A subregion – free of cosmetic defects – of 400 × 1000 pixel was chosen to calculate the CCD signal.

Nom. exposure time (s)	**S** (ADU)
1 × 16	13974 ± 183
2 × 8	14150 ± 185
4 × 4	14167 ± 185
8 × 2	14254 ± 187
16 × 1	14619 ± 190

Table 4.3: Shutter delay
Resulting CCD signals S for multiple exposures. S is the remaining average signal per pixel after dark substraction.

From these data we calculate:

$$\Delta_T = 0.044 \pm 0.018s$$

In addition to the systematic uncertainty of 18 ms we estimate a rather conservative 20 ms jitter of the exposure time.

4.3.9 Lightfield non-uniformity

The light field nonuniformity was measured by [46] (see Fig. 4.29) . A photodiode was mounted on a micrometer stage and the light intensity was scanned in the horizontal and vertical direction.

The CCD is mounted in the center of the dewar window (centered around zero in Fig. 4.29). The SNAP device measures about 7.5 cm along the diagonal axis. From

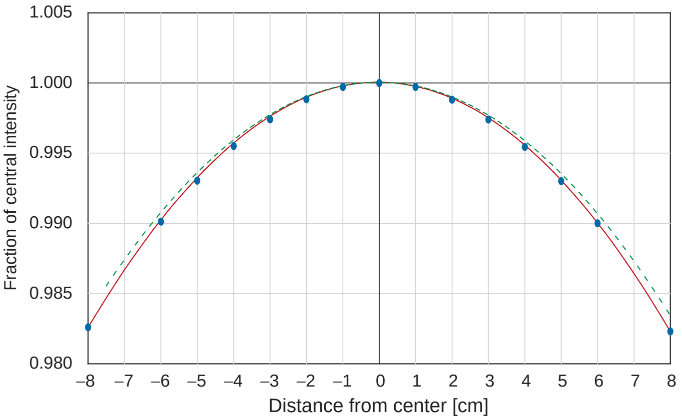

Figure 4.29: Position dependence of light intensity in front of the dewar, as obtained by scanning with a photodiode. Measurements are shown by the circles. The dashed curve is from a less-dependable vertical scan.
Reproduced from [17] with the kind permission of Donald E. Groom

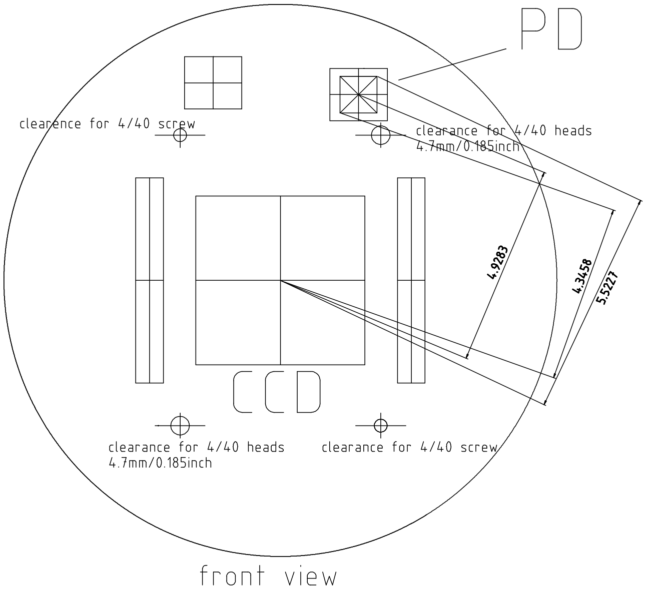

Figure 4.30: Cad drawing of the optical mask which is placed in front of the CCD and the photodiodes. The drawing allows to measure the distance of the photodiode and its corners from the center.

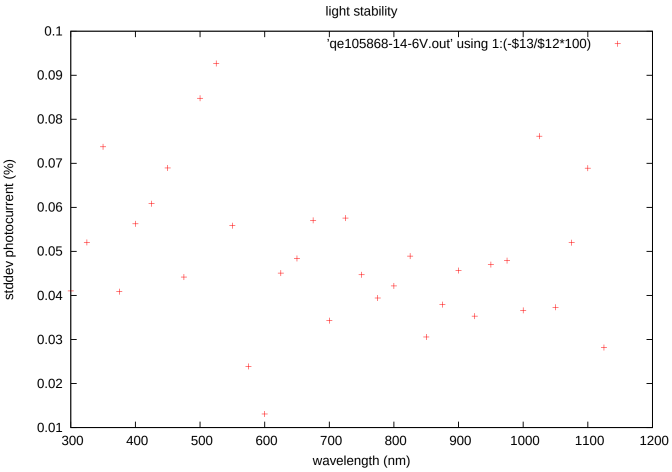

Figure 4.31: Plotted are the standard deviations of the photocurrent samples for the sphere diode during one QE scan. The stability is better than 0.1% for the whole scan.

figure 4.16 one can see that the non-uniformity in this area is smaller than 0.4%. The calibrated photodiodes used for the QE measurement is mounted at a distance of 4.93 cm from the center of the dewar window (see 4.30). The furthest corner of the photodiode has a distance of 5.52 cm from the center. The closest corner of the photodiode has a distance of 4.35 cm from the center.

The lightlevel for the photodiode is about (0.75±0.25) % lower than in the center. An effect we can easily correct for. Even though possible we have not implemented a correction for the non uniformity across the CCD yet.

4.3.10 Light stability

We decided against using the feeback stabilization of the light source for the QE measurement, and therefore had to assure that varying lightlevels are not a source of significant errors. The Keithley picoammeters are set to a half-second integration time. A build-in and about a half second long delay between the samples does not allow to measure the light intensity over the time of the whole exposure. Variations of the light intensity during these delays are not seen be the photodiode. The light intensity monitored in the dewar but also at the sphere (with much better signal to noise ratio due to hight light intensity) show standard deviations of less than 0.1% (see 4.31).

Even though we can not integrate the photocurrent over the whole exposure time the light instability will show up in the standard deviation of the multiple current samples we take for each measurement.

4.3.11 Photocurrent

The statistical noise in the photocurrent is a combination of the noise in the measurement (Keithley, noise in the photodiode and the wiring, etc.) and the instability of the light source.

The systematic error is a function of the selected range for the photocurrent measurement. We operate the currentmeter in the 2 nA range. The manufacturer claims a accuracy of 0.4% plus a 400 fA offset.

We sample the photocurrent typically eight times during one exposure as well as during the dark exposure to get an estimate for the statistical uncertainty. The substraction of the dark current eliminates any offsets. For the chosen light levels of 2000 photons/pixel/s (see Sec. 4.3.1) we typically measure a 0.1% uncertainty which might become as large as 0.2% for extreme ends of our scan range where we get the lowest light intensity.

4.3.12 Gain calibration

The gain calibration was introduced in section 2.1. An error in the gain calibration constitutes a systematic error in the QE measurement. As is explained in chapter 6 there are some problematic aspects to the classic gain calibration.

We typically reach a precision of 0.5% for the average x ray signal in ADU using the ^{55}Fe method with large values for delta (see Sec. 8.3). On top of that there is the 1% uncertainty in the actual number of electrons generated during an absorption.

The fast photon transfer curve method allows a gain calibration without knowledge of this number. The magnitude of the uncertainty depends on the size and the quality of the device. 0.2% are typical for a high quality SNAP V2 device.

4.3.13 Summarizing all effects.

An overview of all the uncertainties is given in table 4.4, table 4.5 summarizes the effects and categorizes them by the particular measurement they will affect.

Source	**Magn.**	**Comment**
Systematic effects		
Contamination	$< 3.5\%$	(abs.) if scan is done within 3:40 hours
	$< 1.5\%$	(abs.) for the first sweep in 110 min
PD mask active area	$\sim 0.3\%$	from manufacturing
	$\sim 0.2\%$	from tilting
Backreflection	$< 1\%$	depending on the reflectivity of the device
Stray light	0.8%	worst case at the extreme ends of the wavelength range
Gain		
through ^{55}Fe method	1%	due to uncertainty in electron generation
	0.5%	error due to algorithm
through FPT method	0.2%	depending on size and quality of the device
Photocurrent measurement	0.4%	quoted by Keithley for the 2 nA range
PD mode photocurrent measurement	0.2%	quoted by Keithley for the 200 nA range
Shutter error	0.1%	(corrected) 0.2% if uncorrected
Light field nonuniformity	0.45%	(corrected) 1% if uncorrected for
Wavelength	2.5 nm	calibration error
	≤ 6.4 nm	3.2 x slitwidth/1000 (in um) bandwidth
signal integration	≤ 0.01 %	
Statistical effects		
light instability + noise in photocurrent	$0.1\%\sqrt{N} \leq 0.02\|_{N\geq 8}$	shows up in the current measurement, N number of samples samples
Shutter exposure time jitter	20 ms	(= 0.1% for 20 s exposure time)

Table 4.4: Error sources

Overview over all systematic and statistical uncertainties we have identified so far.

Magn.	**Comment**	
QE measurement in CCD mode at -140° C		
	3.46 %	relative
	+ 1.5 %	absolute, due to contamination in the first sweep
	+ 3.5 %	absolute, due to contamination in the second sweep
QE measurement in PD mode at -140° C		
	3.35 %	relative
	+ 1.5 %	absolute, due to contamination in the first sweep
	+ 3.5 %	absolute, due to contamination in the second sweep
QE measurement in PD mode at 24° C		
	3.35 %	relative

Table 4.5: Summary of the systematic effects
Summary of all systematic and statistical uncertainties we have identified so far assuming gain calibration through FPT method.

CHAPTER 5
REFLECTOMETER

5.1 Setup

5.1.1 Basic principle

One well-known scheme to measure the CCDs is the VW scheme developed by John Strong [47], illustrated in figure 5.1. The advantages of this system are that the only moving part is the one mirror which changes sides during the measurement and that all components involved in the reference measurement are also involved in the reflectivity measurement itself. Therefore no calibration of any of the mirrors or the photodiode is necessary and the setup is not sensitive towards variations like changes of the reflectivity of the mirrors. All these variations cancel out in the reflectance calculation.

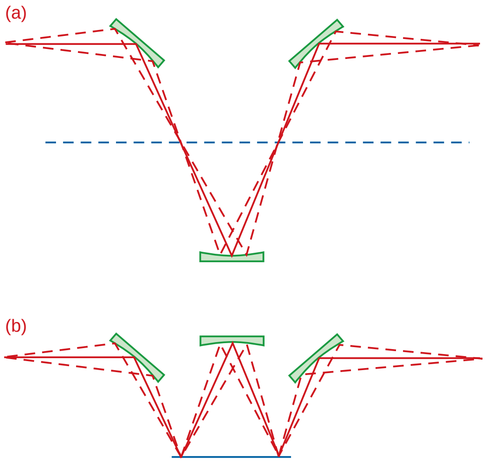

Figure 5.1: a) First the monochromatic light beam coming from the left is reflected off three mirrors giving the reference signal which is measured at the right. b) Then the sample, here the CCD, is moved between the mirrors and one mirror is moved to the other side of the probe to give the reflected signal. The ratio of the both signals gives R^2.

A disadvantage is the need for two reflections from the probe's surface. Since our CCDs only have a reflectivity of a few percent, the signal-to-noise ratio becomes unfavorable. To get a larger signal a calibrated mirror may be put at the place of the second reflection, but this makes prior calibration of this mirror necessary. Therefore we decided to design a setup which makes use of only one reflection, paying the price of having more moving parts. The measurement is done in two steps: Before measuring the actual reflected light, we first place the photodiode directly in the light beam of a spot point projector and record the beam light intensity I_0. In the

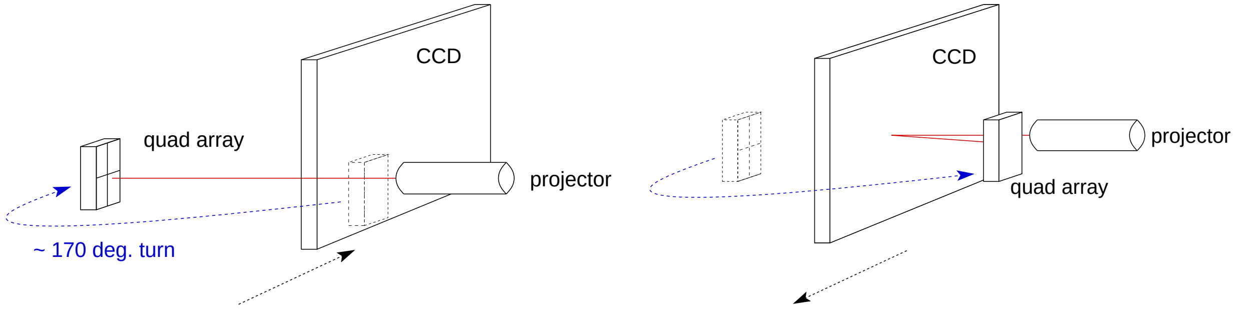

Figure 5.2: Left: The CCD is moved out of the optical path of the projector and the photodiode is moved in. The cumulative photocurrent gives I_0.
Right: The photodiode is moved out of the optical path and the CCD is moved in. The cumulative photocurrent gives I_{refl}. Then $R = I_{\text{refl}}/I_0$.

second step we then project the light spot on the surface of the CCD. The reflected light is directly measured with a silicon photodiode to give I_{refl}. Then

$$R = I_{\text{refl}}/I_0 \tag{5.1}$$

Therefore we need to move the CCD into the beam path and turn the photodiode around the CCD. The light projector is fed by an optical fiber which connects it with a monochromator. A xenon arc lamp serves as light source. A feedback system assures light stability while taking the reference measurement and the actual reflectance measurement. The setup implements several safety mechanisms to prevent the CCD from being harmed, so it allows us to measure the reflectivity of actual science grade devices.

5.1.2 Detailed description

Light source

We used the monochromator and the arc light source (100W xenon light bulb) from the QE setup described in chapter 4. The xenon arc lamp was chosen to provide more light intensity in the UV. Optical filters eliminate stray light and suppress second-order refracted light. The monochromator is equipped with a motorized input slit and a fixed output slit at the lateral port.

Spectra Physics provides a "Digital Exposure Controller" which uses feedback to stabilize the light level. It comes with a temperature-controlled photodiode to provide the feedback signal.

We decided not to use a fiber with enhanced UV transmittance, since we do not expect a match of the QE with $1-R$ in the UV due to absorption in the polysilicon layer of the CCDs. So we lose the UV part from the xenon.

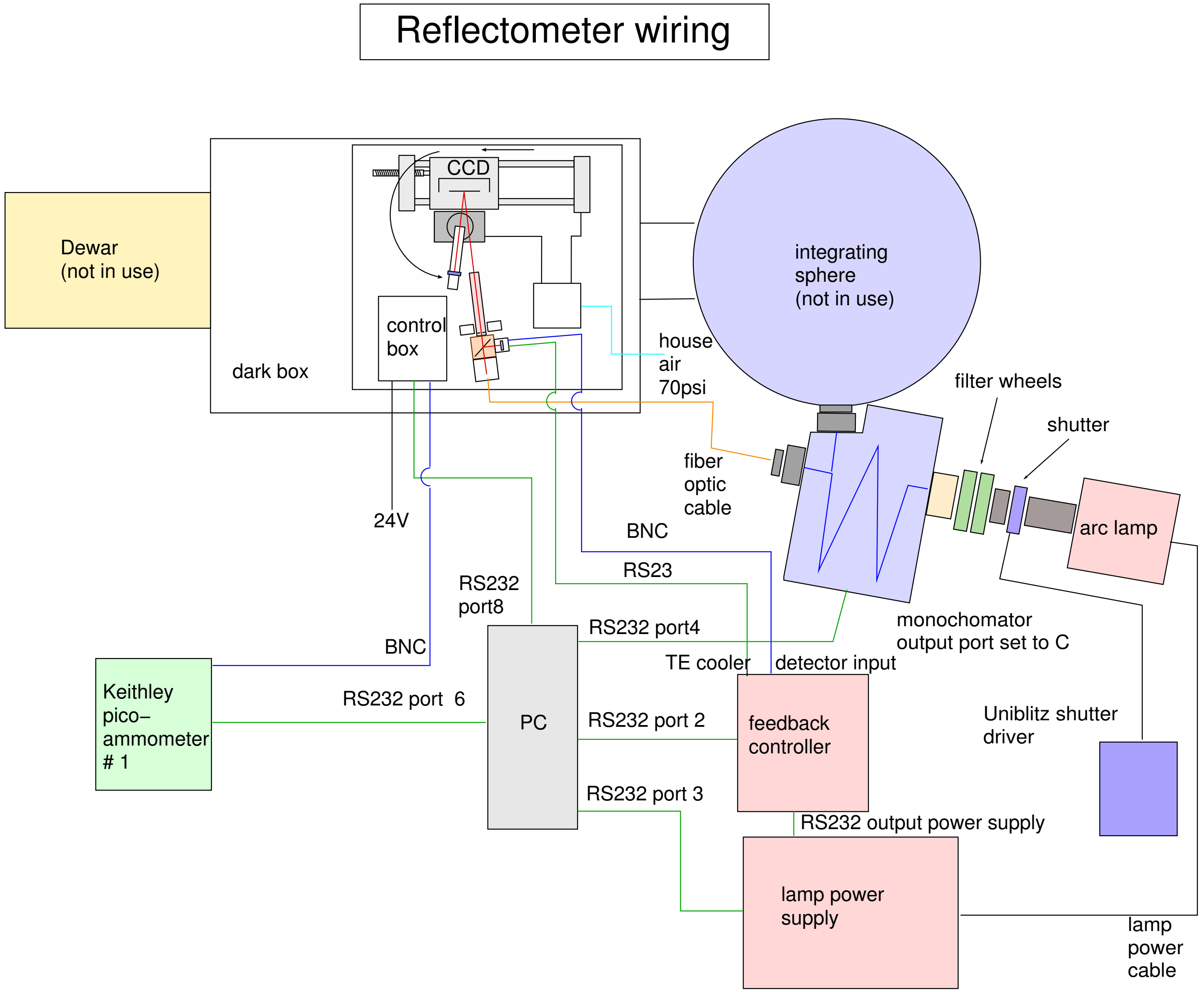

Figure 5.3: The reflectometer setup. The lightsource, monochromator and dark box are the same as in the QE setup. The reflectometer resides in the dark box.

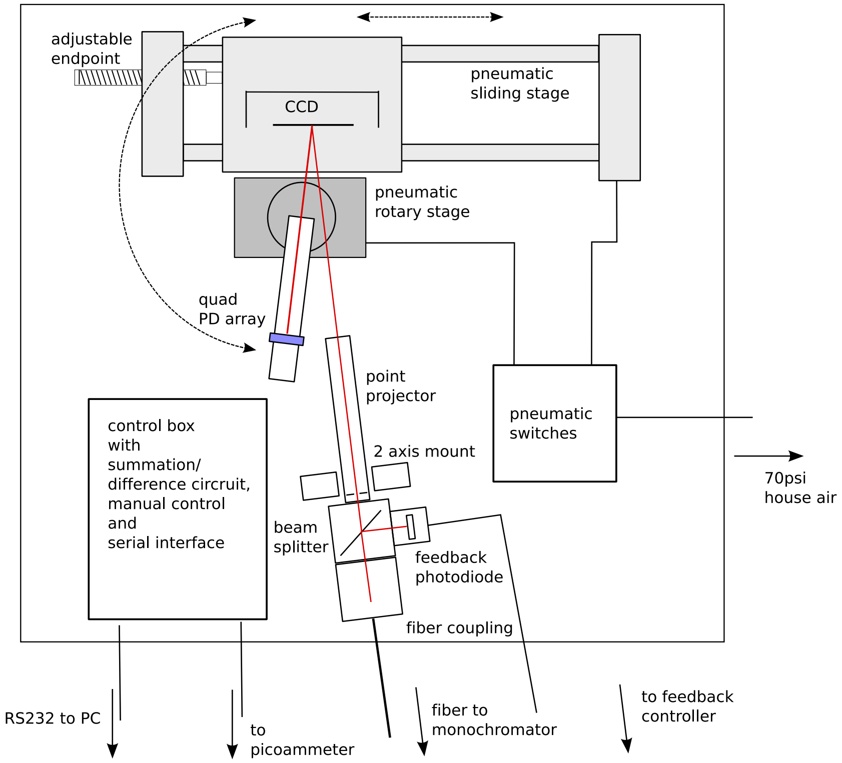

Figure 5.4: Closeup of the reflectometer. The CCD is mounted on a pneumatic sliding stage. It can be adjusted for tilt around two axis and for focus. A point projector equipped with a feedback assembly for light stabilization provides the probing beam. A quad-array photodiode measures first the light beam directly then the reflected beam. Using a quad array allows careful beam centering.

Projector and feedback

We measure the reflectance at an incident angle of 7°. Therefore in the reflectivity measurement position the beam projector and the photodiode are separated by an angle of 14°. The beam projector was adopted from an old wire bonder, where it served as crosshair projector. We took the crosshair mask out and replaced it by a 1 mm aperture mask. The projector has a focal length of about 7.8 cm. We made a beamsplitter which attaches to the end of the projector. The optical fiber feeds into the beam splitter. We disassembled the feedback photodiode box from the Spectra Physics “Digital Exposure Controller” and build the photodiode into the beamsplitter. The result is a compact projector/feedback assembly which is mounted using an mirror mount. The mirror mount has fine-adjustment micrometers for two axes which allow us to center the light beam on the photodiode (see Fig. 5.5).

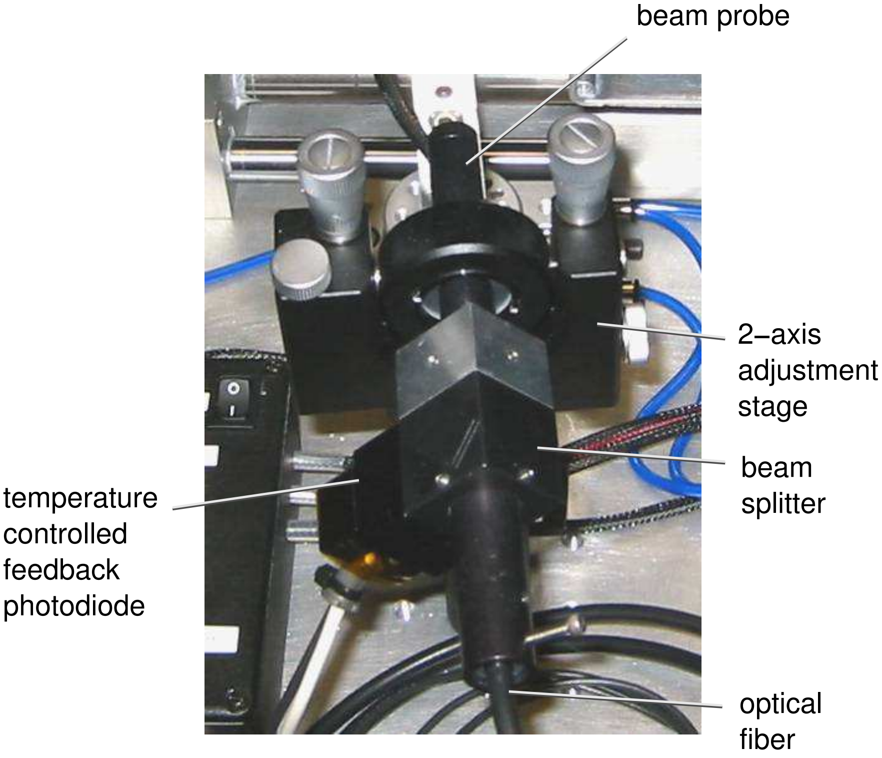

Figure 5.5: The beam probe assembly. The beam probe projects the light spot onto the CCD's surface. A beam splitter and a temperature controlled photodiode stabilize the light during the reference and the reflectivity measurements. A mirror mount was used as fixture for the beam probe. Two micrometer screws allow adjustment of the beam probe around two axis.

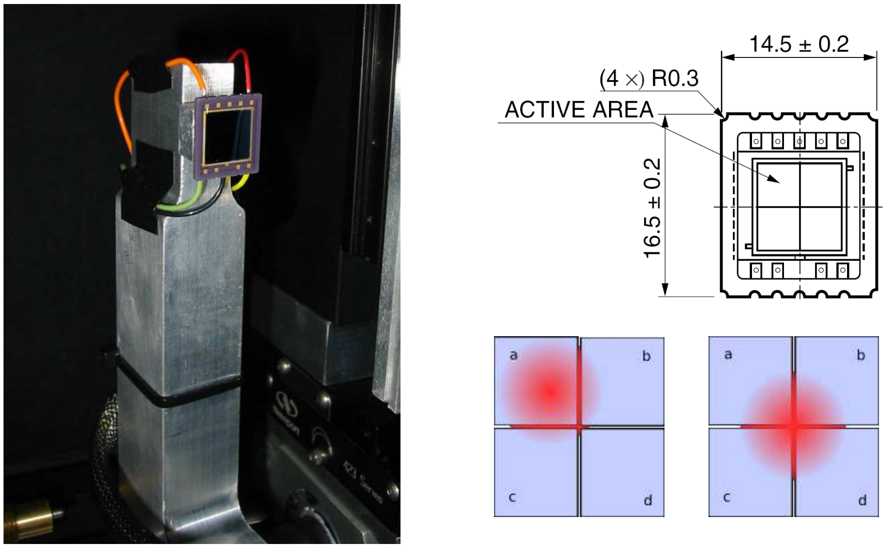

Figure 5.6: Quad array of the reflectometer
The usage of a quad array photodiode instead of a single photodiode allows to very carefully center the reflected lightbeam on the detector. Displays on the controlbox show the differential signals $v = (a+b)-(c+d)$ and $h = (a+c)-(b+d)$ and the sum $\Sigma = a+b+c+d$. For example, a situation where the light beam is off center located mostly on quadrant a would result in $v > 0$ and $h > 0$. The operator adjusts the micrometer screws until $v = h = 0$.

Photodiode quad array

It is important to capture the whole beam diameter at both measurement positions. Therefore, instead of using a single photodiode, we use a quad array (see Fig. 5.6). Using a summation/difference circuit we can center the light beam precisely on the photodiode. The quad array is mounted on a lever which is attached to a rotary pneumatic actuator. The actuator turns the photodiode between the two measurement positions. A reed switch interlock assures that the photodiode can not accidently be moved into the beam path while the CCD is still in position. As illustrated in figure 5.7 we tilted the photodiode to avoid the capture of light reflected off the photodiodes surface onto the CCD an back onto the photodiode. In fact we were unable to reproduce the calculated curves for silicon before employing this trick.

Even though the visible spot on the photodiode is not larger than about 3 mm in diameter, one concern was that the light spot might actually be larger than the 10 mm by 10 mm photodiode, so that the photodiode does not intercept the whole beam. After having centered the beam on the quad array, we moved the spot using the micrometers on the mount of the light projector and observed the output on the picoammeter. We found the light intensity to be insensitive to small movements of

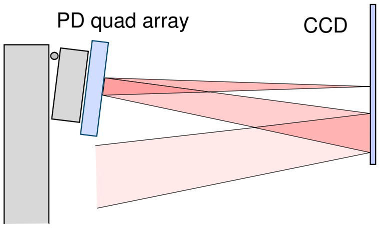

Figure 5.7: The photodiode quad array is slightly tilted to avoid the capture of backreflected light.

the spot.

Since the reflectivity is measured at an incident angle of 7° but the QE is measured for light of normal incident angle a slight difference between QE and $1 - R$ is to be expected. The antireflective coatings were developed for light of normal incident angle. Light of different incident angle will increase the length of the beam path through the coating layers and therefore cause a change of the measured reflectivity.

Since we probe with a cone shaped light beam, we actually integrate over an angular range of about 3.5° to 11.5°.

CCD stage

The CCD is first mounted on a two-axis tilt platform, allowing the reflected beam to be centered on the quad array. This assembly is mounted on additional slides for focus adjustment and selection of the vertical position of the actual point on the CCD's surface where the reflectivity is to be measured. Finally everything is mounted onto a pneumatic slide which allows the CCD to be moved back and forth between both measurement positions. By adjusting the endpoint of the slide the horizontal position of the point to measure the reflectivity is selected. Again a reed switch makes sure that under no circumstances can the CCD and the photodiode collide.

Automation

The pneumatic stage of the CCD and the rotary actuator of the photodiode are connected to an electrically controlled pneumatic manifold. We built a circuit with a microcontroller (PIC) to allow communication with a PC over the serial port. Finally a JAVA program controls and automates the measurement.

Signal measurement

The total photocurrent of the quad array is measured by a Keithley picoammeter. The serial port of the picoammeter allows communication with the control software.

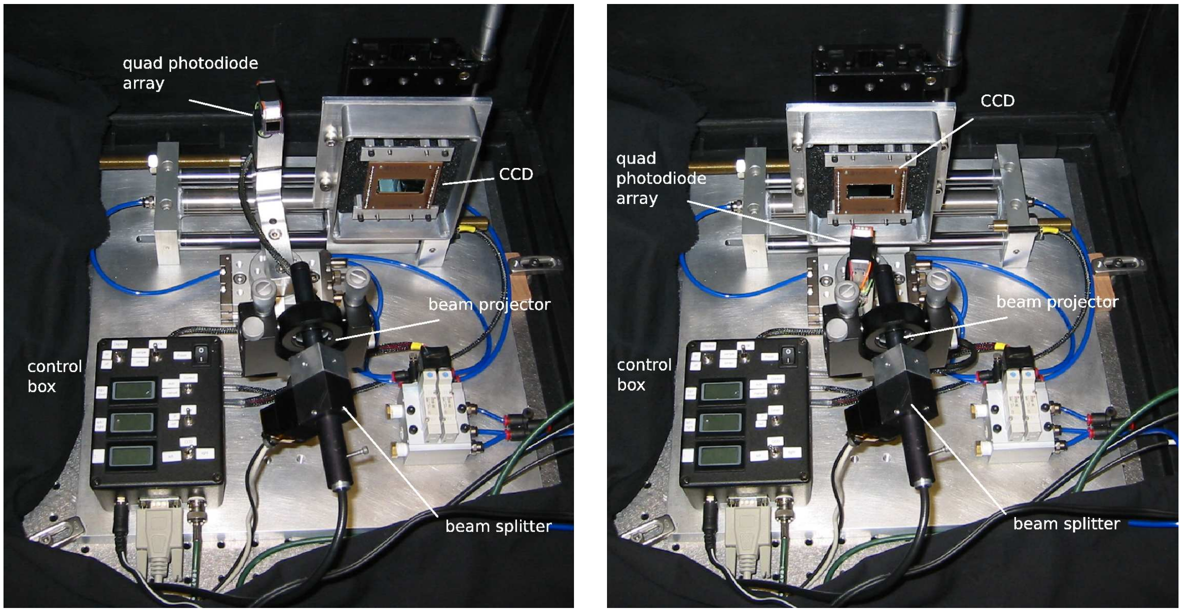

Figure 5.8: The actual reflectometer. A CCD is mounted to be tested.
left) Reflectometer is in position to record I_0 the photodiode faces the beam projector directly.
right) The I_{refl} measurement mode. The light beam from the projector reflects off the CCDs surface and gets intercepted by the photodiode.

Dark box

The reflectometer resides in a dark box, the same box which provides the 80 cm drift space for the QE setup (see Fig. 5.3). There are electrical feedthroughs at the ends of the dark box for communication with the PC and the picoammeter.

5.2 Measurement procedure

5.2.1 System setup

The CCD is placed in a box assembly to protect it from ESD damage, being touched or collecting dust. Only after the box is attached to the CCD stage is the lid is taken off and the CCD exposed the ambient air.

The actual location on the surface of the CCD where the reflectivity is to be measured is then selected. The setup allows any spot on a surface of 5 cm by 5 cm to be chosen.

Part	Manufacturer	Model
Light source		
see table 4.1.2 and 4.1		
Point projector		
Modified crosshair projector from wire-bonder	Volpi	-
In-line mirror mount	Opto Sigma	112-2630
CCD stage		
Tilt platform	Opto Sigma	123-2240
Sliding stage	Newport	423
Sliding stage	Newport	433
Right angle bracket	Opto Sigma	123-8130
Rodless pneumatic slide	Bimba	Ultran USS-0605.000-A1
Quad array		
Quad photo array 2x2 elements 10x10mm active area	Hamamatsu	S5981
Adjustable-angle rotary air actuator	SMC	MSQB10A-DIH00456
Current meter		
Picoammeter	Keithley	6485

Table 5.1: Part list for the LBNL reflectometer reflectivity measurement setup. A detailed description for the monochromator and the light source can be found in [17].

5.2.2 Centering

To assure that the photo diode array actually captures of the whole light beam, the light beam has to be carefully centered on the quad array. The monochromator is first set to a convenient wavelength. Using visible light simplifies the procedure. The slitwidth of the monochromator input port is set to its maximum.

Displays on the control box show the differential signal of the left and right half of the quad array and the difference of the top and the bottom half signal. A third display shows the overall signal. Toggle switches allow selection between manual control of the setup and automatic control i.e. the computer. In the manual mode, the CCD slide and the photodiode lever are operated using switches. The photocurrents of the four diodes in the quad are selected to be processed either by the summation/difference circuit or to be measured in parallel by the picoammeter.

At first, the setup is adjusted for the reference measurement. The photodiode lever is positioned for the reference measurement i.e. the photo diode array is placed so that it directly faces the projected beam. Using the micrometers of the projector mount, the light beam is centered on the quad array. Then the CCD and the photodiode are positioned for reflectance measurement. The CCD now faces the projector. The light beam reflects off the CCD's surface. The quad array is placed close to the projector output. Using the tilt platform on which the CCD is mounted, the light beam is again centered on the quad array.

5.2.3 Measurement

For each selected wavelength the control software records the dark current I_{dark}, the reference light intensity I_0 and the reflected light intensity I_{refl}. We chose to take ten current samples for each measurement of I_{dark}, I_0 and I_{refl} with one second integration times.

As a first step the software positions the CCD and the photo array in a neutral position. The dark current I_{dark} from the photodiode is recorded. The photodiode array is then positioned in the light path so that it faces the beam projector and I_0 is recorded. For the actual reflectivity measurement the CCD is then moved into the beam path. The photodiode array is positioned next to the beam projector facing the CCD and I_{refl} is recorded. Finally the reference measurement is repeated to verify the light stability.

CHAPTER 6

IMPROVED GAIN CALIBRATION

6.1 Advanced x ray identification

The standard x ray gain [25] calibration - i.e. the currently at the SNAP group used ^{55}Fe method - has two problems. First, it shows a dependency on the chosen region of interest (ROI) in the x ray image and of the user provided delta value. The delta value is a threshold which determines what signal a pixel value has to exceed in order to be counted a x ray event.
Second, the value used for the number of generated electron-hole pairs per x ray photon is only known within about 1% .
We found the reproduceability of the average x ray signal to be in the order of 0.5%. Resulting in a 1.5% uncertainty the gain calibration. Two ways to improve the situation were explored. We tried to improve the x ray identification algorithm to eliminate the dependence of the chosen region and the delta value. A modification of the photon transfer curve method the *fast photon transfer curve* [8] provides an alternative method for the gain calibration.

6.1.1 The original algorithm

The improved algorithm tries to eliminate two reasons for the ROI and delta dependence and the variation of the results. The delta value tells analysis software when to consider a pixel as a possible x ray event. The algorithm will "draw" a box - either 3 × 3 pixel or 5 × 5 pixel large - around each pixel which signal exceeds the background value of the x ray image plus delta. For each box the pixel values in the box will be summed up. The resulting value is considered (after background substraction) to represent the number of ADUs which result from the number of electrons which got produced by that particular x ray event in the silicon. If the number of electrons per x ray event is known, one can calculate the system gain, i.e. how many ADUs are measured for a certain number of electrons. A large number of x rays allows a relatively precise calculation of the gain.

A ^{55}Fe x ray source is used. ^{55}Fe decays into ^{55}Mn which in turn emits 5.90 keV x rays after the decay.

Now in backside illuminated devices a x ray event is typically not contained in just one pixel. Instead it will spread over a number of pixel. Therefore we integrate the x ray signal over 5 × 5 pixel large boxes for backside illuminated devices. If the provided delta value now is too small, the standard algorithm might consider two neighboring pixel with large signal values as two different x rays events. Not only the integrated signal in the two different resulting boxes will be correlated, it might also be different. The smaller the delta value the more likely it becomes that boxes are drawn around pixel which actually lie in some distance (one to three pixel, or so)

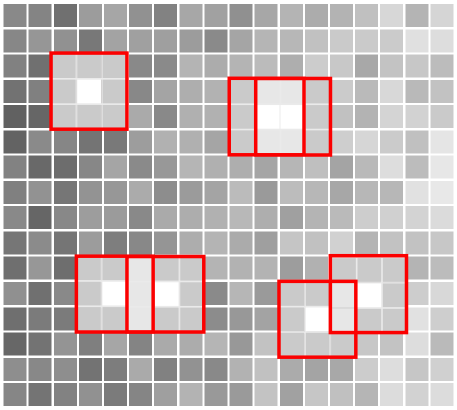

Figure 6.1: Illustrates several possible events. On the top left the x ray event is mainly contained within one pixel. The algorithm correctly identifies it as only one event and draws one integrating box around the event.
On the top right one x ray event spreads over two pixel. The selected delta value was too small and the algorithm wrongly draws two boxes. The event will be counted twice.
On the bottom left and the bottom right two nearby x ray events resulted in overlapping integration boxes. Such overlaps will result in too large signal estimations per x ray.
A basline shift is illustrated. Such a shift in the dark signal i.e. the signal where no x ray interacted with silicon is not treated in the original code. One has to substract a dark image, hoping that the dark image and the actual exposure would show exactly the same basline shifts.

of the real event. The resulting boxed will then not integrate over the whole x ray event but only contain part of its signal. This will result in a wrong too low estimate of the number of ADUs for one x ray event.

To improve statistics one would like to work with a large number of x rays (longer exposure). But as the density of x ray events in the CCD increases, the probability of two events being very close to each other increases. Pixel may then contain electrons from more than one event. If the boxes which are drawn around the x rays events start to actually include electrons from neighboring x rays events, the estimated signal per x ray would be too high.

Finally the algorithm leaves the possibility of an insufficient background substraction. Normally a dark image - an image with the same exposure time but no x ray exposure - is subtracted. This is necessary since the original algorithm can not handle shifts in the base line. It fits a gaussian to the histogram resulting from the x ray image to determine the background level. This method does not compensate for any shifts in the basline. If the shifts in the baseline of the dark image and the actual x ray exposure are not identical, residual shifts will result incorrect background substraction. Also, the method of the gaussian fit introduces a systematic

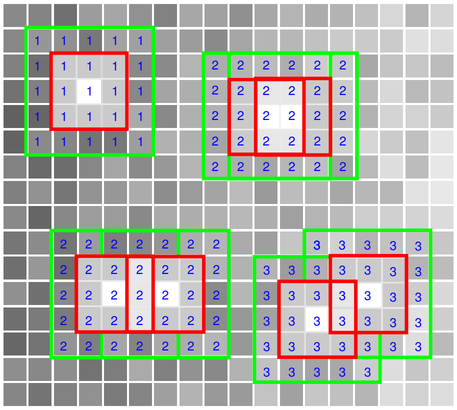

Figure 6.2: Shows how the algorithm addresses the problems of overlapping and background substraction. The new algorithm labels the boxes for the signal integration. If two boxes overlap they are combined into one integration area.
An additional lager box is drawn around each of the signal integration boxes. The background is individually calculated for each of these larger boxes and subtracted from the contained integration box avoiding systematics and being less sensitive to baseline drifts.

effect. Since the same value is subtracted for all pixel, the x ray signals may be systematically off.

6.1.2 Attempt to improve the algorithm

The basic idea is to still draw boxes around pixel which exceed the background level by some given delta value. But now the algorithm checks, while drawing the boxes, whether already any of the pixel are part of another box. Each pixel in the box is labeled by its box number. If the algorithm tries to add any pixels into a box which are labeled already, all the pixel in this new box will get labeled with the same label (see Fig. 6.2 left). If now boxes of two events overlap, they will enter the histogram as a two-x ray event and can easily be rejected since the have a twice as large signal as the normal x ray event. If accidently two boxes are drawn for only one x ray, the signal of these boxes will be combined.

To improve the background substraction, a lager box around each x ray event box is drawn. The background is then calculated from each pixel which is part of the larger box but not of the x ray integration box (see Fig. 6.2 right). This approach also eliminates the systematics caused by the substraction of a fixed value and shows less sensitivity towards drifts in the baseline.

The actual algorithm can be found in appendix C.2.

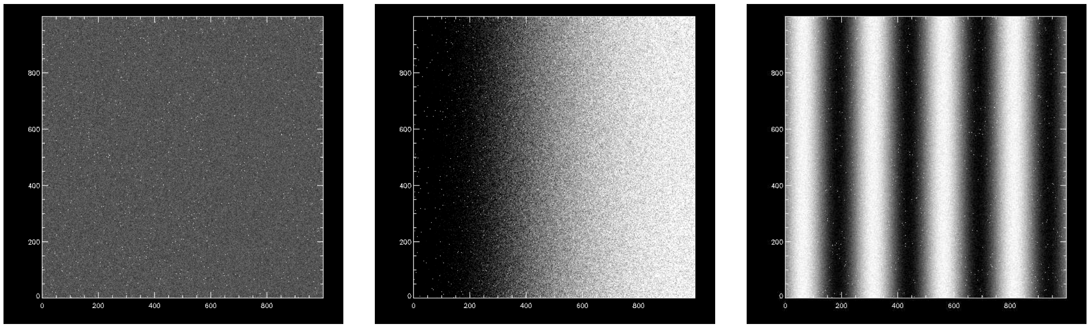

Figure 6.3: Shows three different synthetic x ray images. The improved x ray identification algorithm was first tested on such images. All images are 1000 × 1000 pixel large. The background is 1000 ADU. The synthetic x rays have a signal value of 2500 ADU. The density of x rays was one photon per 300 pixel. A system noise of 10 ADU was applied.

left) Simulates no baseline drift. The old algorithm estimates an average x ray signal signal of 2504.24 ± 0.13 (delta = 1300) whereas the new algorithm correctly states 2500.66 ± 0.93.

left) Simulates a slow baseline drift. A sinusoidal baseline drift with a period of a 2000 pixel and an amplitude of 100 ADU was added to the x ray image. The new algorithm estimates 2498.65 ± 0.82. The correct answer lies within the stated two sigma interval.

left) Simulates a fast baseline drift. A sinusoidal baseline drift with a period of a 250 pixel and an amplitude of 100 ADU was added to the x ray image. The new algorithm correctly states 2499.85 ± 0.92.

Such tests on synthetic images proved to be of great value for benchmarking the algorithms.

6.2 Fast Photon Transfer Curves

A well established method to measure the system gain is the so called photon transfer curve. As in any counting experiment the number of photons per pixel in a flat field image of mean photon level N_γ will be subject to the variance

$$\sigma_\gamma{}^2 = N_\gamma \tag{6.1}$$

This variation is typically referred to as shot noise and is also true for the number electrons per pixel if the quantum efficiency is not 100% as long as the QE is equal for all pixel.
Then the average number of electrons per pixel is

$$N_{\mathrm{e}^-} = QE \cdot N_\gamma \tag{6.2}$$

And still variance of the number of electrons per pixel is

$$\sigma_{\mathrm{e}^-}^2 = N_{\mathrm{e}^-} \tag{6.3}$$

. We measure the signal s of one pixel in ADU. It is

$$s = g \cdot n_{\mathrm{e}^-} \tag{6.4}$$

where n_{e^-} is the number of electrons in one pixel and g is the system gain. By writing down the formula for the variance one can see then that

$$\begin{aligned}
\sigma_s^2 &= \frac{1}{n-1}\sum_i (\bar{s} - s_i)^2 && (6.5)\\
&= \frac{1}{n-1}\sum_i (g \cdot N_{\mathrm{e}^-} - g \cdot n_{\mathrm{e}^- i})^2 && (6.6)\\
&= \frac{g^2}{n-1}\sum_i (N_{\mathrm{e}^-} - n_{\mathrm{e}^- i})^2 && (6.7)\\
&= g^2 \cdot \sigma_{\mathrm{e}^-}^2 && (6.8)
\end{aligned}$$

but with equation 6.3 and 6.4

$$g^2 \cdot \sigma_{\mathrm{e}^-}^2 = g^2 \cdot N_{\mathrm{e}^-} = g \cdot S \tag{6.9}$$

so that

$$\sigma_s^2 = g \cdot S \tag{6.10}$$

where S is the average signal in the flat field. This equation is true as long as the noise in the image is dominated by shot noise and can be used to calculate g from a large number of exposures of different light intensity or exposure times. If one plots σ_s^2 versus the signal S one can fit a line to determine g.

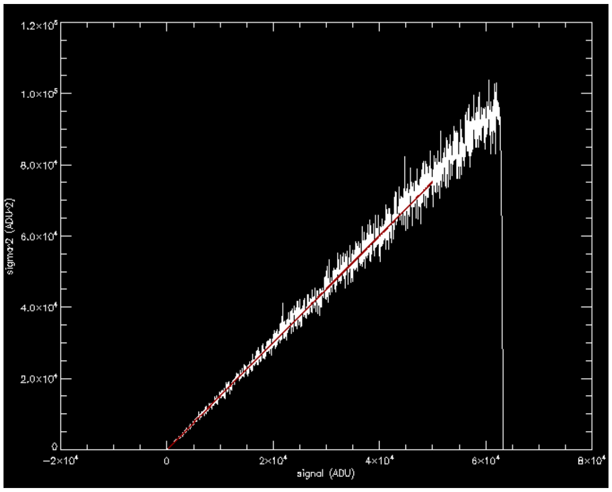

Figure 6.4: Shows a plot of the signal variance versus the signal level. A fit of a straight line to this curve gives the system gain (when choosing the fit region carfully).

Now, the same argumentation is still true for a single row in a CCD as long as each pixel in that row was illuminated by the same light intensity. So instead of taking a large number of flat field images [8] proposed to take only one image where each row was exposed to a different amount of light. This can easily be achieved by starting to read the CCD out and opening the shutter during the read-out. This results in a gradient image as shown in figure 6.5.

The rows which are read out last will have the largest signal whereas the rows which are read out first will have the smallest signal. By calculating the average signal and the variance of the signal for each row one can then use equation 6.10 to calculate the system gain. This is done by fitting a linear function to the signal variance versus the signal. The error on the standard deviation σ_s is given by

$$\sigma(\sigma_s) = \frac{\sigma_s}{\sqrt{2N}} \tag{6.11}$$

(see appendix B) then

$$\sigma(\sigma_s^2) = \frac{\sqrt{2}\sigma_s^2}{\sqrt{N}} \tag{6.12}$$

Since this method relies and the know relationship between the shot noise and the average light level, it will fail if the CCD has a poor CTE. If charge is referred from one pixel to the next, the signal of those pixels is then correlated and not subject to shot noise only any more. The fast photon transfer curve method therefore requires CCDs with high CTE. No attempts have been made so far to determine the minimum required CTE.

The actual algorithm can be found in appendix C.1.

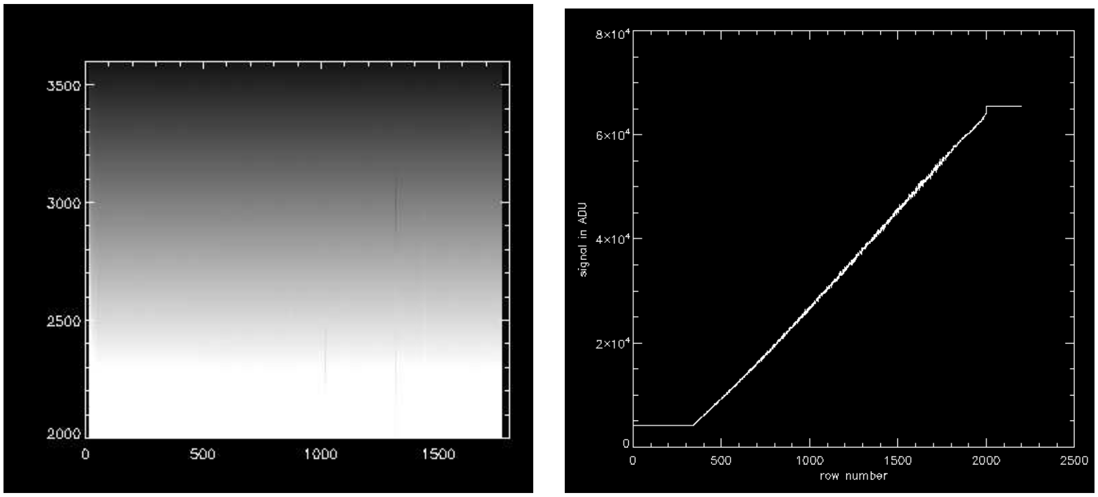

Figure 6.5:

left) Shows a gradient image as used the generate a fast photon transfer curve.

right) Shows a plot along column number 500 of the same image. One can see that the first part of the image is not exposed to light since the readout started before the CCD was exposed to light. This area will be used to determine the baseline signal and the read noise. The lightlevel is chosen so that the ADC saturates during the readout.

As for the improved gain calibration, synthetic images with know gain were generated to test the analysis algorithms.

CHAPTER 7
ANALYSIS

7.1 QE CCD mode

The average CCD signal per pixel S_{CCD} is calculated from a previously selected region. The region is chosen so that is avoids edge regions and cosmetic defects but is as large as possible. It might also focus on a special region of interest e.g. an irradiated part of a CCD.

The average signal per pixel S^* is calculated for that region, the average signal S_{dark} for the same region in the dark image is calculated and subtracted from the flat field image.

$$S_{\mathrm{CCD}} = S^* - S_{\mathrm{dark}} \tag{7.1}$$

The dark current I_{dark} of the calibrated photodiode is subtracted from the actual photocurrent I^*.

$$I_{\mathrm{PD}}^{**} = I^* - I_{\mathrm{dark}} \tag{7.2}$$

The photocurrent then has to be corrected for the light field nonuniformity (see Sec. 4.3.9).

$$I_{\mathrm{PD}} = I_{\mathrm{PD}}^{**} \cdot 1.0055 \tag{7.3}$$

The gain is calculated from the x ray image taken at the beginning of the measurement (see Sec. 2.1 and 6) or a gradient image might be taken for higher accuracy.

The exposure time $T*$ has to be corrected for the shutter delay (see Sec. 4.3.8).

$$T = T^* - \Delta_T \tag{7.4}$$

Finally the quatum efficiency is calculated from

$$\mathrm{QE}_{\mathrm{CCD}} = \frac{e \cdot S_{\mathrm{CCD}}}{G \cdot T \cdot I_{\mathrm{PD}}} \cdot \mathrm{QE}_{\mathrm{PD}} \cdot A_r \tag{7.5}$$

. The analysis is mostly done automatically in a JAVA. The gain calibration and the selection of a region of interest are the only manual steps.

7.2 QE photodiode mode

As stated in chapter 2.5.2 the photodiode mode quantum efficiency is calculated from

$$\mathrm{QE} = \frac{\mathrm{QE}_{\mathrm{PD}} \cdot I_{\mathrm{CCD}} \cdot A_{\mathrm{PD}}}{I_{\mathrm{PD}} \cdot A_{\mathrm{CCD}}} \tag{7.6}$$

where QE_{PD} is the quantum efficiency of the calibrated photo diode, I_{CCD} is the photocurrent generated by the CCD, I_{PD} is the photocurrent from the photodiode, A_{CCD} and A_{PD} are the active areas of the CCD and the photodiode.

Critical is the substraction of the dark current from the actually measured current I^*_{CCD}. We sample the dark current before and after the actual measurement and substract the average. The same substraction is performed for the measured current from the photodiode.

$$\mathrm{QE} = \frac{\mathrm{QE}_{\mathrm{PD}} \cdot (I^*_{\mathrm{CCD}} - I_{\mathrm{CCDdark}}) \cdot A_{\mathrm{PD}}}{(I^*_{\mathrm{PD}} - I_{\mathrm{PDdark}}) \cdot A_{\mathrm{CCD}}} \tag{7.7}$$

When looking at the data for a room temperature photodiode mode measurement for device 105868-14-6 with a dark current of

$$I_{\mathrm{CCDdark}} = (17.9630 \pm 0.0001)\mathrm{nA} \tag{7.8}$$

and a photocurrent of

$$I^*_{\mathrm{CCD}} = (18.8358 \pm 0.0001)\mathrm{nA} \tag{7.9}$$

at 800 nm one sees that the actual *photo generated* current

$$I_{\mathrm{CCD}} = I^*_{\mathrm{CCD}} - I_{\mathrm{CCDdark}} = (0.8728 \pm 0.0001)\mathrm{nA} \tag{7.10}$$

is very small compared the the dark current. This is due to to bias voltage we apply to the CCD.

Keithley quotes a 0.2% systematic error in the current measurement for the gain range of 200 nA. Due to the large photo and dark current but their small differences this would result in large errors for the room temperature measurement. But since both the photo and the dark current measurements are taken with the same picoammeter, the effective relative error in their difference is also only 0.2% .

CHAPTER 8

RESULTS

8.1 Reflectometer

8.1.1 Reflectance measurement for silicon

We measured the reflectivity of a piece of unprocessed silicon i.e. a wafer (see Fig. 8.1). The wafer was etched in hydrofluoric acid before the measurement to eliminate possible surface contaminations. The first data showed a too high reflectivity in the blue. We found the reason in a backreflection which we were able to eliminate by tilting the photodiode slightly (see Sec. 5.1.2). In the wavelength range from 400 nm to 1000 nm we now reach good agreement with the calculated value of the reflectivity

$$R = \frac{(n-1)^2 + k^2}{(n+1)^2 + k^2} \tag{8.1}$$

where the refactive indices n were taken from the Handbook of Optical Constants of Solids [10] and the absorption for room temperature k was calculated using the parameterization from Rajkanan, Singh, and Shewchun [39].

8.1.2 Reflectivity measurement for device 86135-7-7

We then measured the reflectivity of a thick, fully depleted CCD developed at the LBNL. Our reflectivity measurement agrees well with the data from the UCO/Lick observatory as shown in Fig. 8.2.

8.1.3 Repeatability

To test the setup for repeatability we measured the reflectivity for a selection of wavelengths 10 times in one day. The largest fractional standard deviation we found for ten consecutive measurements was 0.3% for 1000 nm. To test the longterm stability we repeated the reflectivity scan for one device with a three month time interval between the two tests. Figure 8.3 shows curves taken of the same device in September and in December 2005.

8.1.4 Sources of errors

The noise for the photocurrent measurement is negligible, and the variations in the light intensity are very small. The standard deviation for the ten samples of I_{refl} at each wavelength is shown in Fig. 8.4 to be never greater than 0.02%. The signal to noise ratio for I_0 is larger.

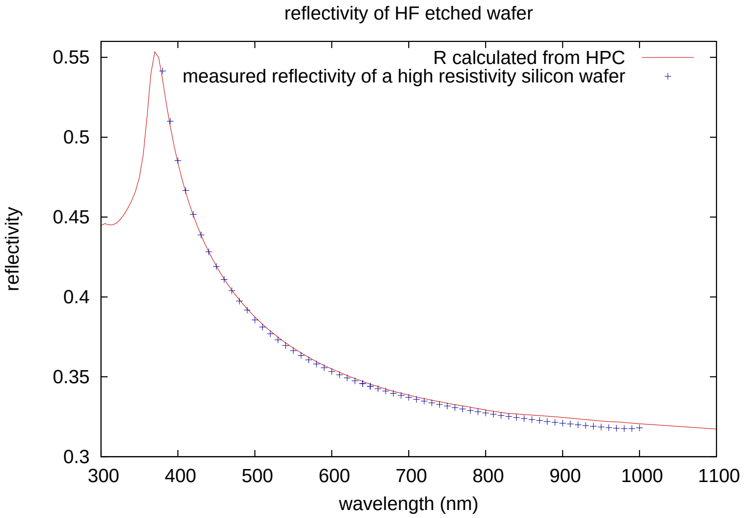

Figure 8.1: Shows the measured and the calculated reflectivity of a piece of a silicon wafer and the calculated reflectivity. The wafer was HF etched before the measurement to eliminate surface contamination. The measured and the calculated curve show good agreement. The absolute difference is not lager than 0.005.

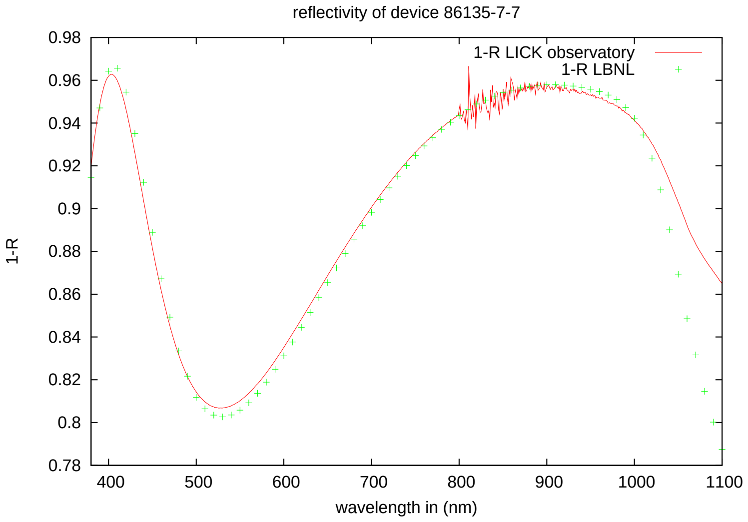

Figure 8.2: $1-R$ for device 86135-7-7 measured at LBNL and the UCO/Lick observatory.

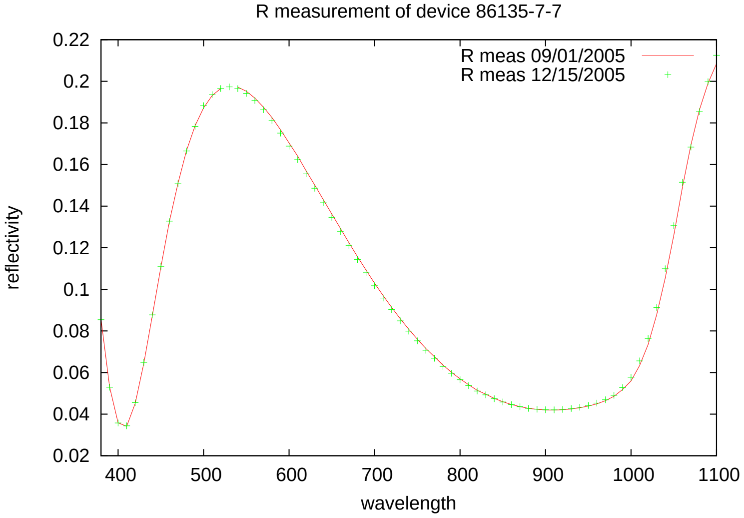

Figure 8.3: The two measurements of $1 - R$ for device 86135-7-7 match well.

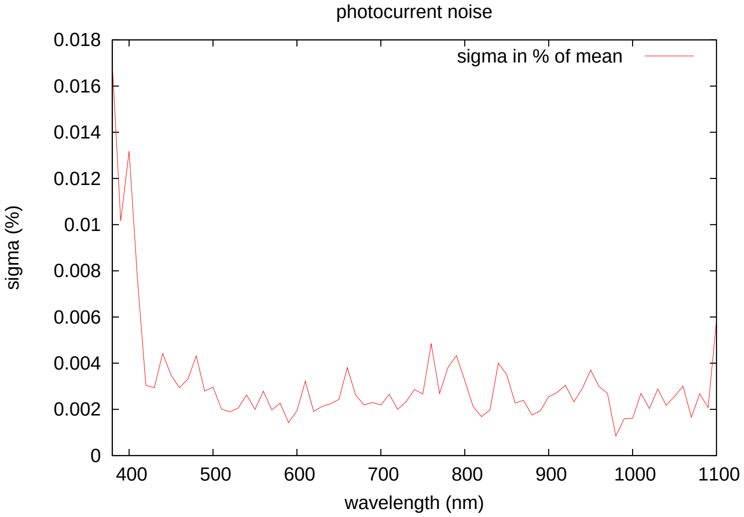

Figure 8.4: Shows the noise of I_{refl} from one scan.

8.2 QE calculation

Figure 8.5 shows the calculated quantum efficiency for device 105868-14-6

$$QE = 1 - R - T - a_{\mathrm{AR}} \tag{8.2}$$

where a_{AR} is the absorption in the backside coatings once ignoring and once including absorption in the ITO layer. $1 - R$ and $1 - R - T$ are shown also. The results of the calculation may be compared to the actual measured reflectivity and quantum efficiency which are shown as gray curves in the background. The oscillations of the calculated curves in the red are due to fringing. They are not seen in the measurements. This calculation used the thicknesses which were measured during the deposition of the backside coatings.

Between 400 nm and 900 nm the calculated QE is too high by up to 8%. Below 400 nm the calculated QE is actually lower than the measured QE. But also the measured and the calculated reflectivity do not match. They show differences of up to 8% in the range 400 nm and 900 nm. Below 400 nm the disagreement is actually worse and measured features like the minimum of 1-R around 400 nm and the maximum around 370 nm are not reproduces well in the calculation.

Including the ITO absorption produces better results as one can see in second figure 8.5. Still the reflectivity curves do not agree.

The upper figure 8.6 shows again the calculated quantum efficiency, $1 - R$ and $1-R-T$ compared to the actual measurement. The Levenberg-Marquardt nonlinear fitting algorithm was used to vary the thicknesses of the backside coatings to reach optimal agreement between calculated and measured reflectivity. Besides a slightly higher than measured reflectivity around 490 nm, the calculation shows a fairly good agreement over the whole spectral range down to 380 nm where our measurement looses accuracy due to the loss of light intensity caused by absorption in the optical fiber.

Starting from the hypothetical device we now included the absorption in the ITO layer in our calculation. Shown in the bottom figure 8.6 are again the calculated quantum efficiency $QE = 1 - R - T - a_{\mathrm{AR}}$, $1 - R$ and $1 - R - T$, but a_{AR} now does include the ITO absorption.

Finally we increased the thickness of the poly silicon layer in the calculation from the measured 22.5 nm to 30 nm. We see that the absorption in the ITO layer combined with an increased thickness of the poly silicon layer produces a calculated curve which is in fairly good agreement with the measurement. We can, so far, not explain the differences of the measured thicknesses and the thicknesses we reach optimal agreement for. They are possible due to uncertainties in the thicknesses of

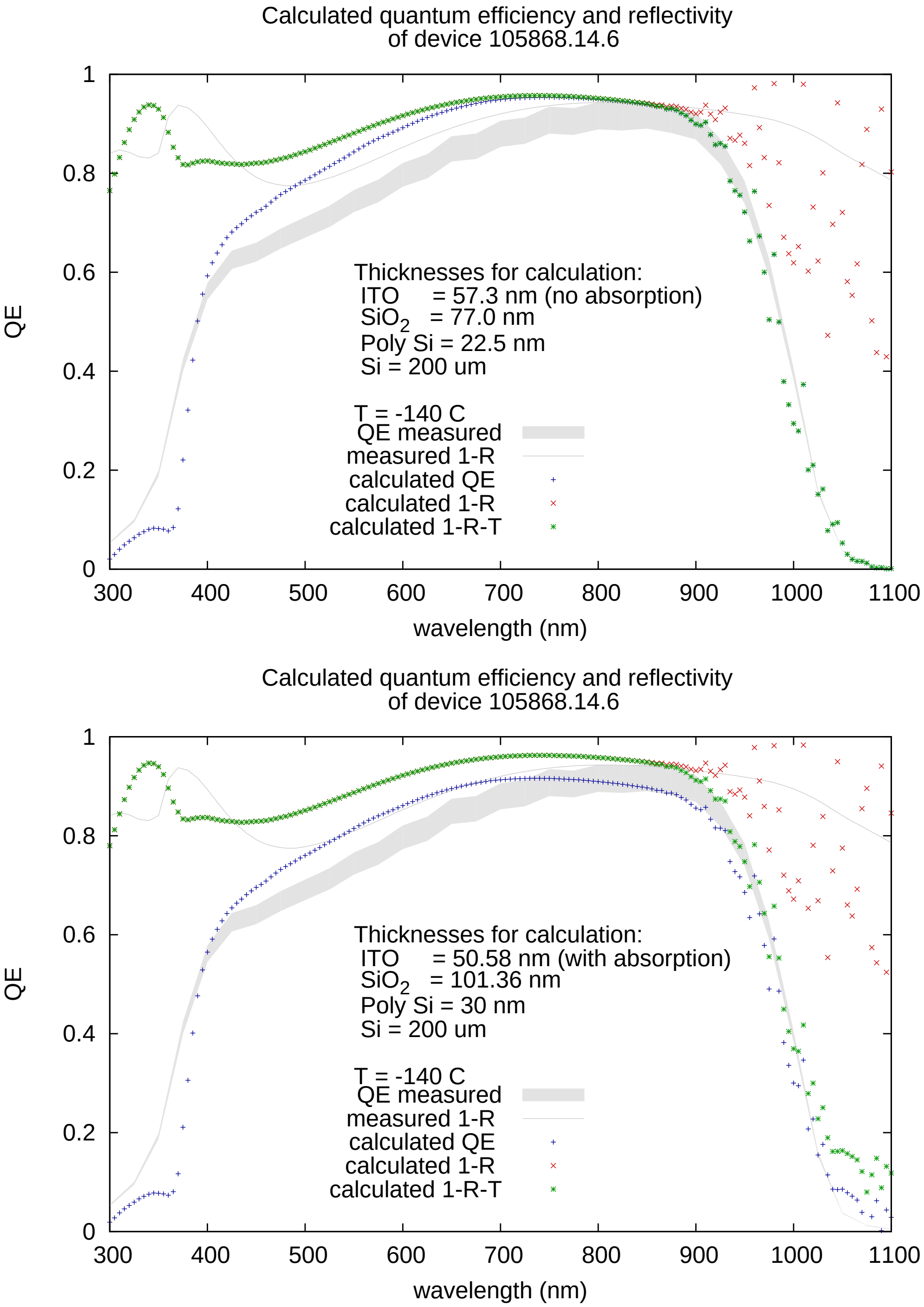

Figure 8.5: Calculated QE, with and without ITO absorption

Calculated $QE = 1 - R - T - a_{\mathrm{AR}}$ for device 105868-14-6, without (top) and with (bottom) ITO absorption. Show are also $1 - R$ and $1 - R - T$. The measured thicknesses for the deposited layers were used in this calculation. The measured QE and one minus the reflectivity are shown gray in the background for comparison. The systematics caused by contamination are not included in the errorbands of the QE measurement for clarity.

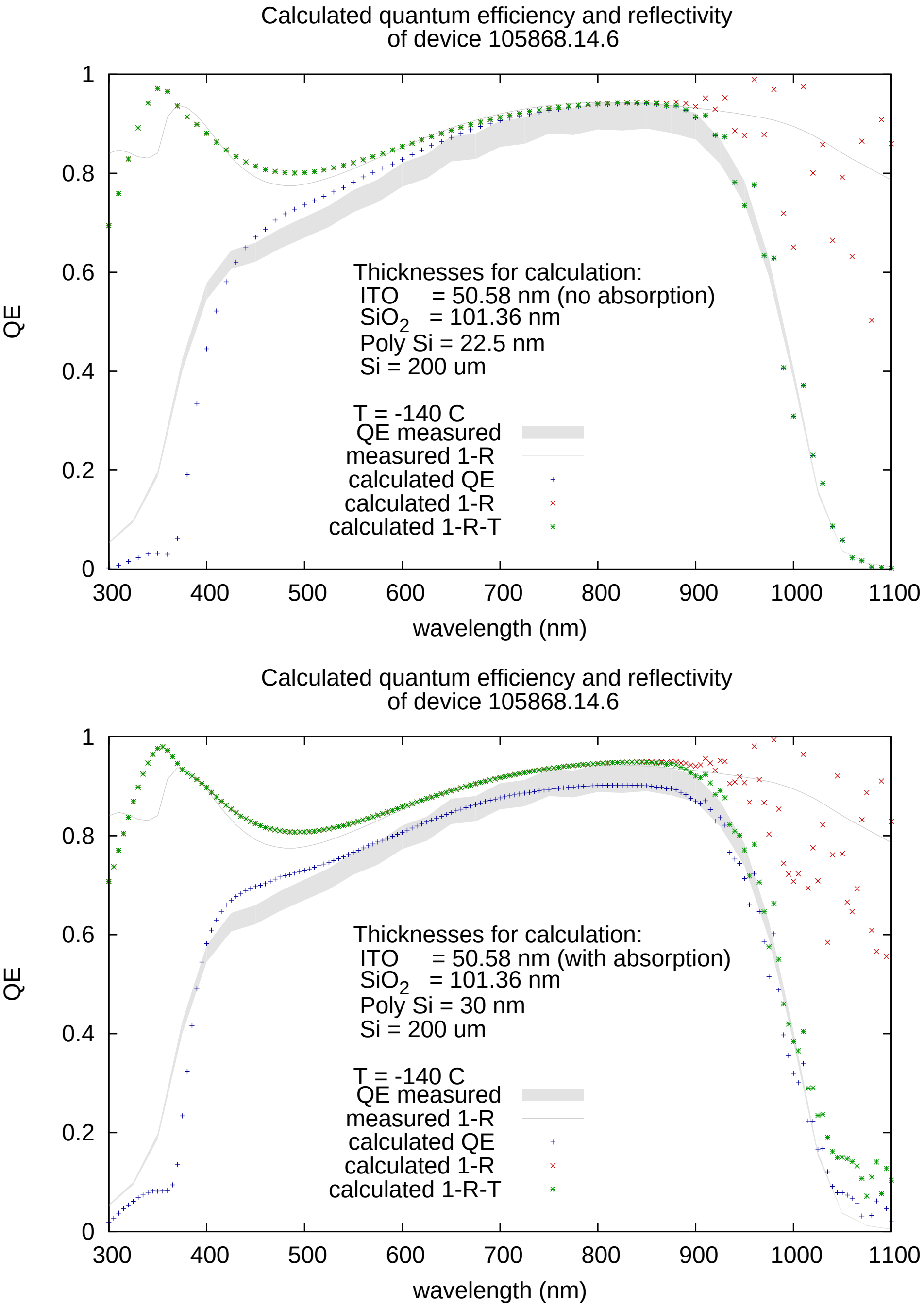

Figure 8.6: Calculated QE for best fit, with and without ITO absorption

The thicknesses of the SiO_2 and the ITO layers were fitted such that the calculation reproduced the calculated reflectivity. Shown are $QE = 1 - R - T - a_{\mathrm{AR}}$, $1 - R$ and $1 - R - T$ for the resulting hypothetical device, with (top) and without (bottom) ITO absorption. The measured QE and reflectivity are shown gray in the background for comparison.

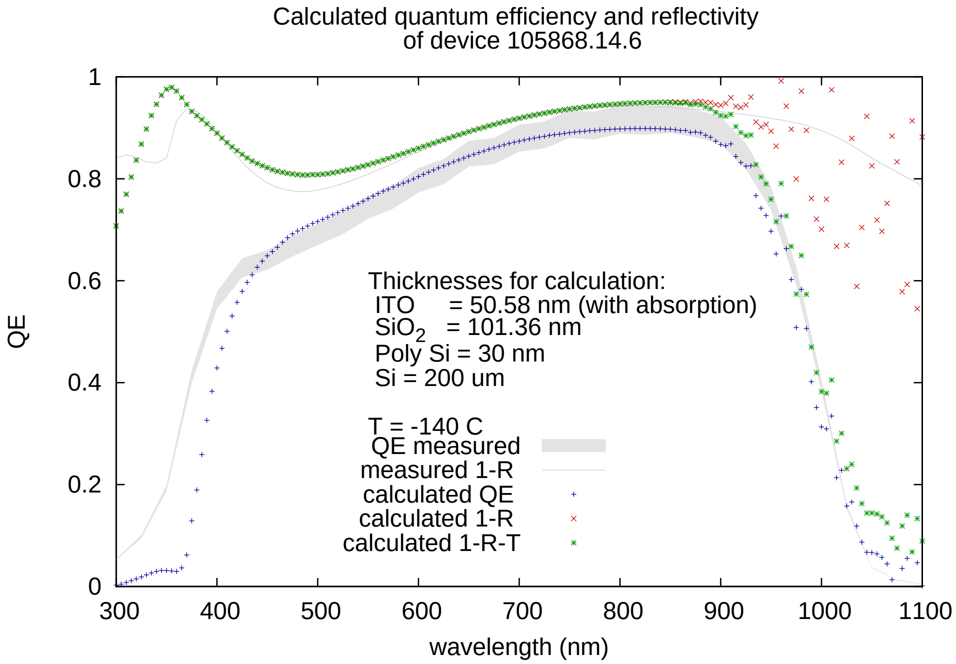

Figure 8.7: Calculated QE for device 105868-14-6, fitted with ITO absorption Calculated QE for device 105868-14-6, still using the fitted thicknesses for the SiO_2 and the ITO layers, this QE and reflectivity calculation now used an increased thickness (30 nm) for the poly silicon layer.

the layers and in the actual datasets for the refractive indices used in the calculation. But with the absorption in the ITO layer we believe to have found the reason for the disagreement between $1 - R$ and the QE we see in the measurements. Also the calculation points to the possibility of an underestimate of the thickness of the poly silicon layer. Alternatively photogenerated charge might also get lost at the surface because of the diffusion of dopants into bulk material. The remaining too low calculated quantum efficiency below 400 nm is possibly due to the too conservative assumption that all charge generated in the polysilicon layer is lost.

8.3 X ray identification

The new algorithm was tested on several devices. Here two, the device 105868-14-6 and the 13 MeV proton irradiated device 105868-15-10 are shown (see Fig. 8.8 and 8.9). The proton irradiation was part of a different experiment which tested the tolerance of SNAP devices towards radiation in space like solar flares and cosmic radiation. Radiation damages decrease the CTE and increase the dark current.

Here, both algorithms show comparable weak dependence of the outcome on the chosen threshold value. The new flagging improved the dependace on the chosen region of interest. The original algorithm often gives a different result for the average signal per x ray event. Tests on synthetic images showed that the background substraction is most likely to be blamed. The background signal level was determined through a gauss fit and subtracted from the whole image. Errors in the background level therefore systematically affected the whole image. The new algorithm tries to avoid such systematic by calculating the background level for each event separately. During earlier tests on synthetic images with artificial background drifts and oscillations the new algorithm showed good stability (see Fig. 6.3).

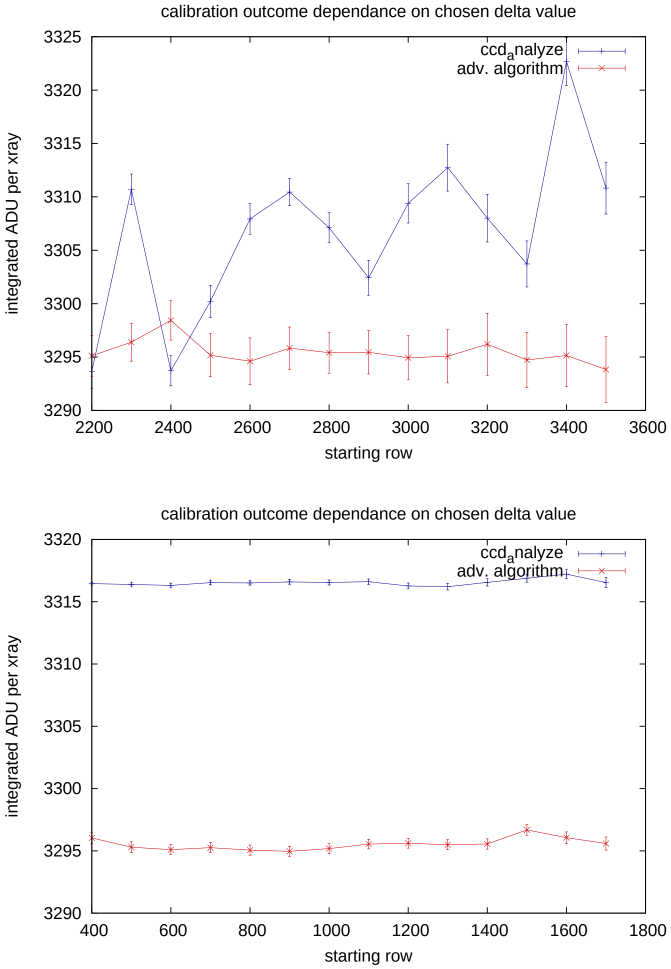

Figure 8.8: Shows the dependence of the outcome for the x ray signal integration on the chosen region of interest.
The CCD 105868.14.6 for exposed to ^{55}Fe x rays.

top) Both the classical and the new algorithm were used to calculate the average signal per x ray for a number of different regions of interest. The region was 900 pixel high and 400 pixel wide. The x-axis shows the start column for the 400 wide area. The new algorithm shows better stability. And a systematically lower signal.

bottom) Now different delta values were tested for for algorithms. A region of interest which was again 900 pixel high but 1800 pixel wide was chosen. The original algorithm shows slightly better stability but a generally higher signal.

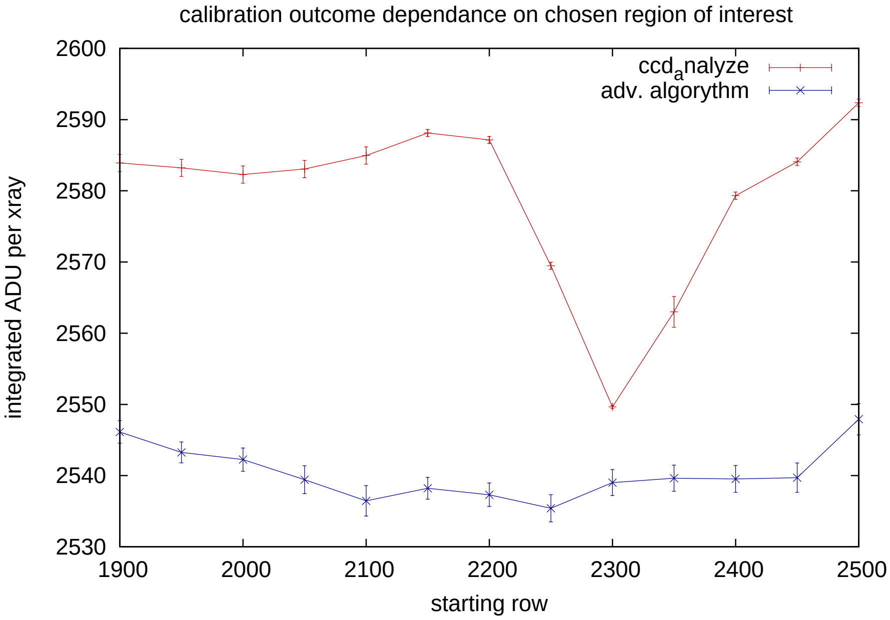

Figure 8.9: Shows the dependence of the outcome for the x ray signal integration on the chosen region of interest.

The previously proton irradiated CCD 105868.15.10 was exposed to ^{55}Fe x rays. Again both algorithms were used to calculate the average signal per x ray for a number of different regions of interest. The region was 1800 pixel high and 1100 pixel wide. The x-axis shows the start column for the 1100 wide area. As for device 105868-14-6 the new algorithm shows better stability. And a systematically lower signal.

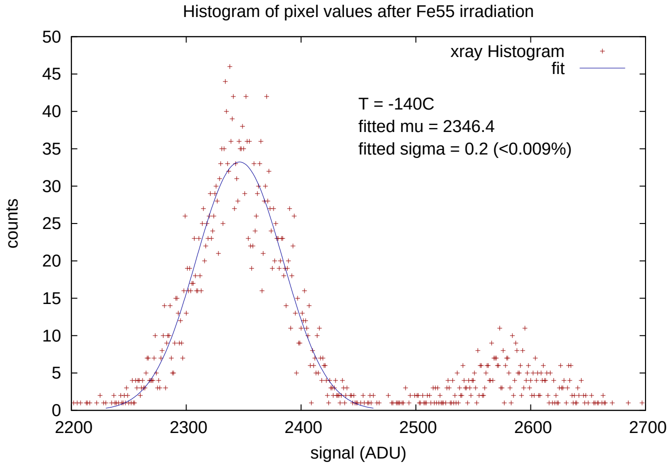

Figure 8.10: The improved x ray identification algorithm was used to generate this histogram for a ^{55}Fe CCD image. Shown are the K_α peak K_β peak. A Gaussian fit to the K_α peak gives a signal of 2346.4 ± 0.2 ($<$ 0.009%) ADU per x ray.

8.4 Fast photon transfer curves

Figure 8.10 shows the result of a ^{55}Fe irradiation of device 105868.14.6 for one quadrant. The K_α and the K_β peak are visible in this histogram. A Gaussian fit to the K_α peak gives a signal of 2346.4 ± 0.2 ($<$ 0.009%) ADU per ray. Even though the the error seems extremely small, the uncertainty in the number of generated electrons per x ray of 1570±17 at -140°C results in a ~1% error for the gain estimate.

Figure 8.11 shows a fast photon transfer curve for device 105868.14.6. A region without any visible artifacts like hot or blocked columns was manually selected.

The signal variance of one row, shows the expected linear dependence of the mean signal. At about 65.000 ADU the ADC saturates and the variance drops to zero. A linear function was fitted to the curve. The high signal region (S $>$ 50000 ADU) was not included in order to minimize fixed pattern effects. The fit gives a gain of 1.4785 ± 0.0034 ($<$ 0.24%) ADU/e^-.

We have now a gain estimate with an uncertainty of about a quarter percent in hand for our QE measurement. This, on the other hand, allows us to estimate a electron-hole pair generation of 1587 ± 4 electons per x ray which is in agreement with [17].

This method allows to measure the electron-hole pair generation as a function of temperature. Such an attempt was made. The data had to be rejected due to problems with the temperature stabilization though.

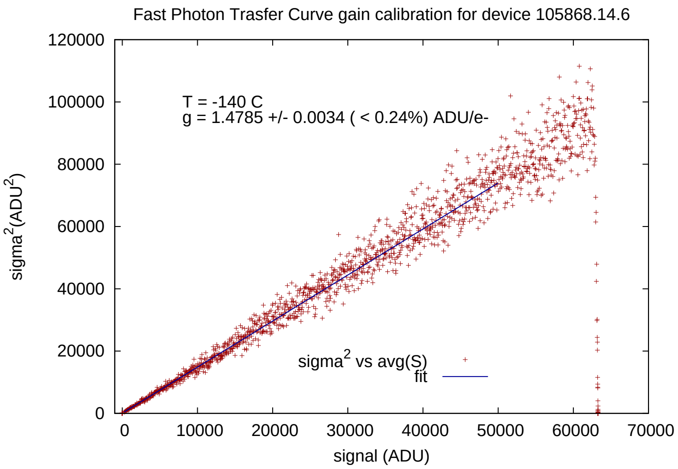

Figure 8.11: Shows the fast photon transfer curve that was calculated from a gradient image. The system gain can be estimated by fitting a linear function to this curve.

8.5 Quantum Efficiency

8.5.1 Round robin device

We received the CCD in a metal box. Three connetctors at the side of the box called "RD", "SS" and "CHAS" allowed to connect the CCD to an amperemeter (see Fig. 8.12). Several modifications to our usual QE setup were necessary to accompany this measurement: The dewar was removed from the blackbox. The hole in the blackbox was closed off. Our calibrated photodiode was taken out of the dewar and placed next to the CCD. Precision square hole masks (9mm x 9mm) were placed in front of the photodiode and the CCD (see Fig.8.13). The CCD and the photodiode were aligned using a laser so that their surfaces were orthogonal to the light path. Our standard script for QE measurements was changed to perform the photodiode mode measurement.

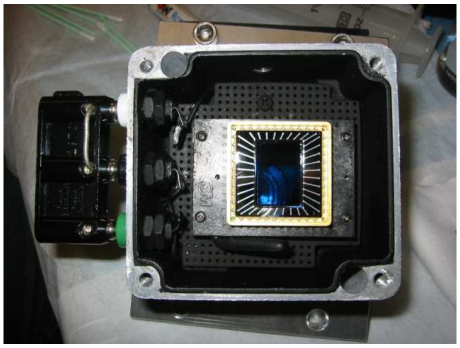

Figure 8.12: The Round Robin CCD in it's box.

Figure 8.13: A 9 mm x 9 mm mask which was placed in front of the CCD. The remainder of the CCD was masked with black tape. The CCD and the photodiode were mounted next to each other close to the back wall of the dark box.

Even though this was not actually considered to be a part of the round robin measurement we also measured the reflectivity for the round robin device. The measured quantum efficiency and one minus reflectivity show excellent agreement from 375 nm to 600 nm (see Fig. 8.14). Below this range we can not claim to be accurate with our reflectivity measurement since the optical fiber we use to connect the reflectometer to the monochromator starts to loose transmittancy. Above 600 nm the QE drops below $1 - R$. This was expected since the round robin device is a thinned device. Our knowledge about the device is intentionally limited but we do know that it is a thinned backside illuminated device as used in astronomy. From the fringes seen in the infrared in the reflectivity data we determine a thickness of about 15 μm .

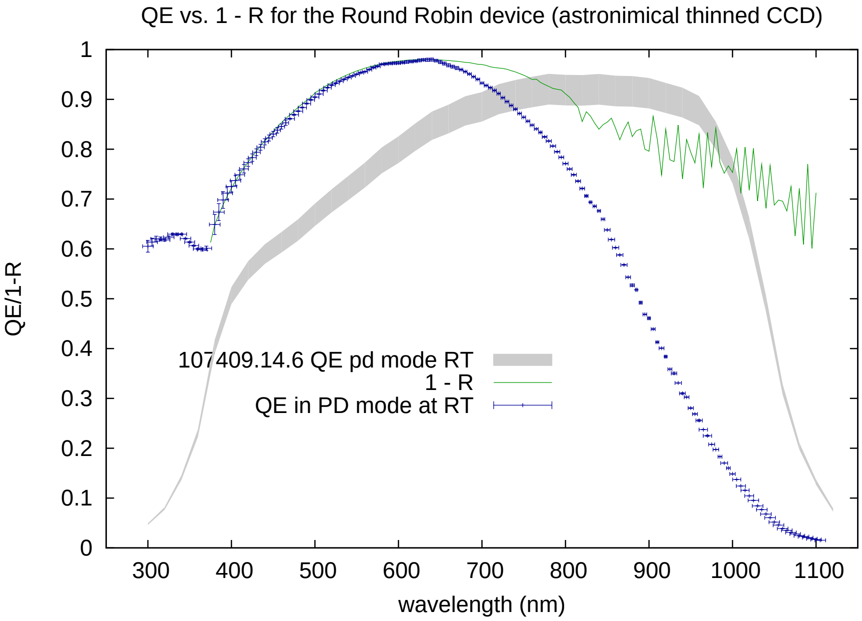

Figure 8.14: Shows the photodiode mode quantum efficiency for the *Round Robin* device. The measured quantum efficiency is in very good agreement with 1-R from 375 nm to 650 nm.

Out knowledge about the *Round Robin Device* is intentionally limited. Certainly it is a thinned, backside illuminated device as often used in astronomy. Rather remarkable is the 98% QE at 630 nm. Above 650 nm the thin device starts to become transparent.

Oscillations in the reflectivity measurement are due to fringing in the CCD. The reflectivity is measured for a 1 mm spot whereas the photodiode mode QE measurement integrates over a 9 mm × 9 mm area (the mask). Which is probably the reason why the QE measurement does not see the oscillations.

The quantum efficiency and $1 - R$ for the device 107409-14-6 for comparison. the thicker device shows a increased quantum efficiency in the infrared.

Parameters:

Temperature: +23° C

Substrate voltage: 0 V

8.5.2 Device 86135-7-7

Device number 86137-7-7 was the very first device tested. It is a thick backside illuminated device without the high voltage modifications. We did not achieve stable results for the quantum efficiency. Only one of the QE curves shows a reasonable agreement with one minus reflectivity. As typical for a contamination, we observed an increase of the QE at the blue end and decrease at the red end (see Fig. 8.15).

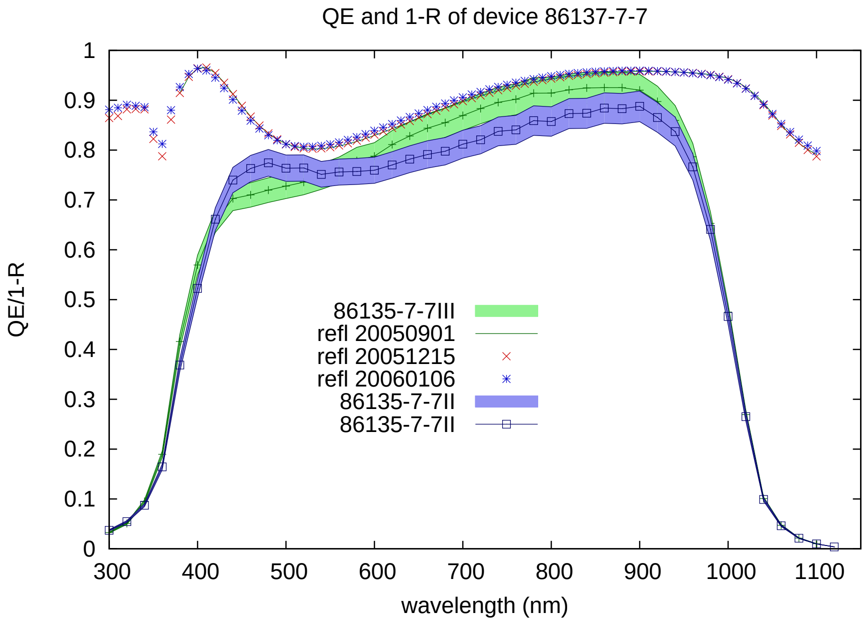

Figure 8.15: Device 86137-7-7 is a thick backside illuminated device but does not have high voltage modifications (Fig. 5.8 shows the device being mounted in the reflectometer.). Tho quantum efficiency scans show a disagreement most likely due to a contamination. The errorbands do not contain systematics due to contamination. Shown also are three measurements of the reflectivity. They are in good agreement.

Parameters:

Temperature: -140° C

Substrate voltage: 20 V

8.5.3 Device 105868.13.6

Device 105868.13.6 was the first high voltage SNAP V2 device tested in the QE setup. We took a large number of QE measurements most of which did not agree with each other (see Fig. 8.16). These measurements pointed us to the problem of contaminations of our CCDs.

Photodiode mode measurements at room temperature did give reproducible results. They show the increase of quantum efficiency in the infrared due to the bandgap shift (see Fig. 8.17).

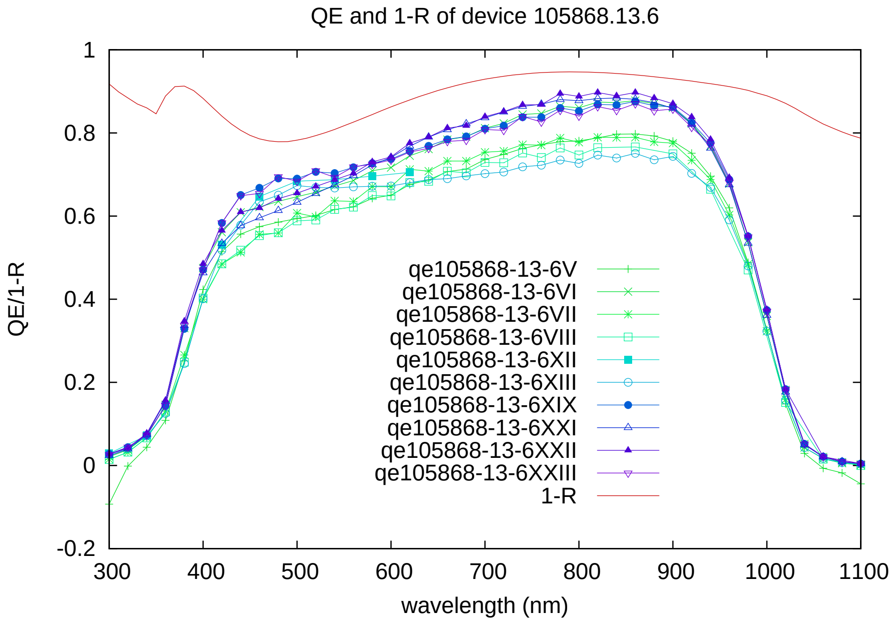

Figure 8.16: 1-R and the results of the first QE measurements for device 105868.13.6. The strong variations in the QE measurements are due to contaminations of the CCD.

Parameters:
Temperature: -140° C
Substrate voltage: 55 V

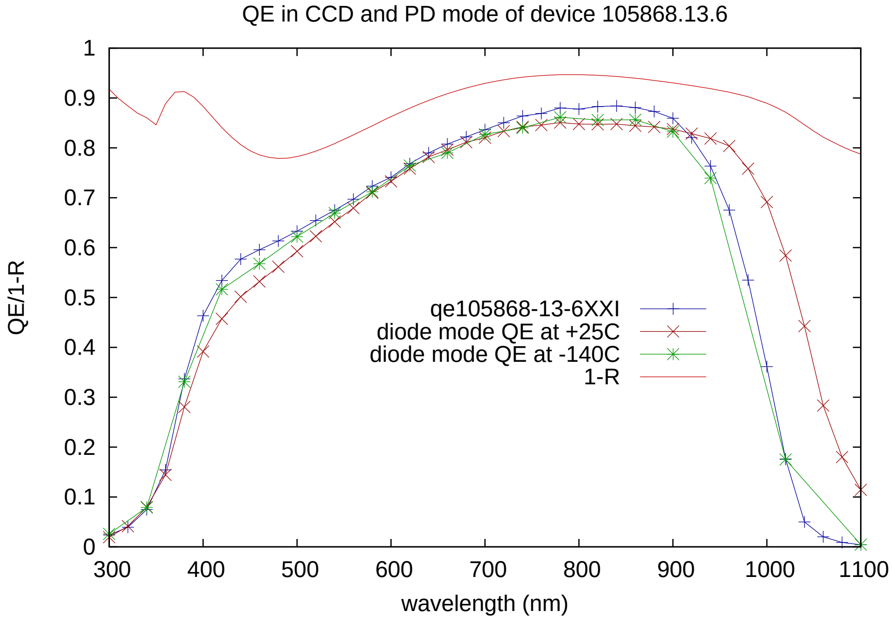

Figure 8.17: The QE measured in photodiode mode shows the typical temperature dependence in the infrared.
The *best* CCD mode measurement and the photodiode mode measurement at -140°C seem to point at an increase in the QE in the blue for lower temperatures. We saw a similar result for device 107409.14.6.
The agreement with 1-R is fairly poor in all cases, probably due to a lack of the not yet implemented masking.

Parameters:
Substrate voltage: 55 V

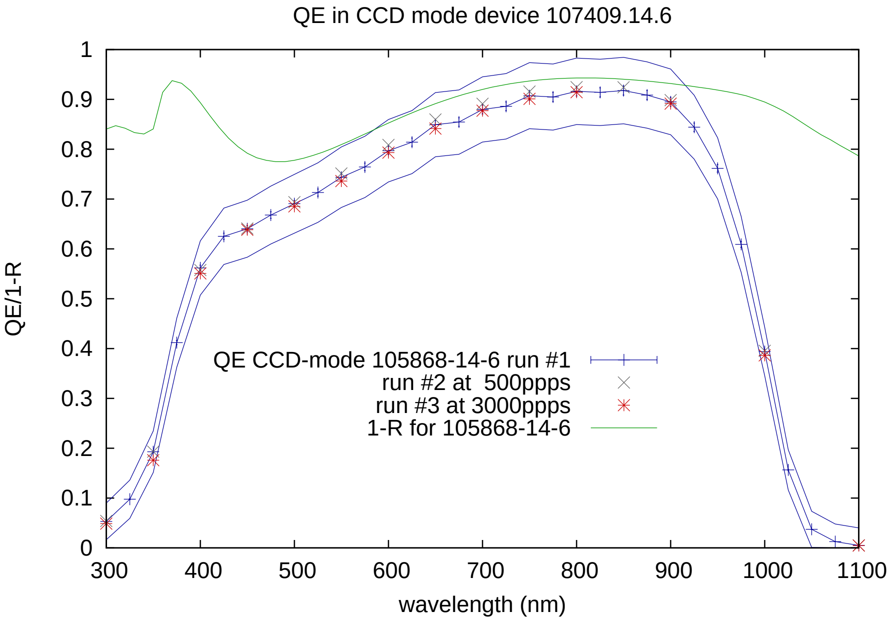

Figure 8.18: CCD mode quantum efficiency scans from device 105868-14-6. Decreasing the scan time and thermocycling produced repeatable results.
The quantum efficieny for this device was measured three times. Each time the dewar was warm to room temperature and then cooled back to the operating temperature. Before each measurement the CCD was thermocycled. Measurement # 2 and # 3 were also take at different light levels (300 photons/pixel/sec. and 3000 photons/pixel/sec.).

Parameters:
Temperature: -140° C
Substrate voltage: 30V V

8.5.4 Device 105868.14.6

After decreasing the scan time we took three sequential QE measurements of the backside illuminated SNAP V2 type CCD 105868-14-6. Before each measurement the CCD was thermocycled, i.e. first cooled to its operating temperature, the warmed up and cooled down again. The three measurements show good agreement suggesting that the method of thermocycling before the measurement and decreasing the scan time produces repeatable results.

Two photodiode mode scans at room temperature were taken (see Fig. 8.19). The room temperature measurement allowed to remove the dewar window and to perform one of the scans in ambient air. Purpose for this measurement was to see how much the backreflection from the dewar window would affect our measurements (see Sec. 4.3.6). The measurement without the window shows more jitter. The temperature stabilization in ambient air is more difficult. The dark current is highly

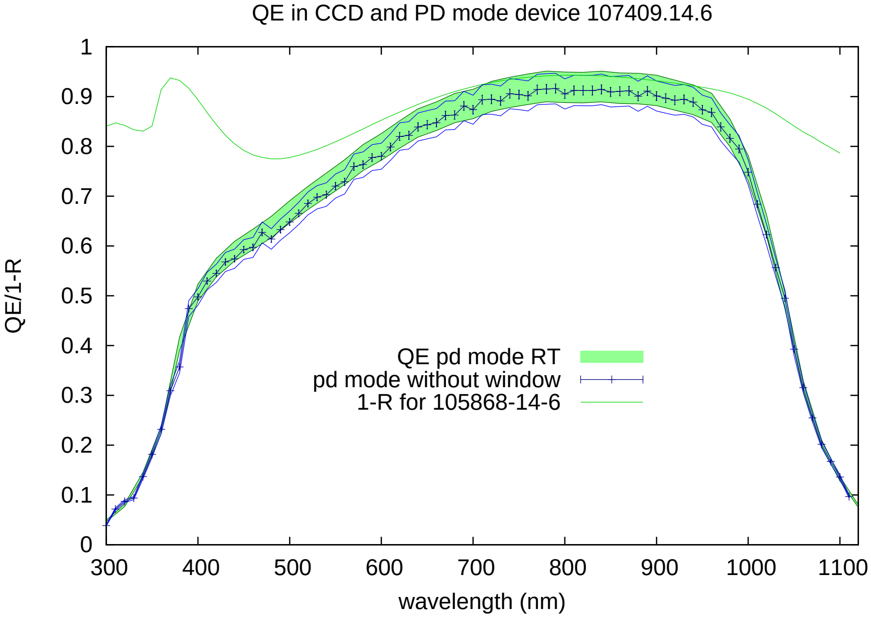

Figure 8.19: The room temperature photodiode mode scans with and without window show good agreement suggesting a small impact of backreflections on the QE data.

Parameters:

Temperature: +23° C

Substrate voltage: 40 V

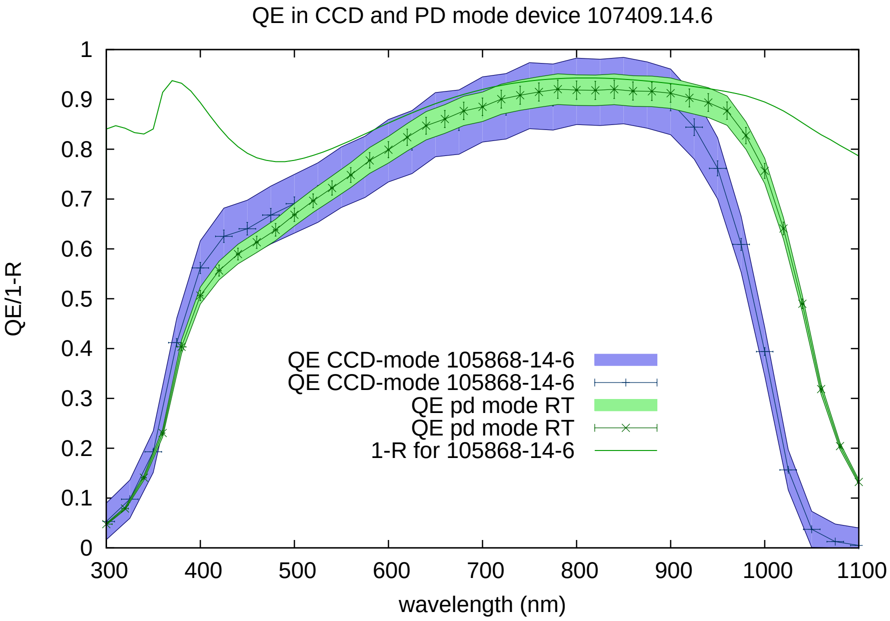

Figure 8.20: Quantum efficiency of the backside illuminated SNAP V2 CCD at 200 V substrate voltage. One minus the reflectivity and the photodiode mode room temperature measurement are shown for comparison.

dependant of the temperature of the CCD. Small temperature drifts cause drifts in the darkcurrent which are seen as jitter. Still both curve agree within their quoted systematic errorbands.

Device 105868-14-6 also was the first device we measured the quantum efficiency for while operating the device with a substrate voltage of 200 V at -140°C (see Fig. 8.20). The room temperature quantum efficiency measured with 30 V substrate voltage and one minus the reflectivity are shown in the also for comparison. Tests for different substrate voltages did not show any significant dependence of the quantum efficiency on the substrate voltage. Both QE curves are in good agreement with exception of the expected change in QE above about 900 nm due to the temperature shift of the bandgap. There is a disagreement between the measured reflectivity and the quatum efficiency. Where 1 - R barely agrees with the measured QE from 650 nm to 900 nm, the disagreement becomes significant below that range. The QE is expected to drop below 1 - R in the blue because of the absorption in the backside coatings. This is not expected to happen much earlier than at 400 nm though. Our results from attempting to improve the QE calculations described in chapter 3 and presented in section 8.2 suggest that this might be explainable by the absorption in the ITO layer and an increased thickness of the poly silicon layer.

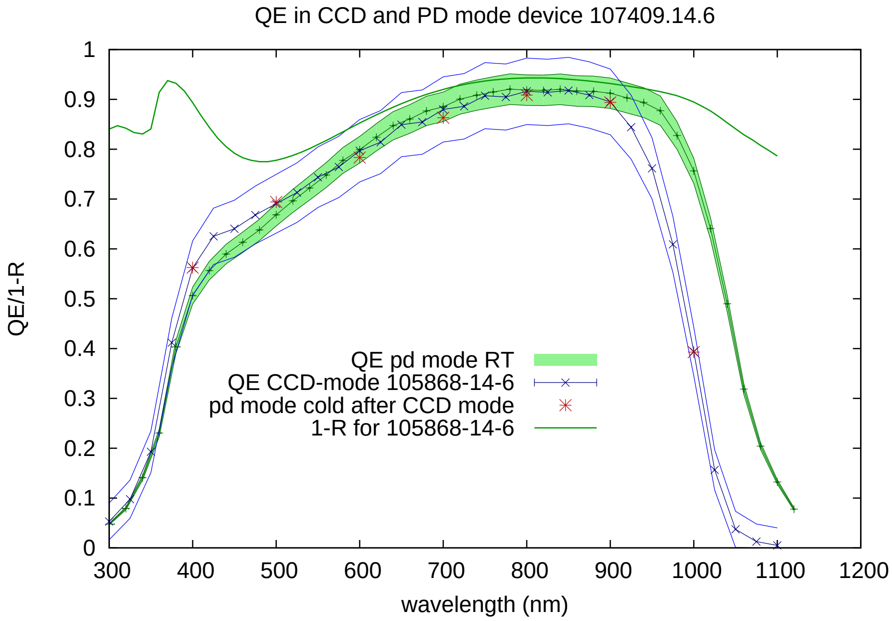

Figure 8.21: Compares the photodiode mode measurements at room temperature and at -140° C and the CCD mode measurement at -140° C. The cold photodiode mode measurement reproduces the CCD mode curve.

Figure 8.21 compares results from a photodiode mode scan at room temperature, the QE measured in photodiode mode for seven different wavelengths at -140°C and the 200 V CCD mode scan. The cold photodiode mode measurement reproduces the CCD mode QE well, suggesting that this measurement is a valid method for verification of the classical method.

From 400 nm to 500 nm both cold scans show disagreement with the room temperature scan. Traces of such a disagreement were also seen in the data for device 86135-7-7. This effect is not understood yet.

Of course the room temperature photodiode mode measurement avoids the problems of contaminations completely. With the fast QE measurement and the photodiode mode measurement we believe to have implemented two techniques to measure the quantum efficiency accurately.

8.5.5 Device 107409.14.7

Radiation damage impact on QE

In a different experiment the frontside illuminated SNAP V2 device 107409.14.7 was exposed to 13 MeV protons at the LBNL 88 inch cyclotron. Since front side illuminated, this particular device was not thinned.

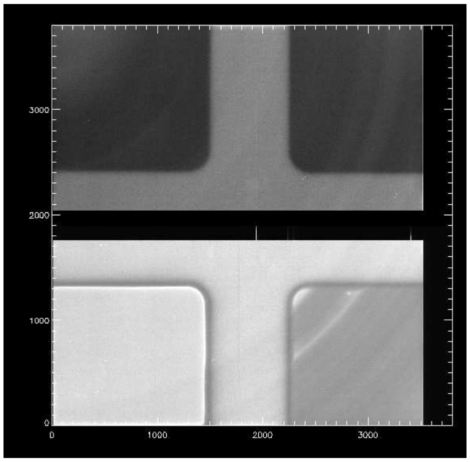

Figure 8.22: Flat field image for the frontside illuminated 650μm thick device 107409.14.7 after irradiation with four different doses.
The corner regions of the device were exposed four different doses
upper right) 5×10^9 p/cm^2
upper left) 1×10^{10} p/cm^2
bottom right) 5×10^{10} p/cm^2
bottom left) 1×10^{11} p/cm^2
. The crossshaped region in the center was masked off and not exposed to protons. The black band in the center is the overscan region and an artifact of the read out.
The lower left region with the highest radiation seems to be least affected. This is a startling result.
Parameters:
Temperature: -140° C
Substrate voltage: 80 V

The four corners of the device were irradiated with four different doses of protons. The post radiation test showed a decrease of QE in the infrared. A flat image (see Fig. 8.22) which was taken for a wavelength of 1050 nm shows a lower signal in three of the four irradiated quadrants. The quantum efficiency of the region with the highest radiation dose seemed to be least affected. To examine this somewhat surprising result we measured the quantum efficiency of the device. The QE scan verified the QE drop in the infrared (see 8.23).

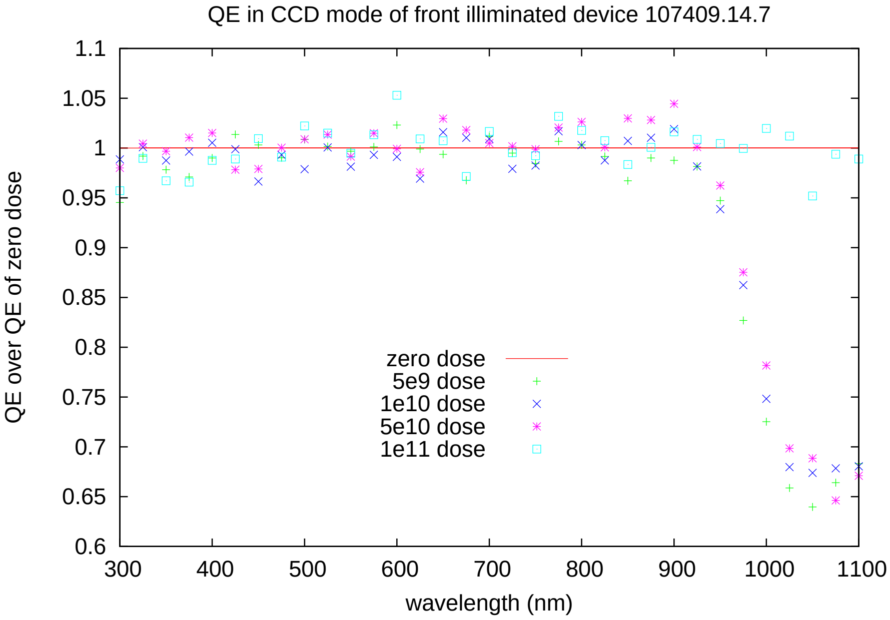

Figure 8.23: Device 107409.14.7 is a SNAP V2 device mounted for frontside illumination. The four corners of the device were irradiated with four different doses 13 MeV protons. The relative QE for the four different doses of radiation vs. the QE of the zero dose is shown here.
Up to 900 nm there is no significant change in quatum efficiency. Then a sudden drop in th QE is observed of all but the highest dose.

Parameters:
Temperature: -140° C
Substrate voltage: 80 V

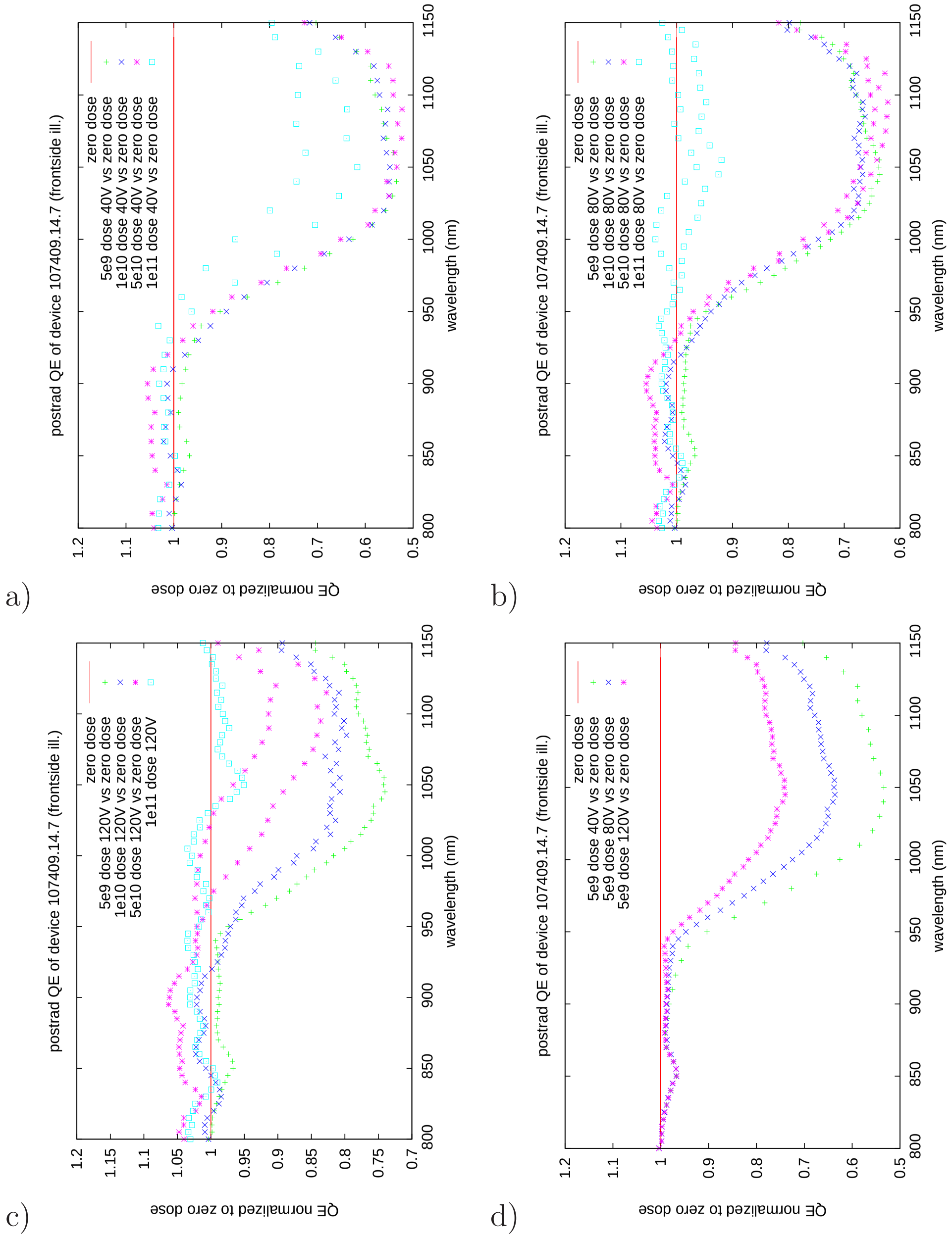

Figure 8.24: Higher resolution scans of the QE for the irradiated device 107409.14.7 far taken. The quantum efficiency proved to be a function of the substrate voltage.
a) QE scan for 40V substrate voltage. All four doses show a decrease in quatum efficiency. The highest dose performs slightly better. The QE of the highest dose seems to change over time. The two lines are a result of the double sweep interlaced scan and a QE drift between the two scans. **b)** QE scan for 80V substrate voltage. The QE for the highest dose is almost restored. It still drifts. **c)** QE scan for 120V substrate voltage. The QE for the highest dose is restored and shows no drift over time. The QE for the lower doses improved. Now the $5 \times 10^{10} \frac{\text{protons}}{cm^2}$ shows a drift. **d)** QE scans for the lowest $5 \times 10^{9} \frac{\text{protons}}{cm^2}$ at three different substrate voltages shows the curing of QE by increase substrate voltage.

All scans were taken at -140 C.

Higher resolution scans at different substrate voltages revealed a curing effect by the increase of the substrate voltage (see Fig. 8.24). This suggests that the depletion depth is affected by the radiation. So far it is unclear, why the QE of the areas with the lowest dose seems to be affected worst.

Front illumination

The 13 MeV proton irradiated device 107409.14.7 is a SNAP V2 device mounted for frontside illumination. Light enters the the silicon through the gate structure. The gate structure partly reflects and partly absorbs light resulting in a loss of quatum efficiency vs. backside illumination. Four corners of the device were exposed to four different doses of radiation. A cross shaped region in the center (see Fig. 8.22) was masked off during the irradiation. Figure 8.25 shows a QE scan of this region and demonstrates why astronomical CCDs are backside illuminated.

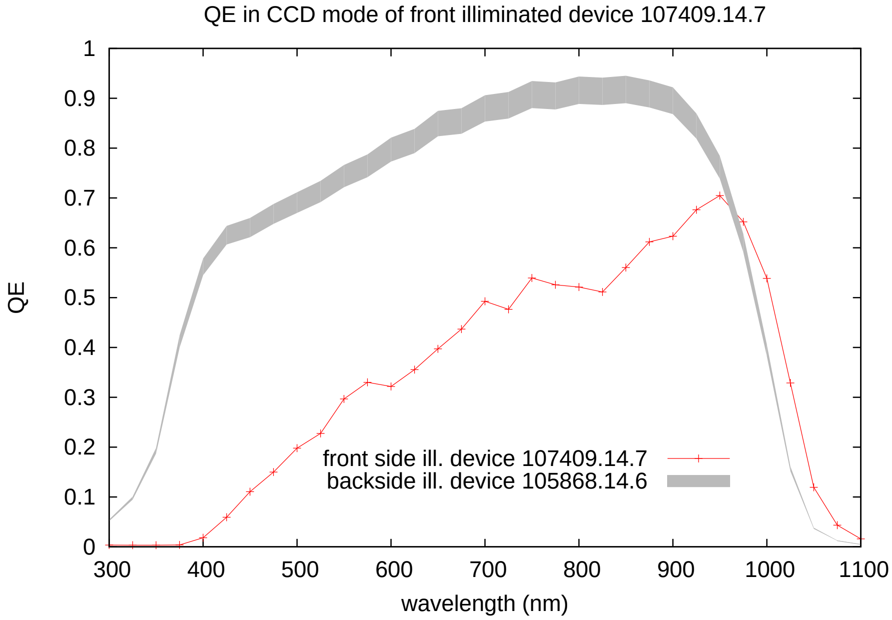

Figure 8.25: Device 107409.14.7 is a SNAP V2 device mounted for frontside illumination. The four corners of the device were irradiated with four different doses 13 MeV protons. Here the QE of the zero dose region between the irradiated parts is plotted over the QE of the backside illuminated device 105868.14.6. Due to the high reflectivity of the front side illuminated device a large amount of light is reflected back and forth between the CCD's surface and the dewar window. Therefore large errors should be attached to the QE plot here. The higher QE estimate for the frontside illuminated device vs. the backside illuminated device at the red cutoff is certainly a effect of backreflection.
The accurate measurement of the absolute QE has not been the purpose of this measurement. We actually intended to examine a change in the QE due to the irradiation.
This plot give a nice impression though, how much the QE is decreased by the gate structure on the front side and why one want to use backside illuminated devices. The loss in QE increases with the decrease of wavelength. For shorter wavelengths also the penetration depth is shorter.

Parameters:
Temperature: -140° C
Substrate voltage: 80 V

8.5.6 Device 81481-23-24

Device 81481-23-24 is a backside illuminated thick LBNL CCD. It is a 2048 × 4096 15.0 μm pixel CCD. The number of cosmetic defects in the device was so low that is considered to be a science grade device which may replace the current CCD in the red arm of the SNIFS (SuperNova Integral Field Spectrometer) on the Mount Palomar, Hawaii. Figure 8.26 shows the quantum efficiency scan for this device. The CCD needed to be mounted in a different dewar due to its different physical dimensions. This dewar was also a Infrared Labs ND-8 device but it was not equipped with a calibrated photodiode. We therefore used the previously crosscalibrated sphere diode for the QE measurement. The three measurements show variations in the QE due to contaminations which grow on the cold device. By the time we took these data we did not operate in the fast scan mode yet. From our later developed knowledge we believe the blue curve to be the most accurate one.

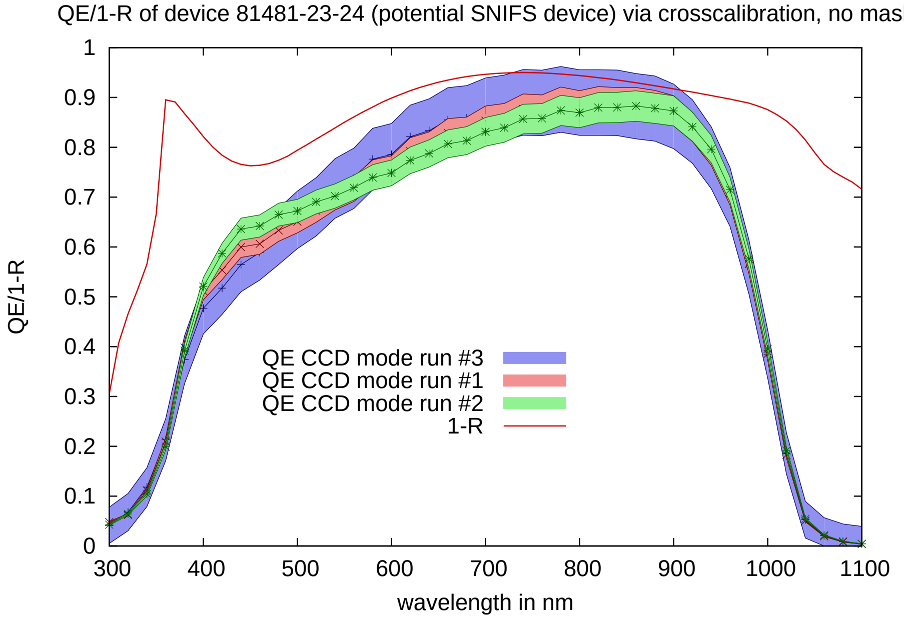

Figure 8.26: Quantum efficiency scans for device 81481-23-24. Variations in the quantum efficiency are due to contaminations. Only the errorband the curve for run # 3 contains the contamination.

Parameters:
Temperature: -140° C
Substrate voltage: 40 V

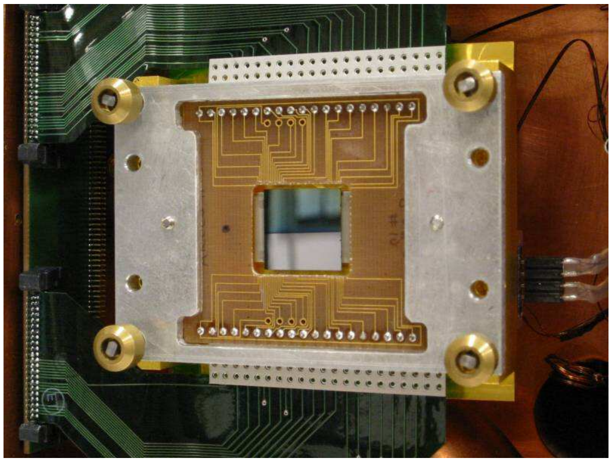

Figure 8.27: The backside ohmic contact was formed molecular beam epitaxy The process grows a thin layer of Sb-doped silicon on the backside. For testing reasons only about half (upper half) of the device has an antireflective coating.

8.5.7 JPL device delta doped 75091-14-9

Figure 8.27 shows a photograph of the device 75091-14-9. The backside ohmic contact was formed molecular beam epitaxy at the Jet Propulsion Laboratory. The process grows a thin layer of Sb-doped silicon on the backside. This is a low temperature step of 450° C which allows to finish the Al interconnects before thinning. The thinner contact layer is expected to increase th UV sensitivity. Only about half of the device is coated with an antireflective layer.

The quantum efficiency and one minus reflectivity for the coated and the uncoated areas of the JPL delta doped CCD were measured (see Fig. 8.28) . A lack of masking of the the mounting frame of the JPL CCD resulted in a measured QE which exceeds 1-R. We scaled the measured QE to match 1-R in the red since we expect a match there. These curves are only of qualitative character. But they point towards and increase of QE in the blue.

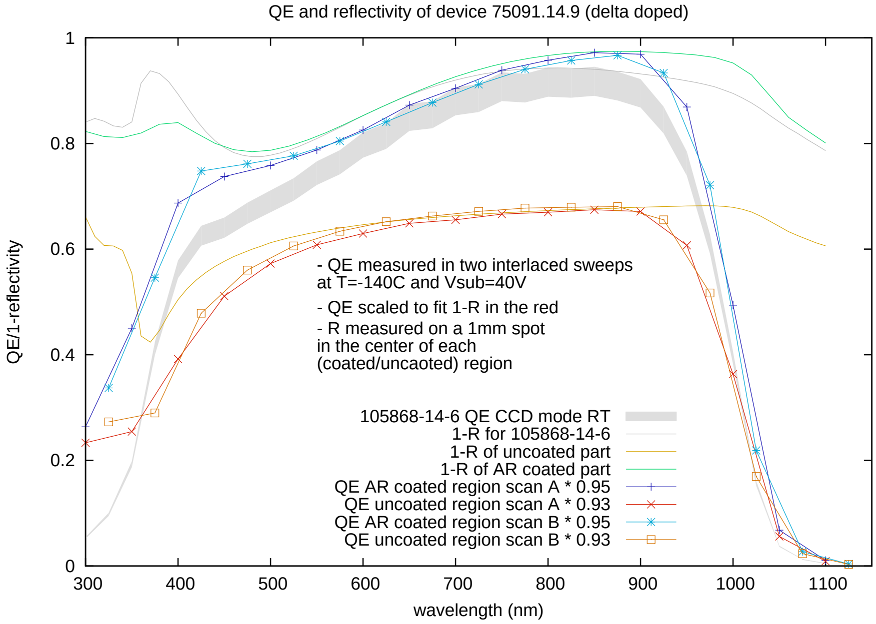

Figure 8.28: Shows the quantum efficiency and one minus reflectivity for the coated and the uncoated areas of the JPL delta doped CCD.
The grey curves in the background show the QE and one minus reflectivity for the CCD 105868-.14.6 for comparison.
QE was scaled to fit $1 - R$ in the red.

Parameters:
Temperature: -140° C
Substrate voltage: 40 V

CHAPTER 9
CONCLUSION

Purpose of this work was the careful examination of the systematics in the LBNL setup for quantum efficiency (QE) measurements of (Charge-Coupled Devices) CCDs and the implementation of techniques to verify the QE data. The already existing prototypal setup was further modified to decrease uncertainties. Methods and algorithms for the automation of the measurement and the analysis of the resulting data were developed.

The most important uncertainty is caused by contaminations of the CCD in the vacuum. The cold (-140°C) detector becomes an effective getter for residual substances in the dewar. If the QE is measured directly after cooling the detector to its operating temperature, contaminations cause a 3.5% absolute uncertainty for a 25 nm resolution scan. If the resolution is decreased to 50 nm, the uncertainty is decreased to 1.5% as a result of the shorter scan which gives the contaminations less time to build up. Future efforts might look into techniques like plasma cleaning of the dewar as suggested by other groups.

After the contaminations the gain calibration introduces the second most significant error of 1.5% (relative). Improvements in the x ray identification algorithm may decrease this figure to one percent. The remaining one percent is a consequence of the uncertainty in the number of generated electron-hole pairs per absorbed 5.90 keV x ray photon at -140°C. The Fast Photon Transfer Method does not rely on the use of an x ray source but on photon statistics. Different than the classic photon transfer curve it only uses one gradient image rather than a large number of images with different signal level. We successfully implemented this technique and reached 0.2% uncertainty in the gain calibration for high quality devices. This method would allow to actually measure the number of electron-hole pair generation as a function of temperature.

Reflection of light off the CCD's surface onto the dewar window and back to the CCD may cause systematics in order of 1% . After an attempt to measure the effect we do believe that this number is somewhat pessimistic but a direct measurement of the magnitude is difficult. A future setup might tilt the dewar window in order to eliminate this effect.

Inspired by the Round Robin test, we implemented the photodiode mode measurement to verify the QE data. Since it directly measures the photocurrent at the reset drain of the CCD, it allows a QE determination without prior gain calibration. We showed that the photodiode mode measurement also allows a QE measurement at room temperature despite of the high dark current which is a result of the biasing of the LBNL devices. We did see a slight increase of the quantum efficiency in the blue at room temperature which is not yet fully understood. Still the room temperature measurement eliminates the contamination problematics completely and allow an estimate with a 3.35% relative, systematic uncertainty. Also the roomtemperature measurement provides a higher test thoughput and shows the possibility of a wafer level QE test. Finally it allowed us to prove us though pre- and post- cooling tests that the contaminations evaporate completely once the CCD is warmed up back to room temperature.

To further verify the QE data we designed and implemented an unconventional reflectometer. Contrary to other systems, it measures the reflectivity with only one reflection off the CCD's surface which is favorable due to the low reflectivity of astronomical CCDs. After the setup, the reflectivity measurement is done fully automated, allowing for a convenient test before each QE measurement.

The fully depleted backside illuminated SNAP CCD does show increased sensitivity in the infrared. For the 200 μm thick device 105868.14.6 we measured a peak quantum efficiency of 91.7% ±6.7% (sys.) ±0.1% (stat.) at 850 nm and still 39.4% ±4.9% (sys.) ± <0.1% (stat.) quantum efficiency at 1000 nm.

Reflectivity measurements showed an unexpected disagreement between one minus the reflectivity and the quantum efficieny. A reimplemented code to calculate the quantum efficiency from given refractive indices and thicknesses of the used materials showed that the disagreement is probably explicable by absorption in the ITO layer and possibly by an increased thickness of the poly silicon layer. Currently measurements are made of deposited layers of SiO_2 and ITO and a combination of both on glass to further examine this issue.

We participated the Round Robin tests which are conducted by Morley Blouke. One astronomical CCD is shipped to several participants who the measure its QE. The data allow for a comparison of existing setups. Our data show an excellent agreement between one minus the reflectivity and the quantum efficiency. The publication of the Round Robin measurements is pending.

The quatum efficiency of a *delta doped* CCD was tested. The backside ohmic contact for this device was formed using molecular beam epitaxy at the Jet Propulsion Laboratory shows an increased quantum efficieny in the UV.

The last measurements conducted as part of this work addressed the somewhat suprising behavior of a earlier proton irradiated CCD. The device was exposed to 13 MeV to test the sensitivity of SNAP CCDs to high energy radiation in space such as solar flares and cosmic radiation. First results indicate a unexpected change of the depletion depth caused by the radiation.

Even though the problem of contaminations remained, we achieved good repeatability of our QE measurements. Methods like the photodiode mode measurement and the reflectivity measurement back our results. We believe to have identified all systematics of the setup and to have prepared for quantum efficiency measurement future devices.

APPENDIX A
VOODOO MEASUREMENT SCRIPTS

A.1 QE measurement CCD mode

It follows the basic structure of the script:

- Parameter definition.
- Set system to the selected temperature and wait until this temperature is reached.
- Start the lamp.
- Prepare the devices (resetting/zero correction of Keithleys).
- Prepare the CCD, epurge/erase (optional, see appendix D).
- Take two initial x ray and two dark images (optional).
- Now for all selected wavelengths (in double sweep interlaced manner, see Sec. 4.1.7) do:
    - Set the monochromator to the current wavelength.
    - Set the slitwidth according to the slitwidth file or do lightlevel adjustment.
    - Do epurge (optional, see appendix D).
    - Take a x ray and a dark image (optional).
    - Take a dark image and measure the current on both Keithleys.
    - Take a flatfield image and measure the current on both Keithleys.
    - Write current data to the data file.
- And finally turn the lightsource off.
- Take long dark exposures (optional).
- Turn the CCD power off.
- Set CCD temperature controller to predefined value.

The actual script may be obtained from the LBNL SNAP CCD group.

A.2 QE measurement photodiode mode

It follows the basic structure of the script:

- Parameter definition.
- Set system to the selected temperature and wait until this temperature is reached.
- Start the lamp.
- Prepare the devices (resetting/zero correction of Keithleys).
- Now for the number of selected iterations:
  - For all selected wavelengths (in double sweep interlaced manner, see Sec. 4.1.7) do:
    - Set the monochromator to the current wavelength.
    - Set the slitwidth according to the slitwidth file or to light level.
    - For all selected substrate voltages do:
      - Set substrate voltage.
      - Take dark current measurement with both Keithleys.
      - Open the large shutter.
      - Take photocurrent measurement with both Keithleys.
      - Close the large shutter.
      - Take second dark current measurement with both Keithleys.
      - Write current data to the data file.
- And finally turn the lightsource off.
- Take long darks (optional).
- Turn the CCD power off.
- Set CCD temperature controller to predefined value.

APPENDIX B
ERROR OF THE ERROR

If the variance σ^2 or σ is a parameter of a fit, then its error can be evaluated.

The trick is to use the *Ursache* of all statistics, the maximum likelihood:

$$\mathscr{L} = \prod_i \mathscr{P}(\overrightarrow{x}_i, \overrightarrow{a})$$

when the $\overrightarrow{x}_i$ are the experimental quantities for the i-th measurement, and $\overrightarrow{a}$ are the parameters. Find the parameters $\overrightarrow{a}$ which maximize $\mathscr{L}$. More conveniently is the log-likelihood

$$w = \ln(\mathscr{L}) = \sum_i \mathscr{P}(\overrightarrow{x}_i, \overrightarrow{a})$$

which has the same maximum. The solution is to solve

$$\frac{\partial w}{\partial a_i} = 0$$

for the a's. If we are lucky, it's linear. Then in the asymptotic case (or a linear model with Gaussian errors), the inverse covariance matrix is (see Chapter 32 [49])

$$V_{jk}^{-1} = -\frac{\partial^2 w}{\partial a_j \partial a_k} \tag{B.1}$$

it is of the form

$$V^{-1} = \begin{pmatrix} \frac{1}{\sigma_1^2} & \frac{1}{\sigma_1\sigma_2} & \frac{1}{\sigma_1\sigma_2} & \cdots & \\ \frac{1}{\sigma_1\sigma_2} & \frac{1}{\sigma_2^2} & \cdots & & \\ \vdots & \vdots & \frac{1}{\sigma_3^2} & \cdots & \\ & & & \ddots & \\ & & & & \frac{1}{\sigma_n^2} \end{pmatrix}$$

and if we are lucky, to' diagonal, and σ_i^2 is the variance of the i-th parameter.

Example: N measurements from a Gaussian distribution:

$$P_i = \frac{1}{\sqrt{2\pi}a_2} \exp\left(-\frac{(x_i - a_1)^2}{2a_2}\right)$$

where a_1 is the mean and a_2 is the usual σ, ${a_2}^2$ is the variance.

So.

$$\begin{aligned} w &= \sum_i^N (-\ln\sqrt{2\pi} - \ln a_2 - \frac{(x_i - a_1)^2}{2{a_2}^2}) \\ &= -N\ln a_2 - N\ln\sqrt{2\pi} - \sum_i^N \frac{(x_i - a_1)^2}{2{a_2}^2} \\ \frac{\partial w}{\partial a_1} &= \sum_i^N \frac{x_i - a_1}{{a_2}^2} = \frac{\left(\sum_i^N x_i\right) - Na_1}{{a_2}^2} \end{aligned}$$

$$\Rightarrow a_1 = \frac{1}{N}\sum_i^N x_i$$

as expected! And

$$\frac{\partial w}{\partial a_2} = \frac{1}{{a_2}^3}\sum_i^N (x_i - a_1)^2 - \frac{N}{a_2}$$

$$\begin{aligned} \frac{1}{{a_2}^3}\sum_i^N (x_i - a_1)^2 - \frac{N}{a_2} &= 0 \\ \Rightarrow {a_2}^2 &= \frac{1}{N}\sum_i^N (x_i - a_1)^2 \end{aligned}$$

Now the second derivative:

$$\frac{\partial^2 w}{\partial a_1^2} = -\frac{N}{{a_2}^2}$$

Comparing with equation B.1 gives:

$$\Rightarrow \text{variance of } a_1 = \frac{{a_2}^2}{N}$$

$$\frac{\partial^2 w}{\partial {a_2}^2} = -\frac{3}{{a_2}^4}\sum_i^N (x_i - a_1)^2 + \frac{N}{{a_2}^2}$$

$$\text{using } {a_2}^2 = \frac{1}{N}\sum_i^N (x_i - a_1)^2$$

$$\frac{\partial^2 w}{\partial {a_2}^2} = -\frac{3}{{a_2}^2}N + \frac{N}{{a_2}^2} = -\frac{2N}{{a_2}^2}$$

Again, comparing with equation B.1 gives:

$$\Rightarrow \text{variance of } a_2 = \frac{{a_2}^2}{2N}$$

$$\textit{error of } a_2 = \frac{a_2}{\sqrt{2N}}$$

APPENDIX C
IDL ALGORITHMS

C.1 Fast Photon Transfer curves

Short version of the algorithms in used for the analysis of the fast photon tranfer curve images. Parts which write and plot files as well as the hot coloumn rejection algorithm are not shown.

```
; performs two pixel substraction to get rid of low frequency noise
;         if used the fpt algorithm will need (and does) take care
;         about the fact that the noise doubles
;
;         INPUT PARAMETERS:
;                  im        –        image to perform two pixel substraction on
;         RETURNS:
;                  twopixel substrated image array
function twoPixSub, im
          s = size(im)
          ncol = s(1)
          nrow = s(2)

          newim = make_array(ncol – 1, nrow, /L64)

          for i = 0, ncol – 2 do begin
                   newim[i, ∗] = LONG64(im[i, ∗]) – LONG64(im[i + 1, ∗])
          endfor
          return, newim
end

;fast photon transfer curve algorithm
;         INPUT PARAMETERS:
;         im                –        gradient image
;         biasIm            –        bias image (typically unexposed part of the
;                                             gradient image)
;         lowerFitLimit     –        lower limit for the fit range
;         upperFitLimit     –        upper limit for the fit range
;
;         OPTIONAL INPUT:
;         NOTWOPIX          –        turns off usage of the two pixel
;                                             substraction mode
;         NO_PLOT           –        turns off plotting
;
pro fpt, im, biasIm, lowerFitLimit, upperFitLimit, NOTWOPIX = notwopix, $
          ;output

          ;get image dimensions
```

```
s = size(im)
ncol = s(1)
nrow = s(2)
twoPixIm = 0

;if two pixel substraction is enabled, generate the two pixel
;        subtracted image
if ( not keyword_set(notwopix)) then begin
        twoPixIm = twoPixSub( im )
endif

;calculate bias level
bias_mom = moment(biasIm)
bias_mean = bias_mom[0]
print, "Bias mean: ", bias_mean
bias_sigma = sqrt(bias_mom[1])
print, "Bias sigma: ", bias_sigma

;calculate mean signal and sigma for each row
signal = make_array(nrow)
signal_sigma = make_array(nrow)
for i = 0, nrow -1 do begin
        mom = moment( im[*,i] )
        if (keyword_set(notwopix)) then begin
                signal[i] = mom[0] - bias_mean
                signal_sigma[i] = sqrt(mom[1])
        endif else begin
                ;if two pixel substraction is selected,
                ;        get sigma from two pixel subtracted image
                signal[i]          = mom[0] - bias_mean
                momTwoPix          = moment( twoPixIm[*,i] )
                ;sigma^2 has to be divided by two since the
                ;        substraction
                ;        doubles the standard deviation
                signal_sigma[i] = sqrt(momTwoPix[1]/2)
        endelse
endfor

;select the data which are within the fit limits
X_L = signal[where(signal gt lowerFitLimit)]
Y_L = signal_sigma[where(signal gt lowerFitLimit)]
X = X_L[where(X_L lt upperFitLimit)]
Y = Y_L[where(X_L lt upperFitLimit)]
ERR_Y   =        Y/sqrt(1*ncol)

;now we linearize the problem. In the
```

```
        ;           shot noise regime the variance has a liner dependance
        ;           of the signal
        Y_sq = Y^2
        ERR_Y_sq = 2*Y*Y/sqrt(2*ncol)

        ;now, FIT
        r = linfit(X, Y_SQ, PROB=prob, $
                    MEASURE_ERRORS=ERR_Y_sq, SIGMA=sigma, CHISQ=chisq)
        gain = r[1]
        g_sigma = sigma[1]

        print, "fit probability = ", prob
        print, "gain = ", gain, " +/- ", g_sigma, $
                    "(=", g_sigma/gain * 100.0,"%)"
        print, "bias = ", bias_mean, " +/- ", bias_sigma, $
                    "(=",bias_sigma/bias_mean * 100,"%)"
        print, "bias sigma from fit = ", sqrt(r[0]), "+/-", $
                    sqrt(sigma[0]) ,"(=",sqrt(sigma[0]/r[0])*100,"%)"

        ;now plot data, write them to files etc...
end
```

C.2 Improved x ray identification

Short version of the algorithms in used for the analysis of the x ray images. Parts which write and plot files as well as the hot coloumn rejection algorithm are not shown.

```
;label all the pixel in the area distance d around (col,row)
pro label, im, map, xrays, col, row, d, l
        ;range checks
        minCol = col-d
        maxCol = col+d
        minRow = row-d
        maxRow = row+d
        if (minCol lt 0) then minCol = 0
        if (minRow lt 0) then minRow = 0
        s = size(map)
        if (maxCol gt (s[1] -1) ) then maxCol = s[1] -1
        if (maxRow gt (s[2] -1) ) then maxRow = s[2] -1

        ;only event label (>0) can overwrite existing labels
        if (l gt 0) then begin
                subim = im[minCol:maxCol,minRow:maxRow]
                submap = map[minCol:maxCol,minRow:maxRow]

                unlabeled = where(submap lt 1, nUnlabeled)

                ;if a background label gets replaced
                ; by an event label we need to substract the values
                ;       from the background
                ; sum for this label

                ;add the number of pixel which are newly labeled as
                ;       event pixel in this
                ; step to the number of pixel for this particular event
                xrays[l - 1, 0] = xrays[l - 1, 0] + nUnlabeled
                ;add signal in target are to overall signal for the
                ;       current label
                if (nUnlabeled gt 0) then begin
                        xrays[l - 1, 1] = xrays[l - 1, 1] + $
                                total(subim[unlabeled])
                endif

                ;substract the number of pixel which get labeled
                ;       from background to
                ; event pixels from the number of pixels for
                ;       background substraction
```

```
                bglabeled = where(submap lt 0, nBglabeled)
                xrays[l – 1, 2] = xrays[l – 1, 2] – nBglabeled
                ;print, "xrays[", l – 1 ,", 2] = ", xrays[l – 1, 2]

                ;substract the signal from the background signal for the pixel
                ; which get relabeled from background to event pixel
                if (nBglabeled gt 0) then begin
                        xrays[l – 1, 3] = xrays[l – 1, 3] – $
                                total(subim[bglabeled])
                endif

                ;label the area
                submap[*,*] = l

                ;replace the submap in the map by the labeled one
                map[minCol:maxCol,minRow:maxRow] = submap
        endif else begin

                submap = map[minCol:maxCol,minRow:maxRow]
                subim = im[minCol:maxCol,minRow:maxRow]

                ; find which pixels are not labeles (<0)
                unlabeled = where(submap eq 0, nUnlabeled)
                xrays[–l – 1, 2] = xrays[–l – 1, 2] + nUnlabeled

                if (nUnlabeled gt 0) then begin
                        ; label them
                        submap[unlabeled] = l

                        xrays[–l – 1, 3] = xrays[–l – 1, 3] + $
                                total( subim[unlabeled] )
                        ;replace the submap in the map by the labeled one
                        map[minCol:maxCol,minRow:maxRow] = submap
                endif
        endelse


end

; marks (boxes) an xray event
pro markEvent, im, eventMap, areaMap, xrays, ecol, erow, d, d_bg, n

;2.0) Check if any pixels are labeled already.
        if (eventMap[ecol, erow] gt 0) then begin

;2.1) Lable all pixel in the target area around the event pixel
```

```
;           whith the current event number
                        label, im, areaMap, xrays, ecol, erow, d, n
;2.2) Lable all pixel around the tart area for background substration
;           with the nagative of the current event number, background
;           substration labelen can not overwrite event summation labeling
                        label, im, areaMap, xrays, ecol, erow, d_bg, - n
;2.4) Eliminate pixel out of the event map (since processed already
                        eventMap[ecol, erow] = -1
;2.3) Check if there are any event pixel in the radius (2*d_bg + 2).
;           If yes go for those pixel to 2.3 and keep current event number
                        r = 2*d_bg
                        ;range checks
                        minCol = ecol - r
                        maxCol = ecol + r
                        minRow = erow - r
                        maxRow = erow + r
                        if (minCol lt 0) then minCol = 0
                        if (minRow lt 0) then minRow = 0
                        s = size(eventMap)
                        if (maxCol gt (s[1] -1) ) then maxCol = s[1] -1
                        if (maxRow gt (s[2] -1) ) then maxRow = s[2] -1

                        otherEventPos = where( $
                                    eventMap[minCol: maxCol, minRow : maxRow] gt 0,$
                                    nOtherEvents   )

                        for oe = 0,nOtherEvents - 1 do begin
                                    oecol = get_col($
                                                eventMap[minCol: maxCol, minRow : maxRow],$
                                                otherEventPos[oe]) + minCol;
                                    oerow = get_row($
                                                eventMap[minCol: maxCol, minRow : maxRow],$
                                                otherEventPos[oe]) + minRow;

                                    markEvent, im, eventMap, areaMap, xrays, oecol,$
                                                oerow, d, d_bg, n
                        endfor
            endif
end

;
; INPUT PARAMETERS:
;           im          -           xray image
;           delta       -           threshold, if pixel > delta+mean it is cosidered
;                                               to be a possible xray event
;           d and d_bg are the radiuses for the event integration and the
```

```
;                                       background  substraction
;           d  =  2,  d_bg  =  3  for  5x5  summation  and  6x6  background  summation
;           d  =  1,  d_bg  =  2  for  3x3  summation  and  5x5  background  summation
function  getXrays,  im,  delta,  d,  d_bg  $
            ;output,  optional
            ,  eventMap  $
            ,  areaMap  $
            ,  QUIET  =  quiet

            s  =  size(im)

            ;  create  event  map,  basically  flags  all  possible  event
            eventMap  =  make_array(s[1],  s[2])
            eventMap[*,*]  =  0

            ;  create  area  map,  falgs  for  either  event  signal  integration  or
            ;           background  substraction
            areaMap  =  make_array(s[1],  s[2])
            areaMap[*,*]  =  0
            mn  =  (  moment(im)  )[0]
            ;1)  number  all  pixel  with  possible  x  ray  event   (>  delta+mean)
            ;           in  event  map
            eventPos  =  where(im  gt  (mn  +  delta),  nEventPos  )

            ;create  array  to  store  event  signals
            ;  y  =  0:  number  of  pixel  for  the  particular  event
            ;  y  =  1:  sum  of  the  pixel  values  for  the  event
            ;  y  =  2:  number  of  pixel  for  the  background  substraction
            ;  y  =  3:  sum  of  the  background  pixel
            xrays  =  make_array(nEventPos,4)

            if  (not  keyword_set(QUIET))  then  print,  "Found  ",  nEventPos,$
                         "  possible  event  locations"

            if  (nEventPos  gt  0)  then  eventMap[eventPos]  =  1

            ;2)  For  all  events:  2.1)
            for  e  =  0LL,  nEventPos  -  1  do  begin
                        ecol  =  get_col(im,  eventPos[e]);
                        erow  =  get_row(im,  eventPos[e]);
                        if  (not  keyword_set(QUIET))  then  $
                                    if  ((e  mod  1000)  eq  0)  then  $
                                       print,  "Exploring  event  number  ",  e,   "  of  ",  $
                                               nEventPos,  "  @  (",   ecol,  ",",  erow,  ")"

                        n  =  (e  +  1)
```

```
                markEvent, im, eventMap, areaMap, xrays, ecol, erow, d, d_bg, n
        endfor

        sort_aM = areaMap[sort(areaMap)]
        uniq_aM = sort_aM[ uniq(sort_aM) ]
        s = size(uniq_aM)
        ;s[1] - 1 / 2 because every event area occours twice, onece positive,
        ;       once negativ.
        ;       -1 to substract away the zero
        if (not keyword_set(QUIET)) then print, "Identified ", $
                (s[1] - 1.0) / 2, " unique event areas."
        return, xrays

end

; Generates a xray histogram using the advance xray identification
;
; INPUT PARAMETERS:
;       im      -       xray image
;       delta   -       threshold, if pixel > delta+mean it is
;                       cosidered to be a possible xray event
;       d and d_bg are the radiuses for the event integration
;                       and the background substraction
;       d = 2, d_bg = 3 for 5x5 summation and 6x6 background summation
;       d = 1, d_bg = 2 for 3x3 summation and 5x5 background summation
; OPTIONAL INPUT PARAMETERS:
;       QUIET   -       disables output
function xrayHist, im, delta, d, d_bg, QUIET = quiet

        xrays = getXrays(im, delta, d, d_bg, QUIET = quiet)

        ; to protect against zero devision
        for i=0LL,( size(xrays) )[1]-1 do  xrays[i,2] = max([1, xrays[i,2]])
        ; now for each event: signal = sum(eventPixel) -
        ;       sum(backgroundPixel)/number(backgroudPixel) * number(eventPixel)
        x = xrays[*,1] - xrays[*,3]/( xrays[*,2] ) * xrays[*,0]


        if (not keyword_set(QUIET)) then print, $
                "Mean of background pixel value:", $
                mean(xrays[*,3]/( xrays[*,2] ))
        ;make a histogram
        if (not keyword_set(QUIET)) then print, $
                "Starting histogram calculation..."
        return, histogram(x, binsize=1, min=1, max=64000)
```

```
end

; MAIN ROUTINE
;          ; Generates a xray histogram using the advance xray identification
;
; INPUT PARAMETERS:
;          im        -         xray image
;          delta     -         threshold, if pixel > delta+mean it is cosidered to
;                              be a possible xray event
;          d and d_bg are the radiuses for the event integration and the
;                              background substraction
;          d = 2, d_bg = 3 for 5x5 summation and 6x6 background summation
;          d = 1, d_bg = 2 for 3x3 summation and 5x5 background summation
; OPTIONAL INPUT PARAMETERS:
;          QUIET   -           disables output
;          NO_PLOT -           disables plotting
;          PLOTW = set width fot the plot, the range P +/-(P*plotw) will be
;                    plotted, where P is the peak location
;          FITW = set width fot the fit, the range P +/-(P*plotw) will be
;                    fitted, where P is the peak location
pro xrayFit, im, delta, d, d_bg, $
          ; optional ouput parameters for the gauss fit
          ucoef2, uscoef2, xhx, xhy, xhg, aloc, NO_PLOT = no_plot, 4
          QUIET = quiet, PLOTW = plotw, FITW = fitw,$
          DATAFILE=datafile, FITDATAFILE=fitdatafile



          gterms=3
          xhy = xrayHist( im, delta, d, d_bg, QUIET = quiet )

          xp = where(xhy eq max(xhy))
          xp = xp(0)
          xhx = findgen( (size(xhy))[1] )

          ;inlcude a values in the fit which are greater than peak
          ;                    location divided by 4.5
          ;                    and less than peak location times 1.5
          ;aloc=where((xhx gt xp/4.5) and (xhx lt xp*1.5))
          if (not keyword_set(FITW)) then fitw = 0.05
          q_g = fitw
          if (not keyword_set(QUIET)) then print, "fit width: ", fitw
          upperFitLimit = xp + (xp * q_g)
          lowerFitLimit = xp - (xp * q_g)

          if (not keyword_set(QUIET)) then print, "xp: ", xp
```

```
        if (not keyword_set(QUIET)) then print, "Fitting from ",
                $ upperFitLimit, " to ", lowerFitLimit
        aloc=where((xhx gt lowerFitLimit) and (xhx lt upperFitLimit))
        ; do the fit uconf will hold the parameters,
        ;       uscoef will hold the errors
        xhg = mgaussfit(xhx(aloc),xhy(aloc),ucoef,uscoef,nterms=gterms,
                $ ESTIMATES=[xhy[xp],xp,xp*0.02])

        ;Refit
        upperFitLimit = ucoef(1) + (ucoef(1) * q_g)
        lowerFitLimit = ucoef(1) - (ucoef(1) * q_g)
        if (not keyword_set(QUIET)) then print, "mean: ", ucoef(1)
        if (not keyword_set(QUIET)) then print, "Refitting from ", $
                lowerFitLimit, " to ", upperFitLimit
        aloc=where((xhx gt lowerFitLimit) and (xhx lt upperFitLimit))
        ;mF added comment: do the fit uconf will hold the parameters,
        ;        uscoef will hold the errors
        xhg2 = mgaussfit(xhx(aloc),xhy(aloc),ucoef2,uscoef2,$
                nterms=gterms, ESTIMATES=ucoef)

        ;plot data, wire data to files etc...
end
```

APPENDIX D
GLOSSARY

CCD	Charge-Coupled Device
CTE	Charge Transfer Efficiency. Denotes the quality of the charge transfer from one to the next pixel in the CCD. Typically better than 0.99999% i.e. more than 0.99999% of the electrons are transferred.
CTI	Charge Transfer Inefficiency. CTI= 1−CTE
clear	Procedure to clear the CCD, i.e. to clock all the charge out of the active area. The parallel clocks are used to clock out the charge just as it would be done during normal readout. But the serial register it not clocked. Since the readout of the serial register is the major time consuming element during the readout this is a very fast way of eliminating charge in the active area. Based on a 100kHz readout frequency the clear for a 1000 pixel wide CCD can be performed in 10ms. Of course, even though the serial register is much wider than the pixels, the amount of charge it can collect is limited. So if the CCD was saturated several clear cycles with intermediate clocking of the serial register might be necessary.
erase	Procedure to eliminate surface dark current. For LBNL p-channel CCDs the substrate voltage is set to zero volts and the parallel clocks are set to some positive voltage (usually eight to nine volts). This will *flood* the frontsind with electrons. Holes trapped in surface states are eliminated through recombination.
epurge	Method to eliminate baseline drift found in some of the high voltage devices. The parallel clocking voltages are temporarely set to some negative value ($\sim$ -10 V) while all other voltages are kept constant.
ITO	Indium Tin Oxide.
LBNL	Lawrence Berkeley National Laboratory
MC	Monochromator
NIR	Near Infra Red
PSF	Point Spread Function.
RGA	Residual Gas Analyzer. A mass spectrograph used to analyze a vacuum for residual gases. Usually provides a plot of partial pressure as function of mass number.

ROI	Region Of Interest. User defined area of interest. For example a area in the CCD image.
SCP	Super Nova Cosmology Project
SNAP	Super Nova Cosmology Probe
QE	Quantum Efficiency, denotes how many incident photons a detector will actually detect. The external QE is defines a incident photons over signal electrons or holes.

BIBLIOGRAPHY

[1] NIST Atomic Spectra Database Lines Data. `http://physics.nist.gov/cgi-bin/ASD/lines1.pl`.

[2] Overview of the hubble space telescope. `http://www.stsci.edu/hst/HST_overview/`.

[3] SNAP. `http://snap.lbl.gov/`.

[4] Supernova Cosmology Project. `http://supernova.lbl.gov/`.

[5] P. Amico and T. Bohm. The ESO CCD testbench. `http://www.eso.org/projects/odt/CCDtestbench/Testbench.html`.

[6] Neta A. Bahcall and Xiaohui Fan. The most massive distant clusters: Determining Ω and σ_8. *The Astrophysical Journal*, 504:1, 1998.

[7] C. J. Bebek, D. E. Groom, S. E. Holland, A. Karchar, W. F. Kolbe, M. E. Levi, N. P. Palaio, B. T. Turko, M. C. Uslenghi, M. T. Wagner, and G. Wang. Proton radiation damage in high-resistivity n-type silicon ccds. 2002.

[8] Fabrice Christen, Konrad Kuijken, Dietrich Baade, Cyril Cavadore, Sebastian Deiries, and Olaf Iwert. Fast conversion factor (gain) measurement of a CCD using images with vertical gradient. volume Scientific Detectors for Astronomy 2005. SDW, 2005.

[9] Sebastian Deiries, Armin Silber, Olaf Iwert, Evi Hummel, and Jean Louis Lizon. Plasma cleaning - a new method of ultra-cleaning detector cryostats. Astrophysics and Space Since Library, Springer, 2005.

[10] D. F. Edwards. *Handbook of Optical Constants of Solids*. Academic Press, 1985.

[11] Douglas A. Simons et al. Instruments, detectors and the future of astronomy with large ground based telescopes. Astrophysics and Space Since Library, Springer, 2005.

[12] Maximilian H. Fabricius, Chris J. Bebek, Donald E. Groom, Armin Karcher, and Natalie A. Roe. Quantum efficiency characterization of back-illuminated ccds: Part ii. reflectivity measurements. volume 6068, page 60680G. SPIE, 2006.

[13] Jessamyn A. Fairfield, D. E. Groom, S. J. Bailey, C. J. Bebek, S. E. Holland, A. Karcher, W. F. Kolbe, W. Lorenzon, and N. A. Roe. Improved spatial resolution in thick, fully depleted ccds with enhanced red sensitivity. *submitted to IEEE Trans. Nucl. Sci.*, April 2006.

[14] Torsten Fliessbach. *Allgemeine Relativitätstheorie*. Spektrum Akademischer Verlag, 3 edition, 1998.

[15] W. L. Freedman, B. F. Madore, B. K. Gibson, L. Ferrarese, D. D. Kelson, S. Sakai, J. R. Mould, R. C. Kennicutt, H. C. Ford, J. A. Graham, J. P. Huchra, S. M. G. Hughes, G. D. Illingworth, L. M. Macri, and P. B. Stetson. Final results from the hubble space telescope key project to measure the hubble constant. *The Astrophysical Journal*, 553:47, 2001.

[16] D. E. Groom, P. H. Eberhard, S. E. Holland, M. E. Levi, N. P. Palaio, S. Perlmutter, R. J. Stover, and M. Wei. Point-spread function in depleted and partially depleted ccds. ESO, Garching, Germany, 13-16 September 1999 (Kluwer, 2000).

[17] Donald E. Groom, Christopher J. Bebek, Maximilian Fabricius, Armin Karcher, William F. Kolbe, Natalie A. Roe, and Jens Steckert. Quantum efficiency characterization of lbnl ccd's: Part i. the quantum efficiency machine. volume 6068, page 60680F. SPIE, 2006.

[18] Donald E. Groom, Steven E. Holland, Michael E. Levi, Nicholas P. Palaio, Saul Perlmutter, Richard J. Stover, and Mingzhi Wei. Quantum efficiency of a back-illuminated ccd imager: an optical approach. volume 3649, pages 80–90. SPIE, 1999.

[19] Dani Guzman, Sebastien Blais-Ouellette, Marco Bonati, and Amal Elgamil. A versatile wavelength-dependent spectrophotometer for efficiency measurements of ccd and cryogenic gratings. volume 5499, pages 371–378. SPIE, 2004.

[20] E. Holland, G. Goldhaber, D. E. Groom, W. W. Moses, C. R. Pennypacker, S. Perlmutter, N. W. Wang, R. J. Stover, and M. Wei. A 200 x 200 ccd image sensor fabricated on high-resistivity silicon. *IEDM Tech. Digest*, 911, 1996.

[21] S. E. Holland, C. J. Bebek K. S. Dawson, J. H. Emes, M. H. Fabricius, J. A. Fairfield, D. E. Groom, A. Karcher, W. F. Kolbe, N. P. Palaio, N. A. Roe, and G. Wang. High-voltage compatible, fully depleted CCD Development. Orlando, 2006. IEEE.

[22] S.E. Holland, D.E. Groom, N.P. Palaio, R. J. Stover, and M. Wei. Fully depleted, back-illuminated charge-coupled devices fabricated on high-resisitivity silicon. *IEEE Trans. Electron Dev*, 50 (3).

[23] Stephen E. Holland. Fully depleted thick ccds. 2006.

[24] E. Hubble. *Proc. Nat. Acad. Sci.*, 15, 1929.

[25] James R. Janesick. *Scientific Charge-Coupled Devices*. SPIE Press, Bellingham, Washington, USA, 2001.

[26] Gordon Johnston. Charge-Coupled Device (CCD) Imaging Arrays. `http://ranier.hq.nasa.gov/Sensors_page/DD/HST&GLL_CCD.html`.

[27] Yukiko Kamata, Satoshi Miyazaki, Masaharu Muramatsu, Hisanori Suzuki, Kazuhisa Miyaguchi, Takeshi G. Tsuru, Shin ichiro Takagi, and Emi Miyata. Development of thick back-illuminated ccd to improve quantum efficiency in optical longer wavelength using high-resistivity n-type silicon. volume 5499, pages 210–218. SPIE, 2004.

[28] Keithley. *Keithley Model 6485 Picoammeter Instruction manual.* Cleveland, Ohio, USA, 2001.

[29] W. F. Kolbe, S. E. Holland, and C. J. Bebek. Ccd development progress at lawrence berkeley national laboratory. volume Scientific Detectors for Astronomy 2005. SDW2005, 2005.

[30] Michael L. Lampton, Christopher Bebek, Carl W. Akerlof, Greg Aldering, R. Amanullah, Pierre Astier, E. Barrelet, Lars Bergstrom, John Bercovitz, Gary M. Bernstein, Manfred Bester, Alain Bonissent, C. R. Bower, Jr. William C. Carithers, Eugene D. Commins, C. Day, Susana E. Deustua, Richard S. DiGennaro, Anne Ealet, Richard S. Ellis, Mikael Eriksson, Andrew Fruchter, Jean-Francois Genat, Gerson Goldhaber, Ariel Goobar, Donald E. Groom, Stewart E. Harris, Peter R. Harvey, Henry D. Heetderks, Steven E. Holland, Dragan Huterer, Armin Karcher, Alex G. Kim, William F. Kolbe, B. Krieger, R. Lafever, J. Lamoureux, Michael E. Levi, Daniel S. Levin, Eric V. Linder, Stewart C. Loken, Roger Malina, R. Massey, Timothy McKay, Steven M. McKee, Ramon Miquel, E. Moertsell, N. Mostek, Stuart Mufson, J. A. Musser, Peter E. Nugent, Hakeem M. Oluseyi, Reynald Pain, Nicholas P. Palaio, David H. Pankow, Saul Perlmutter, R. Pratt, Eric Prieto, Alexandre Refregier, J. Rhodes, Kem E. Robinson, N. Roe, Michael Sholl, Michael S. Schubnell, G. Smadja, George F. Smoot, Anthony Spadafora, Gregory Tarle, Andrew D. Tomasch, H. von der Lippe, D. Vincent, J.-P. Walder, and Guobin Wang. Snap focal plane. volume 4854, pages 632–639. SPIE, 2003.

[31] Robert W. Leach and Frank J. Low. Ccd and ir array controllers. volume 4008, pages 337–343. SPIE, 2000.

[32] Michael P. Lesser and Bradley McCarthy. Quantum efficiency characterization of scientific ccds. volume 2654, pages 278–286. SPIE, 1996.

[33] Eric V. Linder. Probing dark energy with snap, 2002.

[34] Charles W. Misner, Kip S. Thorne, and John Archibald Wheeler. *Gravitation.* W. H. Freeman and Company, Ney York, 24 edition, 1932.

[35] S. Miyazaki, M. Sekiguchi, K. Imi, N. Okada, F. Nakata, and Y. Komiyama. Characterization and mosaicing of CCDs and the applications to the subaru wide field camera (suprime-cam).

[36] G. Aldering (on behalf of the) SNAP collaboration. Overview of the supernova/acceleration probe (snap), 2002. astro-ph/0209550.

[37] Frank L. Pedrotti and Leno S. Pedrotti. *Introduction to Optics.* Prentice Hall, New Jersey, 1993.

[38] S. Perlmutter, G. Aldering, G. Goldhaber, R. A. Knop, P. Nugent, P. G. Castro, S. Deustua, S. Fabbro, A. Goobar, D. E. Groom, I. M. Hook, A. G. Kim, M. Y. Kim, J. C. Lee, N. J. Nunes, R. Pain, C. R. Pennypacker, R. Quimby, C. Lidman, R. S. Ellis, M. Irwin, R. G. McMahon, P. Ruiz-Lapuente, N. Walton, B. Schaefer, B. J. Boyle, A. V. Filippenko, T. Matheson, A. S. Fruchter, N. Panagia, H. J. M. Newberg, and W. J. Couch. Measurements of omega and lambda from 42 high-redshift supernovae. *The Astrophysical Journal*, 517:565, 1999.

[39] K. Rajkanan, R. Singh, and J. Shewchun. Absorption coefficient of silicon for solar call calculations. *Solid-State Electronics*, 22, 1979.

[40] Adam G. Riess, Alexei V. Filippenko, Peter Challis, Alejandro Clocchiattia, Alan Diercks, Peter M. Garnavich, Ron L. Gilliland, Craig J. Hogan, Saurabh Jha, Robert P. Kirshner, B. Leibundgut, M. M. Phillips, David Reiss, Brian P. Schmidt, Robert A. Schommer, R. Chris Smith, J. Spyromilio, Christopher Stubbs, Nicholas B. Suntzeff, and John Tonry. Observational evidence from supernovae for an accelerating universe and a cosmological constant. *Astronomical Journal*, 116:1009, 1998.

[41] Rajkanan Singh and Shewchun. *Solid-State Electronics 22.* Astrophysics and Space Since Library, Springer, 1979.

[42] Spectra-Physics. *MS257 Programming Manual Model 77700B.* 150 Long Beach Boulevard, Stratfor, CT 06615-0872, 1994.

[43] Spectra-Physics. *Arc Lemp Power Supply Model 69907.* 150 Long Beach Boulevard, Stratfor, CT 06615-0872, 2004.

[44] Spectra-Physics. *Digital Exposure Controller Model 68945.* 150 Long Beach Boulevard, Stratfor, CT 06615-0872, 2004.

[45] D. N. Spergel, L. Verde, H. V. Peiris, E. Komatsu, M. R. Nolta, C. L. Bennett, M. Halpern, G. Hinshaw, N. Jarosik, A. Kogut, M. Limon, S. S. Meyer, L. Page, G. S. Tucker, J. L. Weiland, E. Wollack, and E. L. Wright. First year wilkinson microwave anisotropy probe (wmap) observations: Determination of cosmological parameters. *The Astrophysical Journal*, 148:175, 2003.

[46] Jens Steckert. Design, implementation and setup of an automated quantum efficiency measurement system for charge-coupled devices, 2005. Unpublished diploma thesis.

[47] John Strong. *Procedures in Experimental Physics.* SPIE Press, 1938.

[48] John L. Tonry, Barry Burke, Peter M. Onaka, Gerard A. Luppino, and Michal J. Cooper. Orthogonal Tranfer Array. Astrophysics and Space Since Library, Springer, 2005.

[49] W.-M. Yao, C. Amsler, D. Asner, R.M. Barnett, J. Beringer, P.R. Burchat, C.D. Carone, C. Caso, O. Dahl, G. D'Ambrosio, A. DeGouvea, M. Doser, S. Eidelman, J.L. Feng, T. Gherghetta, M. Goodman, C. Grab, D.E. Groom, A. Gurtu, K. Hagiwara, K.G. Hayes, J.J. Hernández-Rey, K. Hikasa, H. Jawahery, C. Kolda, Kwon Y., M.L. Mangano, A.V. Manohar, A. Masoni, R. Miquel, K. Mönig, H. Murayama, K. Nakamura, S. Navas, K.A. Olive, L. Pape, C. Patrignani, A. Piepke, G. Punzi, G. Raffelt, J.G. Smith, M. Tanabashi, J. Terning, N.A. Törnqvist, T.G. Trippe, P. Vogel, T. Watari, C.G. Wohl, R.L. Workman, P.A. Zyla, B. Armstrong, G. Harper, V.S. Lugovsky, P. Schaffner, M. Artuso, K.S. Babu, H.R. Band, E. Barberio, M. Battaglia, H. Bichsel, O. Biebel, P. Bloch, E. Blucher, R.N. Cahn, D. Casper, A. Cattai, A. Ceccucci, D. Chakraborty, R.S. Chivukula, G. Cowan, T. Damour, T. DeGrand, K. Desler, M.A. Dobbs, M. Drees, A. Edwards, D.A. Edwards, V.D. Elvira, J. Erler, V.V. Ezhela, W. Fetscher, B.D. Fields, B. Foster, D. Froidevaux, T.K. Gaisser, L. Garren, H.-J. Gerber, G. Gerbier, L. Gibbons, F.J. Gilman, G.F. Giudice, A.V. Gritsan, M. Grünewald, H.E. Haber, C. Hagmann, I. Hinchliffe, A. Höcker, P. Igo-Kemenes, J.D. Jackson, K.F. Johnson, D. Karlen, B. Kayser, D. Kirkby, S.R. Klein, K. Kleinknecht, I.G. Knowles, R.V. Kowalewski, P. Kreitz, B. Krusche, Yu.V. Kuyanov, O. Lahav, P. Langacker, A. Liddle, Z. Ligeti, T.M. Liss, L. Littenberg, L. Liu, K.S. Lugovsky, S.B. Lugovsky, T. Mannel, D.M. Manley, W.J. Marciano, A.D. Martin, D. Milstead, M. Narain, P. Nason, Y. Nir, J.A. Peacock, S.A. Prell, A. Quadt, S. Raby, B.N. Ratcliff, E.A. Razuvaev, B. Renk, P. Richardson, S. Roesler, G. Rolandi, M.T. Ronan, L.J. Rosenberg, C.T. Sachrajda, S. Sarkar, M. Schmitt, O. Schneider, D. Scott, T. Sjöstrand, G.F. Smoot, P. Sokolsky, S. Spanier, H. Spieler, A. Stahl, T. Stanev, R.E. Streitmatter, T. Sumiyoshi, N.P. Tkachenko, G.H. Trilling, G. Valencia, K. van Bibber, M.G. Vincter, D.R. Ward, B.R. Webber, J.D. Wells, M. Whalley, L. Wolfenstein, J. Womersley, C.L. Woody, A. Yamamoto, O.V. Zenin, J. Zhang, and R.-Y. Zhu. Review of Particle Physics. *Journal of Physics G*, 33:1+, 2006.

[]